

Role of Loading Direction on Fatigue Behavior of Smooth and Notched ZK60 Extrusion

by

Amirhossein Pahlevanpour

A thesis

presented to the University of Waterloo

in fulfilment of the

thesis requirement for the degree of

Doctor of Philosophy in

Mechanical Engineering

Waterloo, Ontario, Canada, 2018

© Amirhossein Pahlevanpour 2018

EXAMINING COMMITTEE MEMBERSHIP

The following served on the Examining Committee for this thesis. The decision of the Examining Committee is by majority vote.

Supervisor	Hamid Jahed, Ph.D. Professor, University of Waterloo
External Examiner	HongTae Kang, Ph.D. Professor, University of Michigan-Dearborn
Internal Member	Grzegorz Glinka, Ph.D. Professor, University of Waterloo
Internal Member	Mustafa Yavuz, Ph.D. Professor, University of Waterloo
Internal-external Member	Adil Al-Mayah, Ph.D. Assistant Professor, University of Waterloo

AUTHOR'S DECLARATION

This thesis consists of material all of which I authored or co-authored: see statement of contributions included in the thesis. This is a true copy of the thesis, including any required final revisions, as accepted by my examiners.

I understand that my thesis may be made electronically available to the public.

Amirhossein Pahlevanpour

STATEMENT OF CONTRIBUTIONS

Chapter 3 of this thesis consists of a paper that was co-authored by myself, my supervisor (Dr. Jahed), Dr. Behraves, and SMH. Karparvarfard. The fatigue experimental work has been conducted by myself and SMH. Karparvarfard. Dr. Shaha performed microstructural imaging.

Chapter 4 has been incorporated within a paper to be submitted for publication. The paper is co-authored by myself, Dr. Behraves, and my supervisor. All experimental, analytical and numerical works have been performed by me.

Section 4.5.2 of Chapter 4 has been embedded within a paper to be submitted for publication. The paper is co-authored by Dr. Roostaei, myself, Dr. Behraves, and my supervisor. I carried out the lab experiments on ZK60 extrusion, collected and analyzed the data, and assisted with the writing of the paper. The model was developed in association with Dr. Roostaei, and Dr. Behraves.

The balance of the research is my own work.

ABSTRACT

In spite of the increasing trend of magnesium (Mg) application over the last decade, numerous technical restrictions still limit Mg alloy's extensive implementation in industry. For instance, many mechanical behaviors of Mg alloys are still unknown, which make them risky options for manufacturers who prefer to be well-informed about raw materials' characteristics so as to maximize their product reliability. Therefore, a comprehensive characterization in conjunction with life assessment via empirical models is needed to expand these alloys' application. A literature review has revealed the potential of energy-based models to be employed in strain- and stress-controlled modeling of wrought alloys. However, to the best of the author's knowledge, no study is available yet on the anisotropic fatigue behavior and modeling of smooth and notched ZK60 extrusion, which is the focal point of this research.

The quasi-static and strain-controlled fatigue characteristics of ZK60 extrusion have been investigated along three different directions: the extrusion direction (ED), the radial direction (RD), and 45° to the extrusion direction (45°). The quasi-static response showed symmetric behavior for the samples tested along RD and 45° , whereas ED samples manifested completely asymmetric behavior. Although the ED samples exhibited longer fatigue lives than the RD and 45° in the high cycle fatigue, the fatigue lives in the low cycle fatigue regime were similar. Microstructural analysis revealed finer grains for ED, thereby higher strength for this direction. Moreover, the texture measurement indicated a sharp basal texture justifying asymmetric behavior solely along the ED direction. Higher tensile mean stress and less dissipated plastic energy per cycle for the ED samples, acting as two competing factors, were the principal reasons for showing identical fatigue responses to those of RD and 45° in the low cycle fatigue regime. The fracture surface in the ED direction was dominated by twin lamellae and profuse twinned grains, whereas slip bands were dominant on the fracture surface in RD direction. Smith-Watson-Topper, as a critical-plane strain-based criterion, and Jahed-Varvani (JV), as an energy-based damage criterion, were employed to predict the strain-controlled fatigue lives along all directions using a single set of material parameters.

Fully reversed stress-control condition was also investigated over a wide range of stress amplitudes along two different material directions: ED and RD. The in-plane random texture along RD promotes activation of twinning/detwinning deformations in both tension and compression

reversals, which brings about a sigmoidal but near-symmetric shape for hysteresis loops along this direction. The stress-strain response along ED is asymmetric in tension and compression reversals if subjected to high-stress amplitudes. The asymmetry is attributed to different deformation mechanisms being active in the tension and compression reversals. Overall, loading along ED yields superior fatigue performance compared to RD. One set of JV coefficients extracted from the strain-controlled tests was employed and successfully modeled the anisotropic stress-control fatigue response of the material.

The effect of a material's orientation on the fatigue response of notched ZK60 extrusion was investigated via fully reversed stress-controlled experiments in ED and RD. The anisotropy observed in the stress-life curves of the notched ED and RD samples resembles the stress-controlled fatigue performance of the smooth samples. This observation is attributed to the higher strength of ED specimens, which imposes less plastic-induced-damage in the stress-controlled fatigue experiments. The ED specimens exhibit not only superior fatigue performance but also higher notch sensitivity while loading along RD significantly reduces the notch sensitivity.

ACKNOWLEDGEMENTS

First of all, I would like to express my sincere gratitude to my supervisor, Professor Hamid Jahed, for his valuable support, guidance, and encouragement.

I greatly appreciate my colleagues, Dr. Behraves, Dr. Roostaei, Dr. Shaha, and SMH. Karparvarfard for their precious thoughts and suggestions.

Last but not the least, I owe my deepest gratitude to my beloved parents and brother for their unconditional love and inspiration in every single moment of my life.

Table of Contents

EXAMINING COMMITTEE MEMBERSHIP	ii
AUTHOR'S DECLARATION	iii
STATEMENT OF CONTRIBUTIONS	iv
ABSTRACT	v
ACKNOWLEDGEMENTS	vii
Table of Contents	viii
List of Figures	xii
List of Tables	xvi
Chapter 1 : Introduction	1
1.1 Motivation	2
1.2 Objectives	2
1.2.1 To Characterize the Effects of Loading Direction (Anisotropy) on Fatigue Behavior of Smooth and Notched Members.....	2
1.2.2 To Propose an Anisotropic Fatigue Life Criterion for ZK60 Extrusion under both Stress- and Strain-controlled Conditions.....	3
1.3 Thesis Layout	3
Chapter 2 : Background and Literature Review	5
2.1 Background.....	6
2.1.1 Magnesium	6
2.1.2 Fatigue Models	7
2.1.2.1 Smith-Watson-Topper.....	7
2.1.2.2 Jahed-Varvani	8
2.1.3 Staircase Method	9
2.1.4 Stress Concentration.....	10

2.1.5 Notch Sensitivity	11
2.2 Literature Review	12
2.2.1 Fatigue Behavior of Mg Alloys.....	12
2.2.2 Fatigue Models of Mg Alloys	15
2.2.3 Notch Effects on the Fatigue of Mg Alloys	17
2.3 Summary.....	22
Chapter 3 : Quasi-static and Cyclic Strain-control Behavior.....	23
3.1 Material and Specimens.....	24
3.2 Experimental Procedures	25
3.3 Results	26
3.3.1 Microstructure Analysis	26
3.3.2 Quasi-static Tension and Compression Behavior	27
3.3.3 Cyclic Behavior.....	28
3.3.3.1 Extrusion Direction.....	28
3.3.3.2 Radial direction.....	31
3.3.3.3 45° direction.....	32
3.3.4 Strain-life Curve	34
3.3.5 Fatigue Fracture Surfaces.....	35
3.4 Discussion.....	37
3.4.1 Deformation Behavior.....	37
3.4.2 Effect of Loading on the Fatigue Performance	40
3.5 Fatigue Modeling.....	42
3.5.1 SWT	42
3.5.2 Jahed-Varvani.....	44
3.6 Further Discussion.....	46

3.7 Summary.....	46
Chapter 4 : Cyclic Stress-control Behavior	48
4.1 Material and Specimens.....	49
4.2 Experimental Procedures	50
4.3 Results and Discussion	50
4.3.1 Fatigue Behavior	50
4.3.1.1 Radial Direction.....	50
4.3.1.2 Extrusion Direction.....	54
4.3.2 Stress-life Curve	57
4.3.3 Ratcheting Strain Effects on Fatigue Life	58
4.4 Fatigue Modeling.....	60
4.4.1 Stress-Based Model (Basquin)	60
4.4.2 Energy-Based Model (JV).....	61
4.5 Further Discussion	64
4.5.1 Reference Cycle in Fatigue Modeling.....	64
4.5.2 ESED Modification Accounting for Mean Stress Effect	66
4.6 Summary.....	69
Chapter 5 : Notch Effects.....	71
5.1 Material and Specimens.....	71
5.2 Experimental Procedures	73
5.3 Results	74
5.3.1 Stress-life Behavior	74
5.3.2 Notch Sensitivity	75
5.4 Discussion.....	76
5.5 Summary.....	80

Chapter 6 : Conclusions and Future Works	81
6.1 Conclusions	81
6.2 Future Works	83
References	84

List of Figures

Figure 2-1. Potential slip and twin systems in Mg alloys [5]	6
Figure 2-2. Illustration of elastic and plastic strain energy densities for JV model.....	9
Figure 2-3. Schematic presentation of the changes in stress and strain concentration by increasing the stress at the notch [30]	11
Figure 2-4. Fatigue behavior of Rolled AZ31 along two directions under controlled stress [16] 12	
Figure 2-5. S–N curves of AZ61 extrusion in three different directions [60]	13
Figure 2-6. Contradictory behavior of ED and TD samples in two different wrought Mg alloys: a) AM30 [12] and b) ZA81M [51].....	13
Figure 2-7. b) Schematic illustration of specimens at different orientations; a) Strain-life curve for AZ80 [48].....	14
Figure 2-8. JV promising capability in the life prediction of multiaxial tests on rolled AZ31 under proportional and non-proportional loadings [42].....	16
Figure 2-9. Life prediction of AM30 extrusion by: a) JV and b) SWT [12,31,80,81]	17
Figure 2-10. K_f correlation with K_t for different Mg, aluminum, and steel alloys [83]	18
Figure 2-11. K_f vs. K_t for AM60 cast and AMX602B Mg alloys and comparison with SUS304 and AISI316 steel alloys [84]	18
Figure 2-12. Stress–life curves of AZ80 for notched and un-notched specimens: a) nominal stress and b) elastic notch root stress [85]	19
Figure 2-13. BTGs formation in the vicinity of the notch root due to high compressive loading: a), b) macroscopic level, and c) microscopic level at the boundary of the BTG [88]	19
Figure 2-14. Strain distribution near the notch showing the localized negative strain in compressive loading and the consequent residual strain in the next tensile loading [88]	20
Figure 2-15. Notch sensitivity evolution as the function of cycles to failure for AM30 [88]	20
Figure 2-16. Stress–Life curves for ZK60 (top) and ZK60-T5 (bottom) for un-notched and notched specimens: a) nominal stress and b) elastic notch root stress [89]	21
Figure 3-1. a) Static tension and fatigue tests specimens’ geometry; b) Static compression tests specimen geometry	24
Figure 3-2. Reference cylindrical coordinate system for sample extraction (Dimensions are in “mm”)	24
Figure 3-3. Typical microstructure of ZK60 extrusion; (a) TD-RD plane and (b) RD-ED plane	26

Figure 3-4. (0002) and (101 $\bar{0}$) pole figures of ZK60 extrusion obtained from; (a) TD-RD plane and (b) ED-RD plane	27
Figure 3-5. Quasi-static behavior under tensile and compressive loading for ED, RD, and 45° .	27
Figure 3-6. Typical engineering stress-strain hysteresis loops of the stabilized cycle for ED ranging from 0.2% to 2% strain amplitudes.....	29
Figure 3-7. Evolution of hysteresis loops for 2 nd and stabilized cycles along ED at different strain amplitudes: (a) 0.3%, (b) 0.5%, (c) 0.8%, and (d) 2%.....	30
Figure 3-8. Typical engineering stress-strain hysteresis loops of the stabilized cycle for RD ranging from 0.2% to 2% strain amplitudes.....	31
Figure 3-9. Evolution of hysteresis loops for 2 nd and stabilized cycles along RD at the strain amplitude of: (a) 1% and (b) 2%.....	32
Figure 3-10. Typical engineering stress-strain hysteresis loops of the stabilized cycle for 45° direction ranging from 0.3% to 2% strain amplitudes	33
Figure 3-11. Evolution of hysteresis loops for 2 nd and stabilized cycles along 45° direction at the strain amplitudes of: (a) 1% and (b) 2%	33
Figure 3-12. A comparison of strain-life (ϵ_a -N) curves obtained from different directions for the ZK60 extrusion	34
Figure 3-13. SEM images of fatigue fracture surfaces of ZK60 extrusion Mg alloy at different strain amplitudes along different directions: (a) ED at $\epsilon_a=0.3\%$, (b) ED at $\epsilon_a=2\%$, (c) RD at $\epsilon_a=0.3\%$, (d) RD at $\epsilon_a=2\%$, (e) 45° at $\epsilon_a=0.3\%$, and (f) 45° at $\epsilon_a=2\%$, (Yellow arrows indicate the position of FCI sites, and the dashed lines represent the boundary between the FCG and the FF areas).....	35
Figure 3-14. SEM images of the fracture surface of ZK60 extrusion at the total strain amplitude of 2% showing twin lamellae and slip bands on the: (a) ED sample and (b) RD sample.....	36
Figure 3-15. Fatigue crack growth at the total strain amplitudes of 0.3% (Top) and 2% (Bottom) for: (a) ED, (b) RD, and (c) 45° samples	36
Figure 3-16. Microstructure illustrating the traces of twin on the polished cross-section of the fatigue-tested samples near the fracture surface, obtained at a strain amplitude of 2% along (a) ED and (b) RD.....	37
Figure 3-17. cyclic tension and compression behavior along ED, RD, 45°	38
Figure 3-18. Ratio of cyclic asymmetry at different strain amplitudes ranging from 0.3 to 2% for	

different sample orientations.....	39
Figure 3-19. Comparison between quasi-static and cyclic curves for ZK60 extrusion along (a) ED, (b) RD, and (c) 45°	40
Figure 3-20. Stabilized hysteresis loops for ED, RD, and 45° at: (a) $\epsilon_a=0.5\%$ and (b) $\epsilon_a=1\%$...	41
Figure 3-21. Nonlinear elastic response of the strain for ED	42
Figure 3-22. Decomposition of strain into elastic and plastic strain in RD.....	43
Figure 3-23. SWT predicted vs. experimental reversals for all directions	44
Figure 3-24. Decomposition of total strain energy into elastic and plastic energies in RD	45
Figure 3-25. Predicted vs. experimental reversals for all directions by JV model	45
Figure 3-26. Total strain energy density as the fatigue damage parameter at different strain amplitudes along different directions for ZK60 extrusion.....	46
Figure 4-1. a) Dog-bone specimens' geometry; b) Specimens' orientations machined from ZK60 extrusion billet	49
Figure 4-2. Strain ratcheting in the first cycle along RD at $\sigma_a = 200$ MPa	51
Figure 4-3. Evolution of stress-strain hysteresis loops along RD at $\sigma_a = 200$ MPa.....	52
Figure 4-4. Strain evolution along RD at $\sigma_a = 200$ MPa.....	52
Figure 4-5. Stress-strain hysteresis loops along RD at different stress amplitudes, ranging from $\sigma_a = 120$ to 200 MPa: (a) for the 1 st cycle, and (b) for the half-life cycle	53
Figure 4-6. Strain ratcheting in the first cycle along ED at $\sigma_a = 200$ MPa	54
Figure 4-7. Evolution of stress-strain hysteresis loops along ED at $\sigma_a = 200$ MPa	55
Figure 4-8. Strain evolution along ED at $\sigma_a = 200$ MPa	55
Figure 4-9. Stress-strain hysteresis loops along ED at different stress amplitudes, ranging from $\sigma_a = 120$ to 200 MPa: (a) for the 1 st cycle, and (b) for the half-life cycle	56
Figure 4-10. Stress-life curves for RD and ED.....	57
Figure 4-11. Smaller hysteresis loops of ED compared to RD at two stress amplitudes	58
Figure 4-12. Initial compressive mean strain for the RD compression first test at $\sigma_a = 200$ MPa	59
Figure 4-13. Effect of loading sequence on half-life hysteresis loops for ZK60 extrusion under $\sigma_a = 200$ MPa.....	59
Figure 4-14. Basquin equation fitted to the stress-life curves of RD and ED	60
Figure 4-15. Predicted vs. experimental life for different directions using Basquin equation	61
Figure 4-16. Comparing TSED as a function of reversals for different loading conditions.....	62

Figure 4-17. Predicted life vs. experimental life for both directions using one set of JV coefficients	63
Figure 4-18. Mean squared error for strain- and stress-controlled tests, representing the prediction accuracy of JV and Basquin models	64
Figure 4-19. Evolution of TSED with respect to normalized life.....	65
Figure 4-20. Experimental life vs. the life predicted by JV, using Ellyin’s definition for ESED	67
Figure 4-21. Schematic illustration of Ellyin’s and proposed definition for positive elastic energy density	68
Figure 4-22. The experimental life vs. the life predicted by JV using the ESED new definition	69
Figure 5-1. Cyclic notched samples (All dimensions are in mm).....	72
Figure 5-2. Schematic illustration of the reference cylindrical coordinate system utilized for the notched-specimen extraction	72
Figure 5-3. Detection of crack initiation and propagation on both sides of a notched sample by using a stereo camera setup: (a) left image, and (b) right image	73
Figure 5-4. S-N curve for notched samples along ED and RD under fully reversed loading condition	74
Figure 5-5. Stress vs. crack initiation life for notched samples along ED and RD	75
Figure 5-6. S-N curves for ED and RD notched and smooth samples with fitted power functions in semi-log scale	77
Figure 5-7. Evolution of fatigue stress concentration (K_f) over number of cycles.....	78
Figure 5-8. Evolution of notch sensitivity (q) over number of cycles	78
Figure 5-9. Crack initiated at a location other than the notch root (ED sample under $\sigma_{root} = 160$ MPa).....	79

List of Tables

Table 2-1. Notch sensitivity of ZK60 and ZK60-T5 [89].....	21
Table 3-1. Quasi-static mechanical properties of ZK60 extrusion along different directions (The numbers in the parentheses are standard deviations).....	28
Table 3-2. Coffin-Manson parameters for SWT model.....	43
Table 3-3. JV model parameters	44
Table 4-1. Strain energy density comparison in different cycles.....	66
Table 5-1. Sequential tests to obtain fatigue strength along ED.....	75
Table 5-2. Sequential tests to obtain fatigue strength along RD.....	76
Table 5-3. Fatigue strength along two directions based on the staircase method.....	76
Table 5-4. Notch parameters for ED and RD	76

Chapter 1

Introduction

Light-weighting is one of the pivotal steps toward fuel consumption reduction in vehicles and consequent environmental preservation. Magnesium (Mg) alloys, as the lightest engineering metal, could contribute to this process. However, they must first be well characterized in order to elucidate their properties for the transportation industry [1]. The present study is concerned with the effect of loading direction on the fatigue behavior of notched ZK60 extrusion as a wrought Mg alloy. This chapter introduces this thesis in three sections: research motivations, objectives, and the thesis outline.

1.1 Motivation

Environmental concerns, as well as economic considerations, have shaped car manufacturers' strategies toward cutting fuel consumption in vehicles. Reducing weight by adopting lightweight materials such as Mg alloys has been a key approach to achieving this goal [1]. In spite of the very low density (1.8 g/cm^3) that makes Mg the lightest structural metal, its applications have been limited. One challenge ahead of applying Mg alloys in load-critical components is their complex mechanical behavior, which arises from their crystallographic structure. This complexity is more pronounced in textured wrought alloys than in cast alloys, and results in intricate fatigue analysis [2].

Mg was first adopted in the automotive industry by Volkswagen in its Beetle model [1]. High interest in light-weighting, owing to governments' environmental aid policies, increased the Mg average usage per car from 3 kg in 2005 to 20 kg in 2010 [3]. However, in spite of the current wide implementation of Mg alloys in many non-structural automotive components such as trim parts and casings, their application in load-bearing sections is still limited [4]. To expand their application to these sections, it is of key importance to investigate Mg alloys' behavior under both static and cyclic loadings. The wrought alloys are better candidates for load-bearing components, having greater strength than cast alloys.

Notches are inevitable in many components and structures due to design limitations. In addition, they are the locations for stress concentration and are susceptible to fatigue failure. As a result, understanding the fatigue behavior at a notch is of key importance. This need justifies the proposed research, aimed to analyze the notch effects on the anisotropic fatigue response of ZK60 extrusion as a high-strength wrought Mg alloy.

1.2 Objectives

This thesis is motivated by two main objectives.

1.2.1 To Characterize the Effects of Loading Direction (Anisotropy) on Fatigue Behavior of Smooth and Notched Members

The induced strong texture in wrought Mg alloys results in anisotropic mechanical properties (dissimilar behavior in different material orientations). In addition to that, notches affect the life

of load bearing members significantly, according to the fact that they locally boost the strain/stress. As a result, anisotropy and notch effect are two crucial factors in the fatigue analysis of Mg notched members.

Despite the importance of life correlation in Mg alloys as a promising candidate for their extensive application in many industries, limited research has been conducted on characterizing their fatigue damage mechanisms. This lack of knowledge is even more pronounced when it comes to loading direction (anisotropy) and notch-effect considerations. A better understanding of active fatigue mechanisms contributes to selecting appropriate damage parameters in the next objective. Designing and performing direction-based experiments on smooth and notched samples are crucial steps in meeting this first objective.

1.2.2 To Propose an Anisotropic Fatigue Life Criterion for ZK60 Extrusion under both Stress- and Strain-controlled Conditions

Numerous fatigue damage criteria have been developed in the past three decades. However, only a limited number of them are capable of taking into account both anisotropy and asymmetry (dissimilar behavior under tension and compression), two main characteristics of wrought Mg alloys that complicate their fatigue analysis. In addition to such intricacies, the load controlling parameters in the cyclic tests, i.e. stress or strain, could crucially alter the material's fatigue response. Controlling strain induces mean stress in the stress-strain hysteresis loops, whereas controlling stress tests may impose ratcheting mean strain.

The final and main objective of this research is to propose an applicable fatigue life criterion for ZK60 extrusion alloy regardless of both the load controlling parameters and the material's direction.

1.3 Thesis Layout

In accordance with the aforementioned research objectives, this thesis incorporates two main investigations on ZK60 extrusion; characterization and fatigue modeling. The organization of the thesis is as follows:

Chapter 2 provides brief background information on Mg, in particular, wrought alloys, their crystallographic structure, and mechanical characteristics. To furnish pertinent modeling in the following chapters, the fatigue models are categorized and the employed ones are meticulously

introduced. Eventually, a review of the available studies on fatigue of smooth and notched wrought Mg alloys, in particular ZK60 extrusion, is followed by divulging the gap in the literature at the end of this chapter.

Chapter 3 begins with the microscopic characterization of ZK60 extrusion. The cyclic behavior of the material, including its strain-life and stabilized strain-stress response together with the fractographic observations, are presented and rigorously discussed along three different material's directions. Finally, the merits of two common fatigue models are assessed based on their capability of mimicking experimental data.

Chapter 4 focuses on the fatigue behavior characterization of the material under stress-controlled condition in two perpendicular directions. Special attention is given to a detailed explanation of the observed anisotropy and asymmetry. Jahed-Varvani, as an energy-based model, will be calibrated first, using strain-controlled experiments. Lastly, the merit of the model is scrutinized by using the same set of the material parameters to predict the fatigue life for stress-controlled tests.

Chapter 5 covers the influence of notch presence on the anisotropic fatigue response of the material. The fatigue stress concentration factor, as well as notch sensitivity, is quantified over lifetime. The probable sources of the observed dissimilarity in the notch sensitivity along two material orientations are discussed.

Ultimately, Chapter 6 outlines the concluding remarks and comments on the prospects for the further works.

Chapter 2

Background and Literature Review

This chapter starts with background information on Mg in terms of its crystallographic structure and unique mechanical characteristics. Then, the two fatigue models employed in this study are explained in detail. In order to statistically quantify fatigue strength, the staircase method is described next. Stress concentration and notch sensitivity, two terms generally used in notch study, are lastly elaborated on in the background section. The chapter concludes with highlights of relevant research and the identification of a gap in the literature.

2.1 Background

2.1.1 Magnesium

The profound impact of the automotive industries on greenhouse gas emission and global warming has led them to the light-weighting of their products [1]. Mg alloys with roughly 35% and 75% less density than aluminum and steel, respectively are the lightest available structural metals. This low density and high specific strength of the Mg alloys have made them highly attractive for the transportation industries. In addition to low density, they offer excellent machinability and very good die-castability [2]. These alloys are classified into wrought and casting types. The former is worked to shape, e.g. through extrusion, rolling, forging processes, and performs better than the latter under monotonic and cyclic loadings. The enhanced behavior in wrought alloys is due to the absence of detrimental defects such as inclusion and porosity that are formed during the cast alloy solidification.

The hexagonal close pack (HCP) lattice structure of Mg makes a noteworthy difference between Mg and other conventional alloys in term of deformation mechanisms. The low availability of deformation systems with HCP structure results in poor formability of Mg alloys at room temperature. Whereas dislocation slip is the only plastic deformation mechanism for many engineering alloys, the limited number of slip systems enforces twinning activation in Mg alloys. Figure 2-1 illustrates the predominant slip and twin planes in Mg alloys.

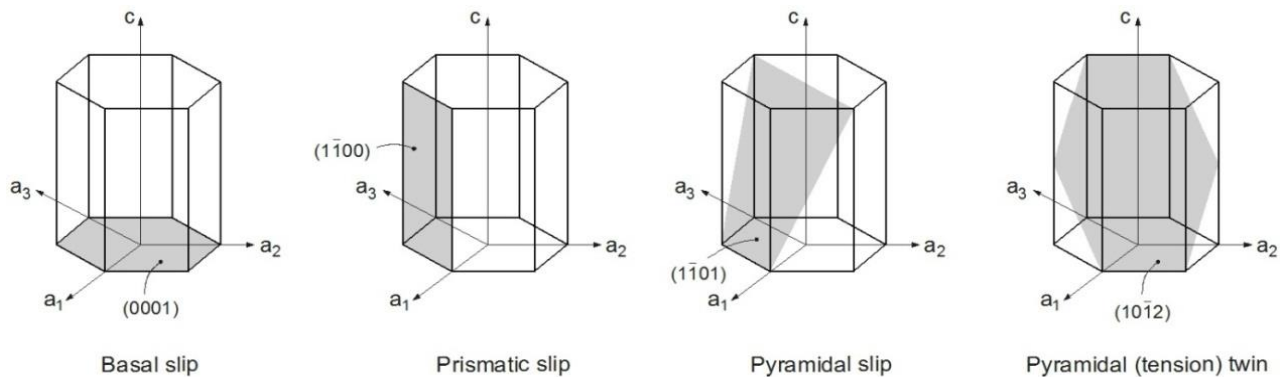


Figure 2-1. Potential slip and twin systems in Mg alloys [5]

Asymmetry (dissimilar behavior under tension and compression) and anisotropy (dissimilar behavior in different material orientations) are the two main mechanical characteristics of wrought

Mg alloys. Activation of $\{10\bar{1}2\}$ extension-twinning deformation mechanism when the external load provokes tension along the c-axis in HCP crystals along one direction and slip-dominant deformation in the reverse direction distorts the loading-unloading curve, a behavior known as asymmetry [6]. The yield asymmetry in Mg alloys is distinct from previously reported hydrostatic pressure dependent strength-differential effect seen in high strength steel [7]. Forming processes such as rolling or extrusion render the c-axis perpendicular to the forming direction, bringing about an intensive basal texture, and eventually causing anisotropy in wrought Mg alloys [8].

Alloying elements can affect the Mg properties proportional to the amount of added constituent. According to ASTM codification, ZK60 is produced by adding Zink and Zirconium, as alloying ingredients to Mg. Zink improves the room-temperature strength, and when combined with Zirconium, the mixture potentially refines the grains and makes the alloy participation-hardenable. Zink also suppresses the corrosive, undesirable effects of nickel and iron impurities.

2.1.2 Fatigue Models

2.1.2.1 Smith-Watson-Topper

Smith–Watson–Topper (SWT) was introduced as a critical plane approach for modeling material in which fatigue cracks are initiated and grew predominantly under tensile loading [9]. The SWT parameter was founded on the principal strain range and maximum stress on the principal strain plane, namely $\Delta\varepsilon_1$ and $\sigma_{n,max}$, respectively, in the following formulation:

$$SWT = \sigma_{n,max} \frac{\Delta\varepsilon_1}{2} \quad \text{Eq. 2-1}$$

This parameter was originally suggested to account for the mean stress effect and has been extensively employed in many efforts to estimate the fatigue life of Mg alloys [10–15]. Although the SWT parameter was defined the same in all those studies, its correlation with fatigue life was made differently. In the present study, the correlation is formulated by integrating SWT with the Coffin-Manson relation as follows:

$$SWT = \frac{\sigma'_f{}^2}{E} (2N_f)^{2b} + \sigma'_f \varepsilon'_f (2N_f)^{b+c} \quad \text{Eq. 2-2}$$

where:

σ'_f : Fatigue strength coefficient

ε'_f : Fatigue toughness coefficient

b : Fatigue strength exponent

c : Fatigue toughness exponent

and E is the modulus of elasticity and $2N_f$ is the number of reversals to failure. Other components on the right side of the equation are based on the Coffin-Manson approximation and will be extracted by employing strain-life and hysteresis curves. In this approach, the strain range is decomposed into elastic and plastic parts ($\Delta\varepsilon_e$ and $\Delta\varepsilon_p$), which are calculated from the stabilized hysteresis loop for each strain amplitude:

$$\frac{\Delta\varepsilon_e}{2} = \frac{\sigma'_f}{E} (2N_f)^b \quad \text{Eq. 2-3}$$

$$\frac{\Delta\varepsilon_p}{2} = \varepsilon'_f (2N_f)^c \quad \text{Eq. 2-4}$$

2.1.2.2 Jahed-Varvani

Energy-based fatigue models, owing to the scalar nature of energy, are promising candidates for describing the fatigue behavior of wrought Mg alloys exhibiting asymmetric and anisotropic characteristics [12,14–16]. By incorporating energy-based fatigue properties, Jahed and Varvani [17] defined a damage parameter similar to that in Ellyin's total strain energy model [18]:

$$\Delta E = \Delta E_e^+ + \Delta E_p \quad \text{Eq. 2-5}$$

Where ΔE_e^+ and ΔE_p are elastic strain energy density (ESED) and plastic strain energy density (PSED), respectively. ΔE is TSED and is considered as the Jahed-Varvani (JV) damage parameter. PSED is essentially the area inside the hysteresis loop, and ESED is calculated from $\sigma_{max}^2/2E$, in which E and σ_{max} are the Young's modulus and maximum stress, respectively. Figure 2-2 schematically illustrates the JV damage parameter's components. The elastic and plastic energy values are extracted from the half-life hysteresis loops. The life correlation of the JV model is defined as follows:

$$\Delta E = E'_e (2N_f)^B + E'_f (2N_f)^C \quad \text{Eq. 2-6}$$

where

E'_e : Fatigue strength coefficient

E'_f : Fatigue toughness coefficient

B : Fatigue strength exponent

C : Fatigue toughness exponent

are the material constants. The coefficients E'_e and B are obtained by fitting a power curve into the experimental ESED, ΔE_e^+ , and the coefficients E'_f and C are found from the experimental PSED, ΔE_p . This model has been extensively in modeling fatigue behavior different alloys including Mg alloys [15,19–27]; however, its capability to capture anisotropy on ZK60 has not been studied.

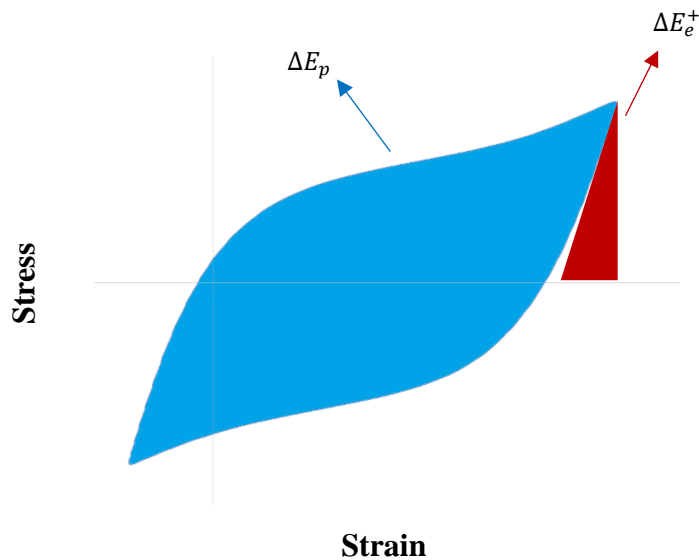


Figure 2-2. Illustration of elastic and plastic strain energy densities for JV model

2.1.3 Staircase Method

The Scattered distribution of fatigue data-points, specifically in the high cycle regime, entails a statistical procedure for fatigue strength calculation at a given life. To that intent, the International Organization for Standardization (ISO) has proposed staircase estimation [28]. A method originally introduced by Dixon and Mode [29] to deal with dosage/mortality sensitivity analysis.

A rough mean and standard deviation (SD) approximation of the fatigue strength is a requisite for the staircase method. The method starts with testing the sample at the first stress level (S_0), preferably close to the estimated fatigue strength of the material at the intended cycle. Based on the survival or failure of the sample, the subsequent stress level will be selected by incrementing

or decrementing the stress by a specified amount, referred to the stress-step (d). The stress-step should be taken as close to the SD as possible. In the case of SD unavailability, 5% of the mean fatigue strength estimation can be employed as the stress-step. The process will be continued sequentially until all the samples are tested in the explained manner. Finally, the mean and SD of the survived population will be calculated and reported as the fatigue strength of the material and its variation, respectively.

2.1.4 Stress Concentration

Notches cause confined stress and strain concentrations. The theoretical stress concentration factor, K_t , is defined as follows to measure the level of this localized concentration within the elastic response regime:

$$K_t = \frac{\sigma_{root}}{\sigma_n} = \frac{\varepsilon_{root}}{\varepsilon_n} \quad \text{Eq. 2-7}$$

Where:

σ_r, ε_r : The notch root stress and strain, respectively

σ_n, ε_n : The nominal stress and strain at the net section, respectively

K_t is a function of both the geometry and mode of loading and plays a key role in the fatigue assessment of notched members, though its applicability is restricted to the linear elastic deformation state. The notched members are usually loaded high enough that the calculated stress from Eq. 2-7 exceeds the yield strength, and plastic deformation occurs consequently. In fact, the local stress may not follow Hooke's law and so becomes disproportionate to the local strain. In the elastoplastic condition, strain and stress concentration factors are defined independently as [30]:

$$K_\sigma = \frac{\sigma_r}{\sigma_n} \quad \text{Eq. 2-8}$$

$$K_\varepsilon = \frac{\varepsilon_r}{\varepsilon_n} \quad \text{Eq. 2-9}$$

where K_σ and K_ε are the stress and strain concentration factors, respectively. The variation in these factors is illustrated schematically versus notch stress in Figure 2-3. The elastoplastic stress and strain of notched members can be assessed by experimental, analytical or numerical approaches [30]. It should be noted that in the present study, the (net) nominal stress, σ_n , (remote load divided by net cross-section) is used as the reference stress for notched specimens.

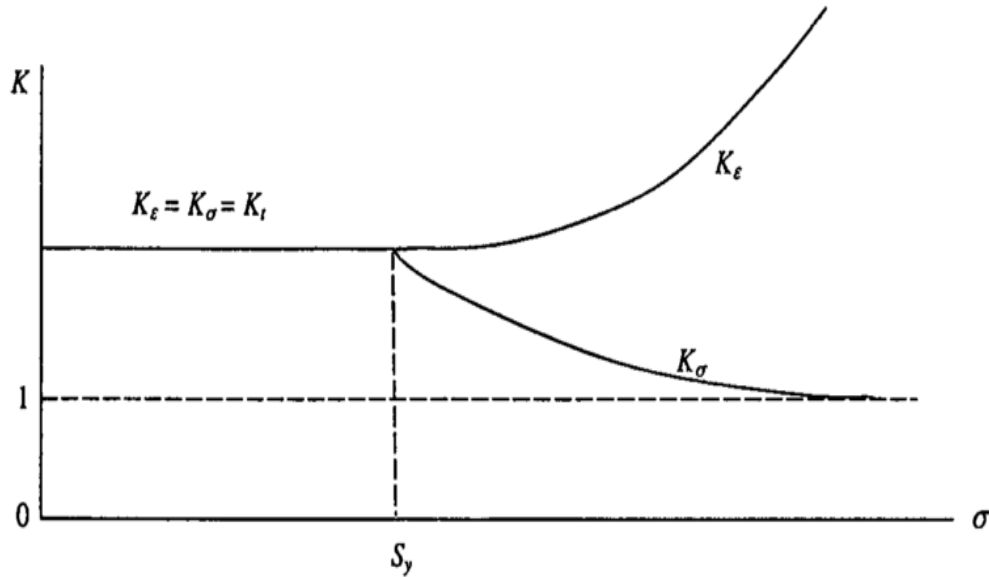


Figure 2-3. Schematic presentation of the changes in stress and strain concentration by increasing the stress at the notch [30]

2.1.5 Notch Sensitivity

According to the above definition for stress concentration factor, it might be expected that the net fatigue strength of a notched component would be predicted by dividing the fatigue strength of smooth specimens by K_t . However, under cyclic loading, many materials are not fully sensitive to stress concentration, and therefore a reduced K_t is warranted for calculating the fatigue life of notched members [30]. The ratio of the smooth specimen's fatigue strength to the notched one is commonly referred to as the fatigue stress concentration factor (K_f):

$$K_f = \frac{\text{Fatigue strength of a smooth specimen}}{\text{Fatigue strength of a notched specimen}} \quad \text{Eq. 2-10}$$

The notch sensitivity of materials, q , is expressed in terms of K_t and K_f :

$$q = \frac{K_f - 1}{K_t - 1} \quad \text{Eq. 2-11}$$

When $q = 0$, the material's fatigue strength is not sensitive to the notch, whereas, for $q = 1$, full sensitivity to the notch is expected.

2.2 Literature Review

2.2.1 Fatigue Behavior of Mg Alloys

Asymmetry and anisotropy have been extensively reported and discussed in the literature on wrought Mg alloys under cyclic loading. Numerous studies have presented such a behavior under strain-control fatigue tests, covering a wide range of wrought Mg alloys, including AM30 [12,31–36], AM50 [37], AZ31 [13,16,45,46,27,38–44], AZ61 [47], AZ80 [22,24,48,49], AZ91 [50], ZA81 [51], and ZK60 [52–55]. However, fewer studies have inquired into the anisotropy and asymmetry in the stress-controlled fatigue behavior of wrought Mg alloys [16,37,39,50,56–59]. Park et al. [16] reported that rotating loading direction from the rolling direction toward the normal to the rolled plane (ND), reduces the fatigue strength of wrought AZ31 significantly (Figure 2-4). This behavior has been attributed to the greater degree plastic-strain induced damage in ND, arising from the reduced twinning stress of ND specimens under tension. Zhang et al. [58] conclusively showed that the cyclic softening-to-hardening transition observed in hot-rolled AZ31B is insensitive to both specimen orientation and rolling percent-reduction. The anisotropic fatigue behavior of ZK60 extrusion under the stress-controlled condition is unprecedented.

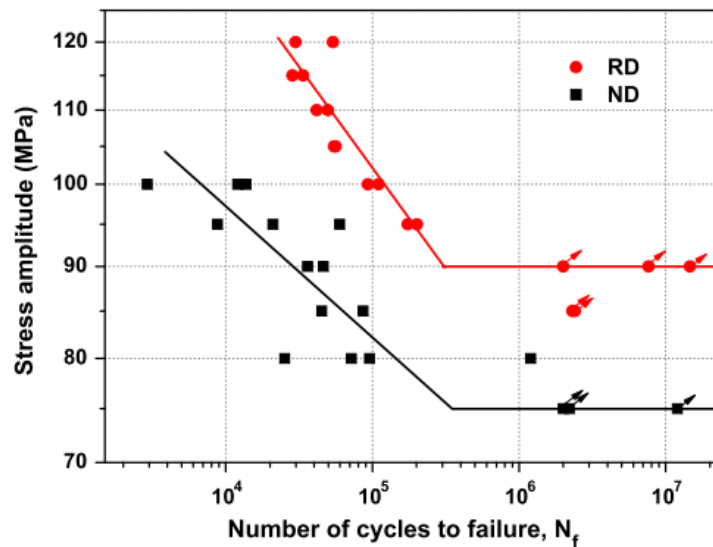


Figure 2-4. Fatigue behavior of Rolled AZ31 along two directions under controlled stress [16]

Anisotropy in Mg alloys can affect the fatigue strength differently in the high-cycle fatigue (HCF) and low-cycle fatigue (LCF) regimes. Sajuri et al. [60] reported that the HCF strength of AZ61 extrusion along the extrusion direction (ED) in stress-controlled experiments is higher than

that in the transverse direction (TD) and 45° to the ED, as depicted in Figure 2-5. The same characteristic was observed under controlled strain by Jordon et al. [31] for AM30 extrusion in the HCF regime, even though for LCF, loading along ED yields lower life to failure than along TD. Roostaei and Jahed [12] investigated the effect of loading direction on the LCF fatigue characteristics of AM30 extrusion. They reported that TD specimens failed in higher lives when identical strain amplitude is applied to both TD and ED specimens. In contrast, Wang et al. [51] found the opposite while testing ED against TD samples under the strain-control state for ZA81M extrusion, a result they attributed to strengthened twinning deformation as well as to the higher detrimental tensile mean stresses in TD (Figure 2-6).

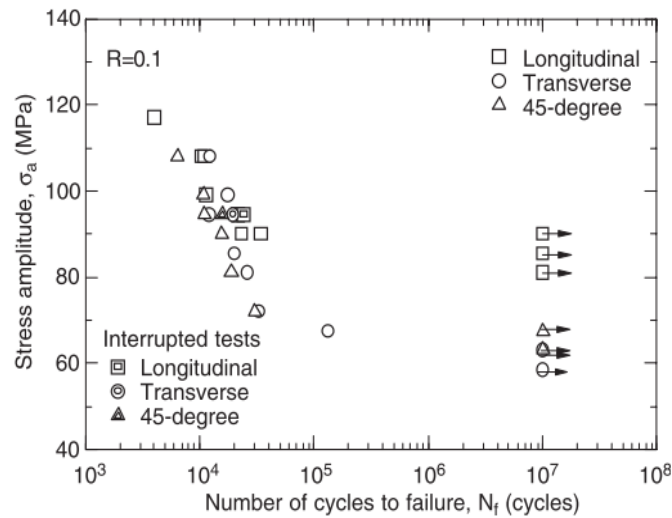


Figure 2-5. S–N curves of AZ61 extrusion in three different directions [60]

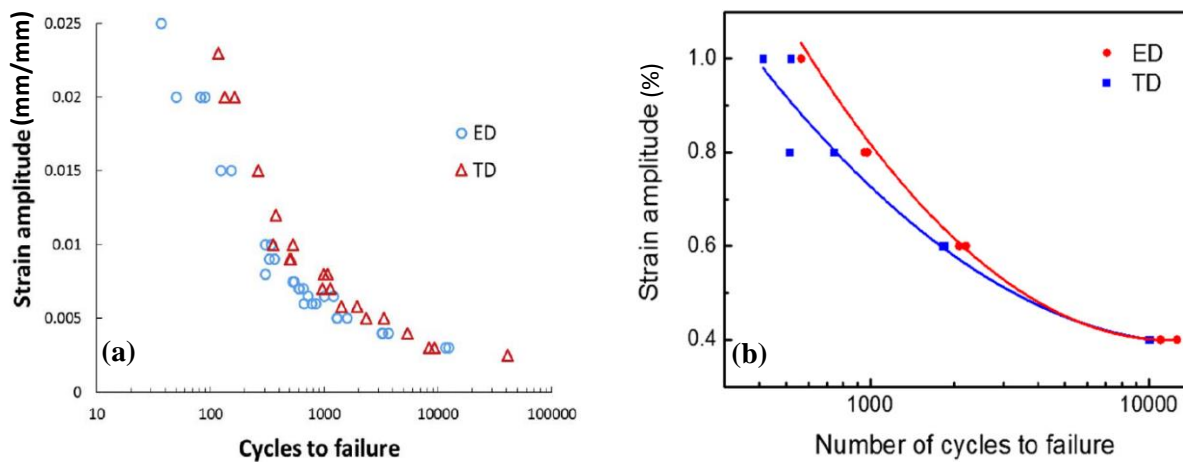


Figure 2-6. Contradictory behavior of ED and TD samples in two different wrought Mg alloys: a) AM30 [12] and b) ZA81M [51]

Xiong and Jiang [48], while experimentally scrutinizing the LCF behavior of AZ80 rolled in four different orientations found that deformation mechanism alteration at a certain strain level affects the material's fatigue resistance with respect to the loading direction. The AZ80 samples in the rolling direction (RD) have the longest life of all other directions for strain amplitudes of less than 0.4%, but increasing the strain to higher values causes the 30° and 60° inclined samples with respect to the rolled plane to exhibit higher fatigue strength. (Figure 2-7).

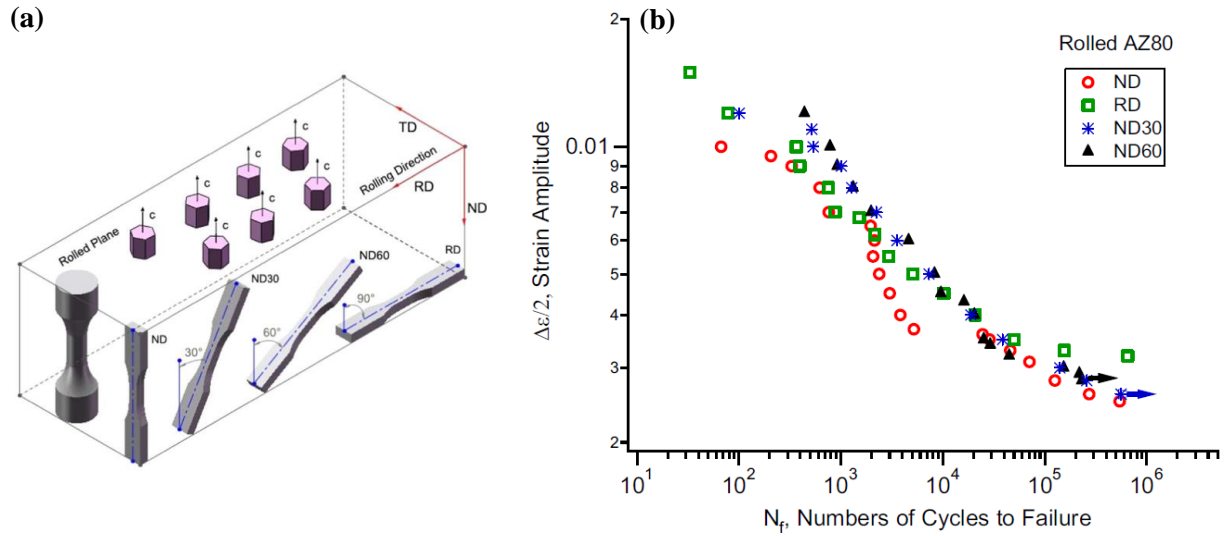


Figure 2-7. b) Schematic illustration of specimens at different orientations; a) Strain-life curve for AZ80 [48]

ZK60, the material which is focused on in this thesis, exhibits exceptional strength and ductility due to its alloying elements [61]. However, despite these characteristics, only limited studies have investigated its fatigue characteristics in extrusion form. Xiong et al. [10,62] and Q. Yu et al. [11] have studied LCF and cyclic plastic deformation, and Wu et al. [6] explored twinning–detwinning behavior of ZK60 extrusion along the ED. These studies reported asymmetry in both the quasi-static behavior and the cyclic hysteresis loops. In another recent study by Xiong et al. [63], characterizing ZK60 under monotonic loading along ED and TD revealed intensive anisotropy in the stress-strain response of the material. The reviewed literature discloses a lack of knowledge on the HCF behavior of ZK60 along directions other than ED.

2.2.2 Fatigue Models of Mg Alloys

Stress, strain, energy, and fracture mechanics are four principal approaches to modeling the fatigue behavior of metals. The fully reversed stress-control behavior has been appropriately expressed using a stress-based fatigue model proposed by Basquin [64]. Later, the Coffin-Manson strain-based relation quantified the strain-life curve in low-cycle (LCF) and high-cycle fatigue (HCF) regimes [65]. Plastic strain energy density (PSED) accumulated in the stabilized stress-strain hysteresis loops was used by Garud [66] and Lefebvre et al. [67] as an energy-based damage criterion. Ellyin [18,68] combined PSED with elastic strain energy density (ESED), suggesting the concept of total strain energy density (TSED) to take into account the mean stress effect. Paris and Erdogan [69] incorporated the concepts of fracture mechanics into Paris' fatigue crack growth law for the subcritical crack propagation region.

The above-mentioned approaches have been adopted to predict the fatigue life of wrought Mg alloys under stress-controlled condition [50,59,70–74]. A study by Ishihara et al. [73] on AZ31 extrusion under different cyclic load ratios demonstrated that the Greber's model performance was superior to that of the modified Goodman model in predicting the fatigue life of stress-controlled experiments. Hasegawa et al. [74] added a correction term to the Coffin-Manson equation in order to improve its accuracy for the life prediction of AZ31 extrusion. The new model provided reliable predictions under the stress-control condition, while the life was over-estimated for the strain-controlled tests, exhibiting retained asymmetry in the stress-strain response of the material. The inability of the Smith [75], Smith–Watson–Topper [9], and Paul–Sivaprasad–Dhar [76] models to predict the fatigue life of rolled AZ91 in rolling and transverse directions led to the proposal of a modification of Basquin's equation [50]. It accounted for the mean stress effect by introducing a new definition for fatigue strength coefficient (σ'_f) and fatigue strength exponent (b). Shiozawa et al. [70] applied different models to predicted the fatigue life of AZ31, AZ61, and AZ80 extruded alloys under both strain- and stress-controlled experiments. They found that TSED, as a fatigue damage parameter, was superior compared to the plastic strain range and PSED. Park et al. [72] showed that Ellyin's criterion provides reliable predictions for different strain and stress ratios. Chen et al. [77] revised the conventional definition of ESED in the Ellyin's model in an attempt to enhance the life prediction accuracy of AZ31B extrusion in a corrosive environment with mean stress. For this purpose, they incorporated both the positive and negative elastic energy densities

into the ESED. Dallmeier et al. [37] weighted the elastic portion of the strain energy to capture the mean stress sensitivity of strain-life and stress-life curves for twin roll cast AM50 in two directions. They identified compressive yield stress (CYS) as a reference limit, beyond which twinning was significantly activated followed by distinct hardening and pronounced increase in the area surrounded by stress-strain hysteresis loops, representing PSED.

Among the different approaches applicable to explaining the fatigue behavior of wrought Mg alloys, the energy approach possesses great potential to describe the damage in different material orientations using a scalar quantity as a damage parameter, i.e., the strain energy density. Energy-based models are commonly differentiated by the definition of ESED and the mathematical expression that correlates the damage parameter to the fatigue life [68].

Jahed and Varvani introduced a fatigue model (JV) based on the governing crack nucleation and propagation mechanisms, along with the plastic energy accumulated by cyclic deformation [17]. In order to extend the original model's applicability to handle non-proportional loading, the incremental cyclic plasticity of Garud was embedded into the strain energy calculation [78]. While examining the role of the load path sensitivity [79], this extended model showed promising life estimation for AZ31B under proportional and non-proportional loading, as shown in Figure 2-8, in a research by Albinmousa and Jahed [42].

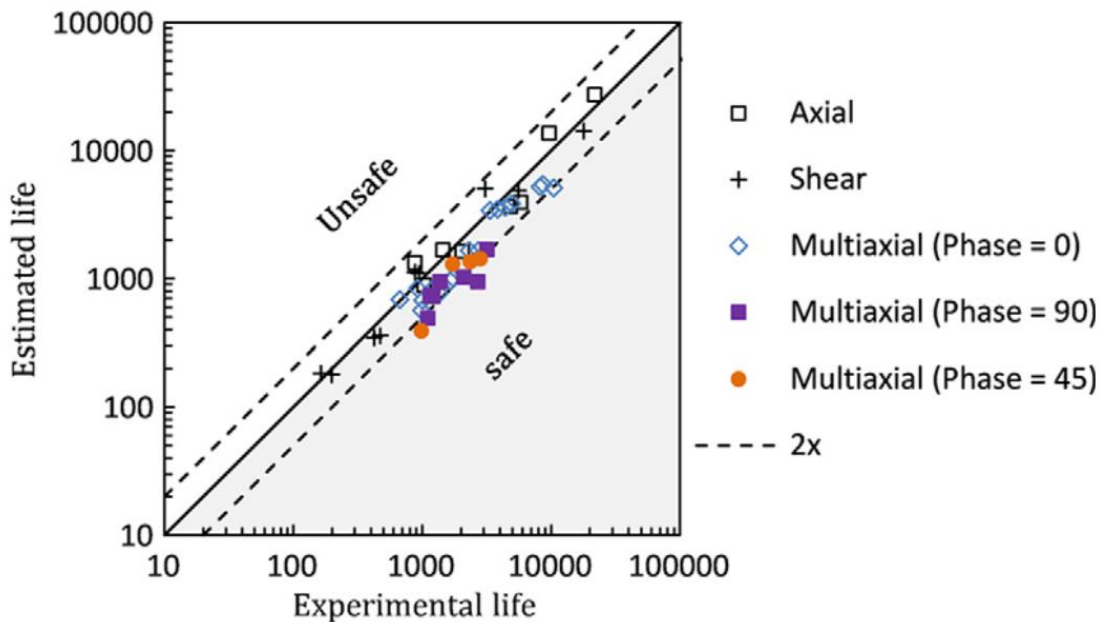


Figure 2-8. JV promising capability in the life prediction of multiaxial tests on rolled AZ31 under proportional and non-proportional loadings [42]

The JV model has been successfully employed for fatigue life correlation of Mg alloys in several studies [15,21,24]. Roostaei and Jahed showed that Smith-Watson-Topper (SWT) and Jahed-Varvani JV parameters yield acceptable life prediction for AM30 extrusion along the different loading directions [12]. The prediction was made by a single set of material parameter extracted in one specific direction to assess the model's insensitivity to the loading direction (Figure 2-9). The conducted literature review divulged that the ability of energy-based models to correlate fatigue life, independent of test controlling parameter, i.e., stress or strain, remains unknown for Mg alloys.

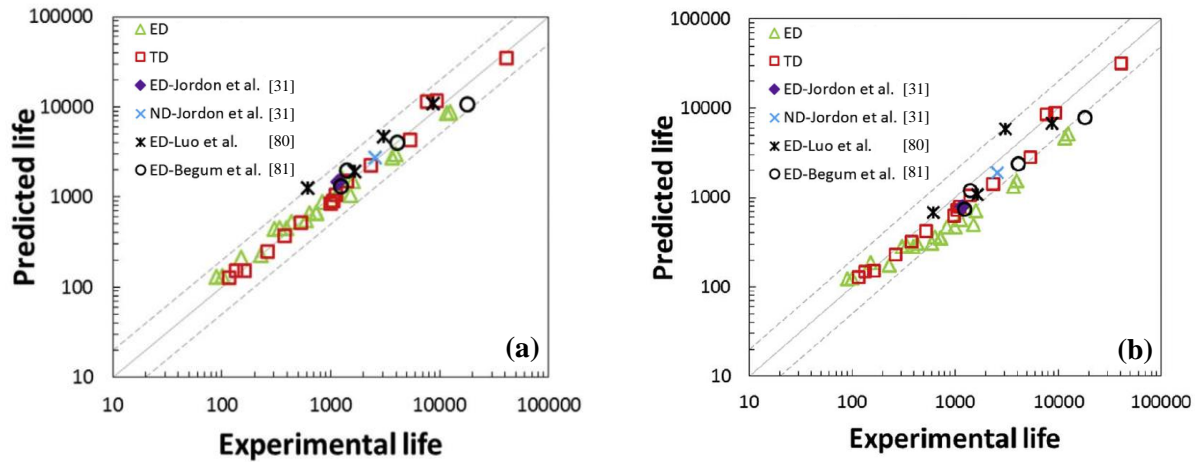


Figure 2-9. Life prediction of AM30 extrusion by: a) JV and b) SWT [12,31,80,81]

2.2.3 Notch Effects on the Fatigue of Mg Alloys

The early investigation on notch sensitivity of Mg alloys goes back to decades ago when Found reported the notch sensitivity of some commercial Mg alloys, including AZ31, AZ61, and AZ80 extrusion [82]. His experiments incorporate cyclic rotary-bending, plate-bending, and axial loading. Sonsino and Dieterich [83] quantified the notch sensitivity of AZ91 HP, AM50 HP, and AM20 HP cast alloys while looking into their fatigue design characteristics under both constant and variable amplitude loadings. The higher notch sensitivity of the investigated Mg alloys in comparison with aluminum, cast-nodular iron, and wrought steels is illustrated in Figure 2-10.

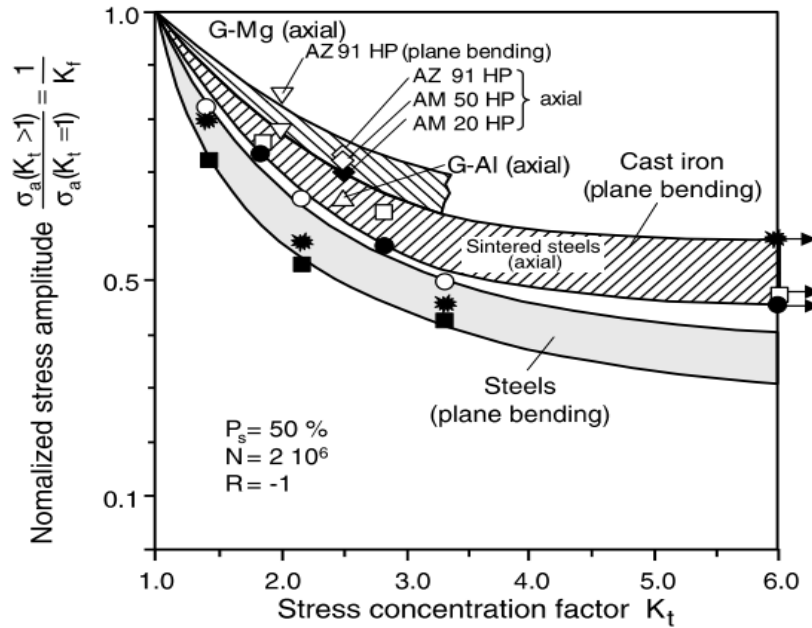


Figure 2-10. K_f correlation with K_t for different Mg, aluminum, and steel alloys [83]

K_f value is expected to fall within 1 and K_t . However, the way it changes in relation to K_t is noteworthy. This correlation is illustrated in Figure 2-11 for cast AM60, where the slight difference between K_t and K_f by increasing K_t tends to exceedingly elevate at higher K_t values [84]. Zhang et al. [85] reported the notch sensitivity of wrought AZ80 to be about 100% at 10^7 cycles by comparing the stress-life curves of smooth and notched specimens (Figure 2-12). The result is in agreement with those obtained by Kuester [86] and Wollmann [87].

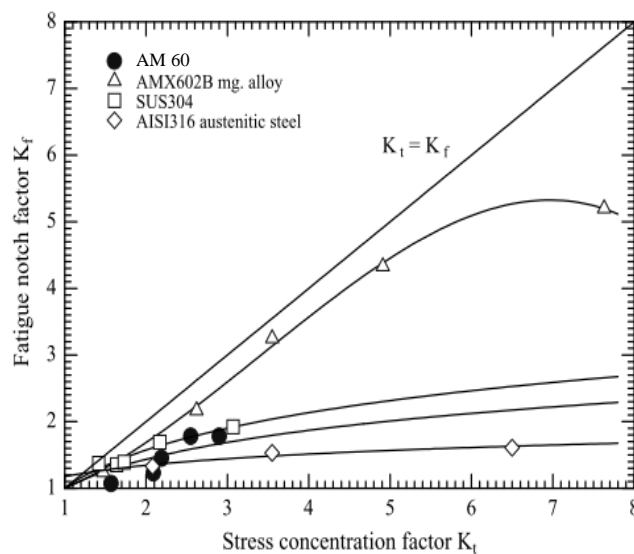


Figure 2-11. K_f vs. K_t for AM60 cast and AMX602B Mg alloys and comparison with SUS304 and AISI316 steel alloys [84]

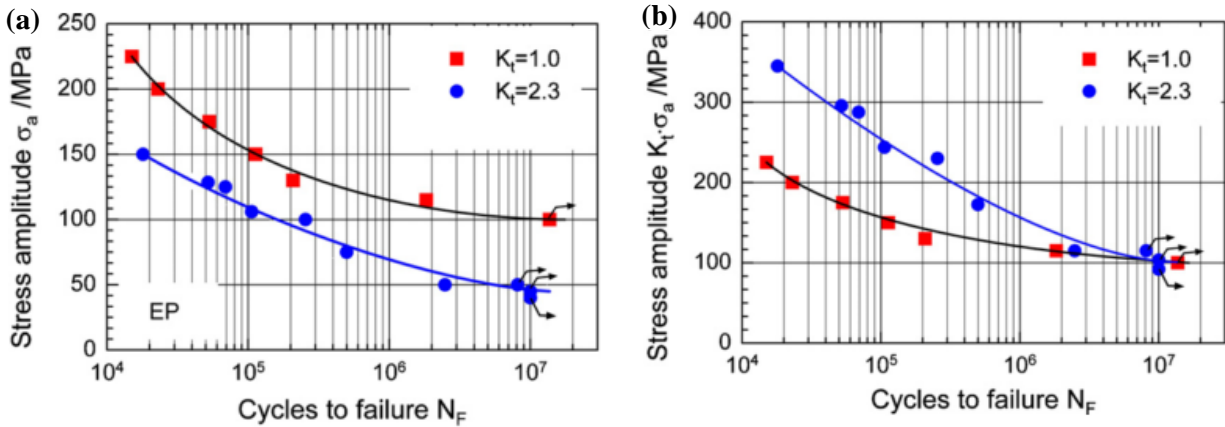


Figure 2-12. Stress–life curves of AZ80 for notched and un-notched specimens: a) nominal stress and b) elastic notch root stress [85]

Denk et al. [88] scrutinized the quasi-static and fatigue characteristics of notched roll-cast AM50 at four different stress concentration factors, with distinctive consideration of the bands of twinned grains (BTGs) formation. The basal texture of rolled AM50 facilitates the twinning activation in compressive reversals. As a consequence, in the low cycle fatigue regime where the twinning/detwinning is the prominent deformation mechanism, the superficial wedge-shape BTGs are formed adjacent to the notch (Figure 2-13).

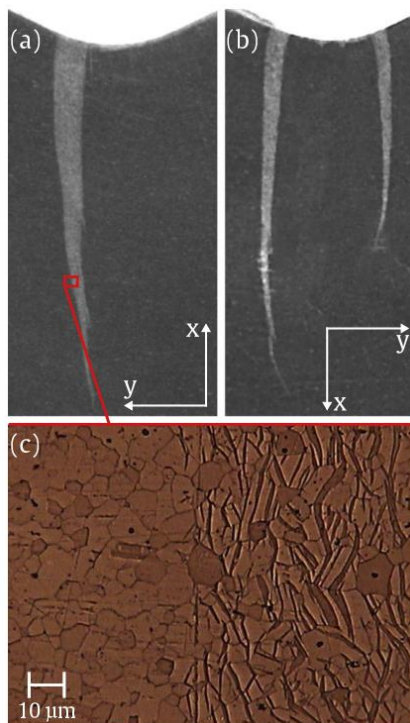


Figure 2-13. BTGs formation in the vicinity of the notch root due to high compressive loading: a), b) macroscopic level, and c) microscopic level at the boundary of the BTG [88]

BTGs locally and excessively boost the strain and impose an advantageous compressive residual stress/strain in the next tensile loading, as shown in Figure 2-14. Thus, BTGs formation in LCF diminishes notch sensitivity significantly. Nevertheless, AM50 remains highly notch-sensitive in the HCF regime, due mainly to the BTG absence (Figure 2-15)

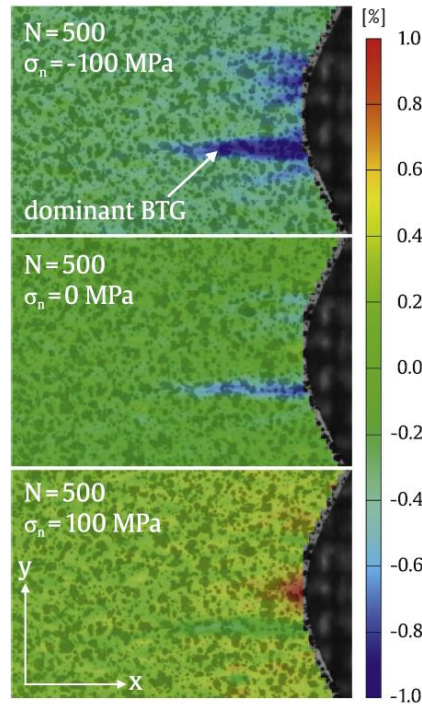


Figure 2-14. Strain distribution near the notch showing the localized negative strain in compressive loading and the consequent residual strain in the next tensile loading [88]

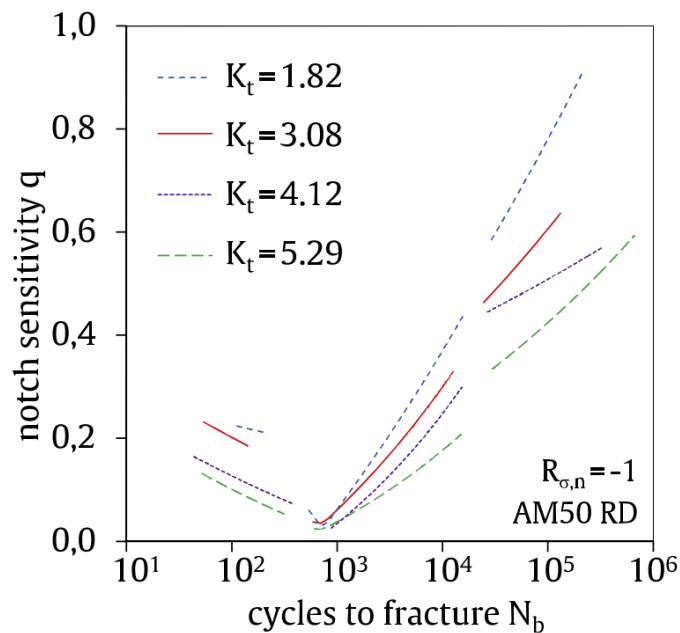


Figure 2-15. Notch sensitivity evolution as the function of cycles to failure for AM30 [88]

Post-manufacturing treatments, such as heat treatment or shot-peening, may alter the notch sensitivity of Mg alloys. Liu et al. [89] compared the notch sensitivity of hot-extruded ZK60 Mg alloy against its T5 aging treated alloy (ZK60-T5) along the extrusion direction. They showed that T5 treatment brings about 6.8% and 6.2% higher notch sensitivity for $K_t=2.3$ and 2.7, respectively (Table 2-1). The improved fatigue properties of T5 treatment over the as-received condition for both notched and un-notched specimens of ZK60 are shown in Figure 2-16. Unfortunately, all of the studies on the notched wrought Mg alloys have been limited to the forming direction, which highlights the lack of understanding on the anisotropic notch sensitivity of these alloys.

Table 2-1. Notch sensitivity of ZK60 and ZK60-T5 [89]

Alloy	K_t	Fatigue strength (MPa)	q (%)
ZK60	1	140	NA
	2.3	150	88
	2.7	160	80
ZK60-T5	1	150	NA
	2.3	155	94
	2.7	165	85

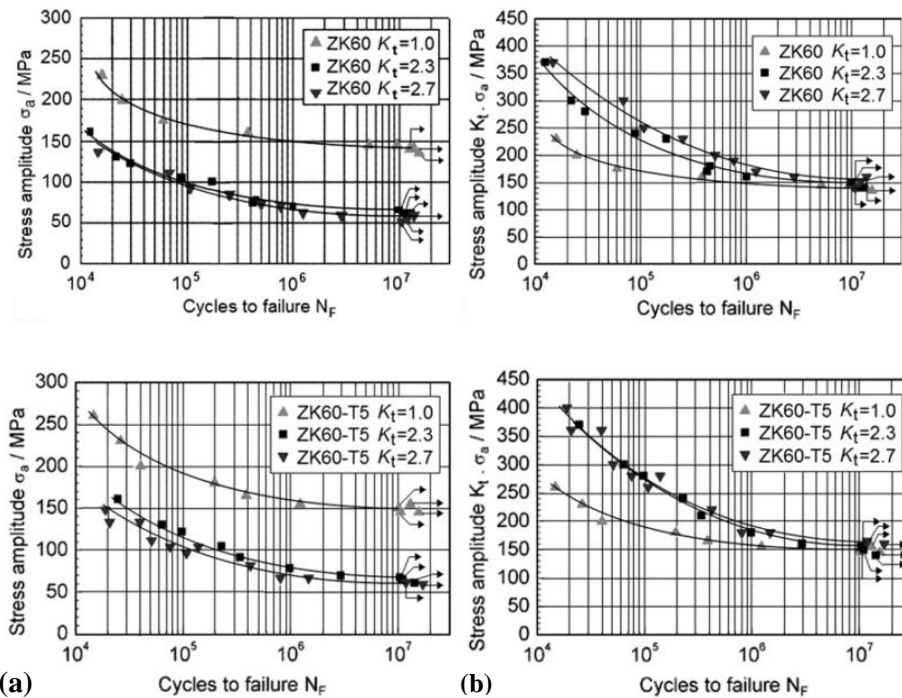


Figure 2-16. Stress–Life curves for ZK60 (top) and ZK60-T5 (bottom) for un-notched and notched specimens: a) nominal stress and b) elastic notch root stress [89]

2.3 Summary

In spite of the increasing trend of Mg application over the last decade, numerous technical restrictions still limit Mg alloy's extensive implementation in industry. For instance, many mechanical behaviors of Mg alloys are still unknown, which make them risky options for manufacturers who prefer to be well-informed about raw materials' characteristics so as to maximize their product reliability. Therefore, life assessment of Mg components via empirical models is needed to expand these alloys' application. The literature review has revealed the potential of energy-based models to be employed in strain- and stress-controlled modeling of wrought alloys. To the best of the author's knowledge, no study is available yet on anisotropic fatigue behavior of notched ZK60 extrusion which is the focal point of this research.

Chapter 3

Quasi-static and Cyclic Strain-control Behavior

This investigation begins with the microscopic characterization of ZK60 extrusion. The cyclic behavior of the material, including its strain-life and stabilized strain-stress response together with the fractographic observations, will be presented and rigorously discussed along three different directions; namely, ED, RD, and 45° to ED (45°). Finally, the merits of SWT as a critical plane and JV as an energy-based model will be assessed based on their capability of mimicking experimental data.

3.1 Material and Specimens

The material investigated in this study, ZK60A Mg alloy in the form of an extruded cylindrical billet with a 127mm diameter, has the chemical composition of Zn 5.5%, Zr 0.71%, other 0.3%, and the balanced weight percent of Mg. The static and fatigue specimens' geometry is depicted in Figure 3-1 (a) and (b). In order to investigate the anisotropy effect of loading directions, specimens were extracted along three distinctive directions, labeled ED, RD, and 45°, such that gage sections were located at the same radius for all samples. The reference cylindrical coordinate system for specimen extraction relative to the extruded billet is illustrated in Figure 3-2, where ED, TD, and RD denote the extrusion, tangential and radial directions, respectively.

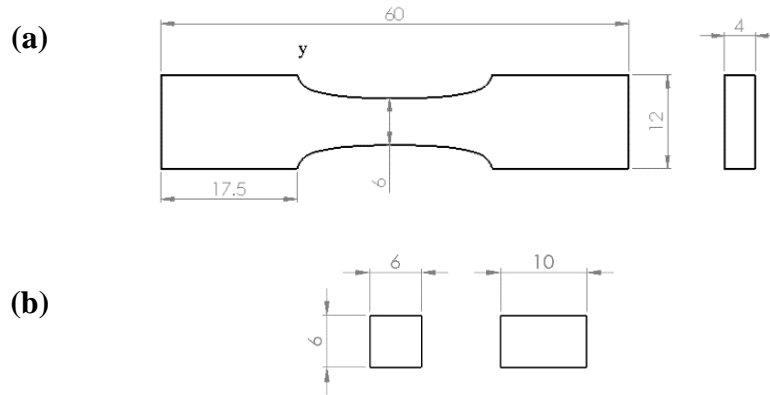


Figure 3-1. a) Static tension and fatigue tests specimens' geometry; b) Static compression tests specimen geometry

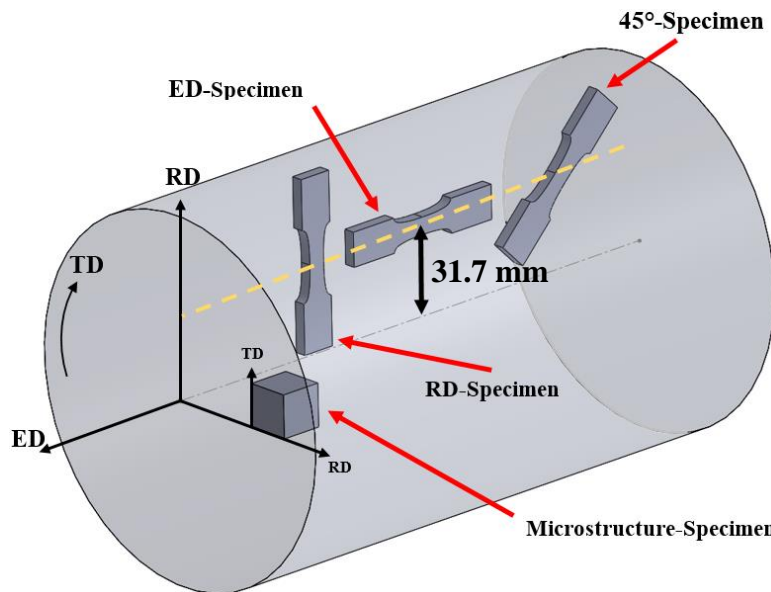


Figure 3-2. Reference cylindrical coordinate system for sample extraction (Dimensions are in “mm”)

3.2 Experimental Procedures

For microstructural observation, samples were prepared through the following standard metallographic procedure. First, they were ground using silicon carbide papers with grit No. up to 1200 and polished sequentially with 6, 3, 1 and 0.1 micron diamond pastes. In order to reveal the grain/twin boundaries, etchant made of 4.2 g picric acid, 70 ml ethanol, 10 ml acetic acid, and 10 ml distilled water was applied to the sample surface.

The crystallographic texture was characterized by means of X-ray diffraction employing Bruker D8 Discover X-ray diffractometer equipped with advanced 2D-detector. The characterization started with incomplete pole figures measurement in the back-reflection mode applying $\text{CuK}\alpha$ radiation at 40 kV-40 mA. The complete pole figures were calculated from incomplete pole figure using DIFFRAC.texture software.

Quasi-static tests were conducted on Instron 8872 servo-hydraulic axial test frame with 25kN load capacity at the ambient temperature. Dog-bone and cuboid samples were used for the static tension and static compression tests, respectively. In these tests, displacement was controlled in order to maintain the strain rate at 0.015 mm/mm/min in accordance with ASTM E8 [90], while the strain was measured using digital image correlation (DIC) technique.

Fully reversed strain-controlled fatigue tests were performed on the same Instron test frame. These tests were conducted at different strain amplitudes, ($R=-1$) ranging from 0.2 to 2 %, with at least two trials at each amplitude. The test frequency was selected based on the applied strain amplitude, varying from 0.1 Hz to 10 Hz, to guarantee precise control of the sinusoidal waveform of the strain. The strain was measured by Instron extensometer with 10 mm gauge length and ± 1 mm travel. The fatigue failure was set at 50% drop in the peak tensile force of the stabilized cycle or the final fracture and the test is considered run-out if the sample survives for more than 1 million cycles. To understand the fracture mechanism, selected fracture samples were analyzed using SEM.

3.3 Results

3.3.1 Microstructure Analysis

The microstructural examination of ZK60 extrusion, shown in Figure 3-3, disclosed the twin-free bimodal grains, i.e., sizable elongated and small equiaxed grains. Similar microstructural characteristics have been reported for this material [11,52].

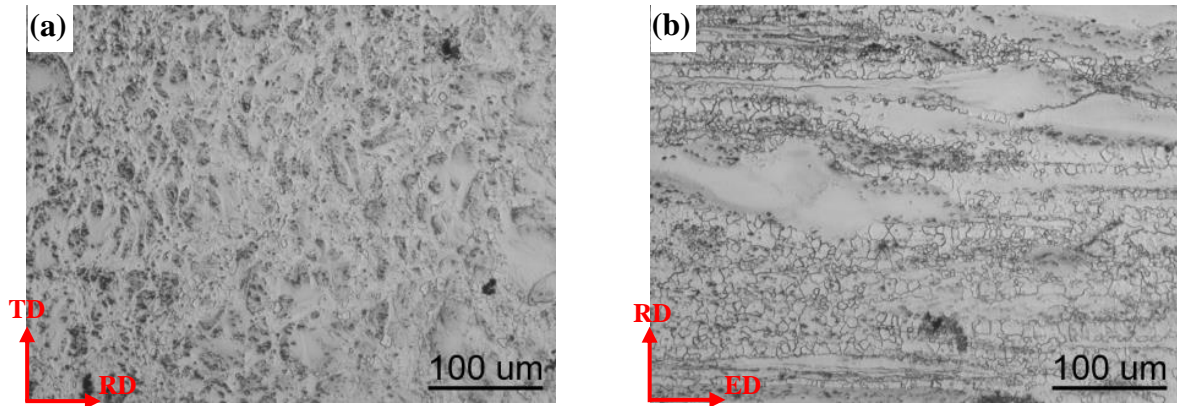
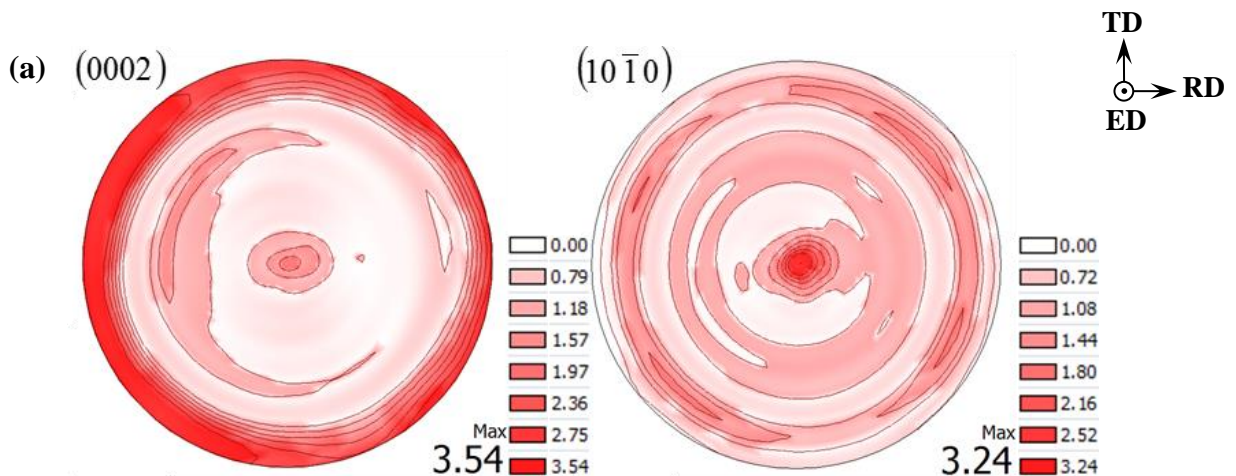


Figure 3-3. Typical microstructure of ZK60 extrusion; (a) TD-RD plane and (b) RD-ED plane

The pole figures, plotted for both RD-TD and ED-RD planes in Figure 3-4, revealed that the majority of the *c*-axes are oriented approximately perpendicular to the ED, but not necessarily parallel to the RD or TD. The crystallographic orientation matches those observed in earlier studies on ZK60 extrusion [52,63]. This can favor $\{10\bar{1}2\}$ extension twinning under compression loading in ED samples [6,63]. The effect of this texture on quasi-static and cyclic behaviors will be thoroughly discussed later.



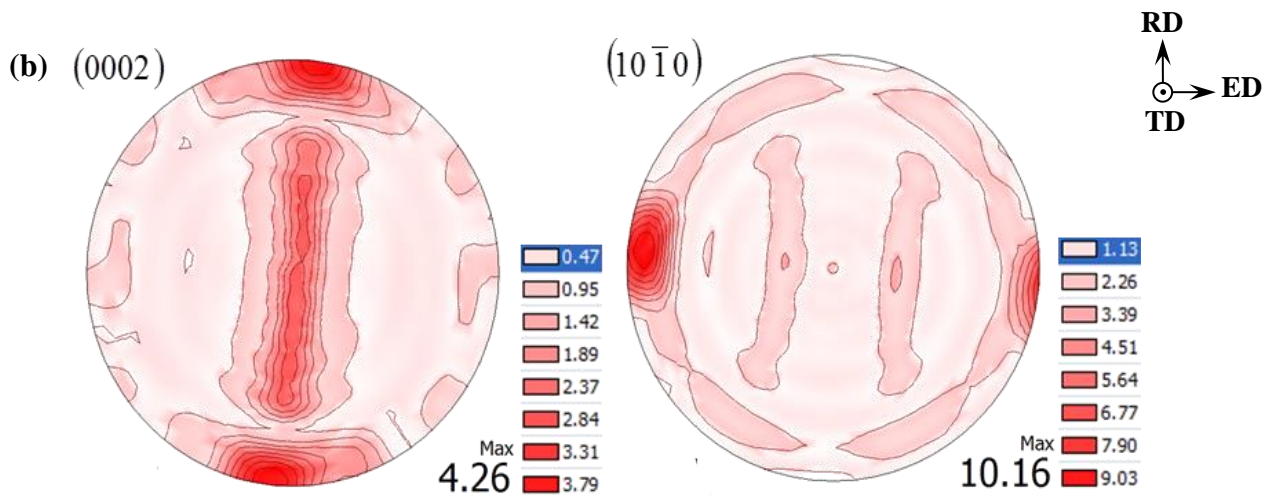


Figure 3-4. (0002) and (10 $\bar{1}$ 0) pole figures of ZK60 extrusion obtained from; (a) TD-RD plane and (b) ED-RD plane

3.3.2 Quasi-static Tension and Compression Behavior

Figure 3-5 illustrates the engineering stress-strain curves for ZK60 extrusion under quasi-static tensile and compressive loadings along different directions. It is seen that the tensile and compressive yield strengths along ED are 251 MPa and 128 MPa, respectively. In contrast, similar yield strengths are observed along the other two directions, i.e. the average yield strengths of 130 MPa and 136 MPa, along RD and 45°, respectively.

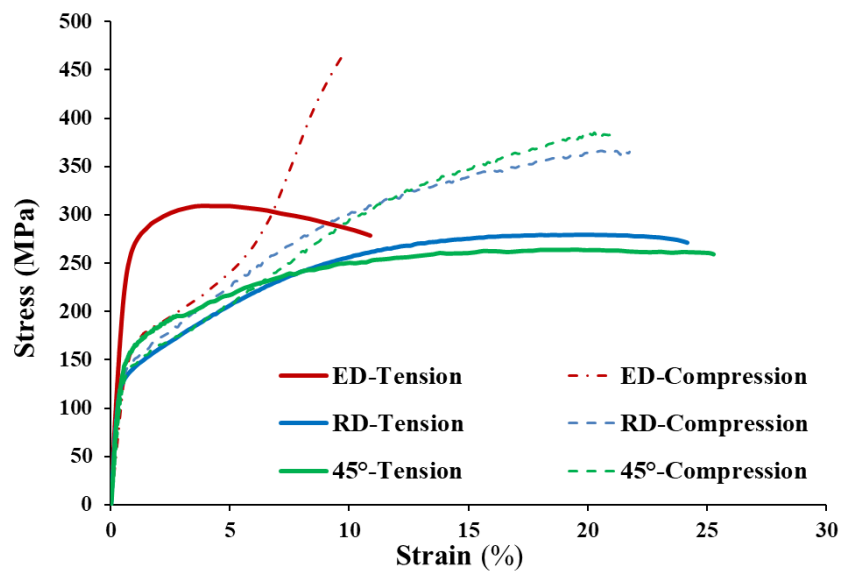


Figure 3-5. Quasi-static behavior under tensile and compressive loading for ED, RD, and 45°

Table 3-1 summarizes the quasi-static mechanical properties of the material along these directions. Two tests were averaged to get the value for each property. The ductility along ED is less than that along RD and 45°, which is in agreement with the texture results, indicating that the c-axis of the grains are perpendicular to the ED. Hence, less number of slip modes can be activated to accommodate the strain.

Table 3-1. Quasi-static mechanical properties of ZK60 extrusion along different directions (The numbers in the parentheses are standard deviations)

Mechanical properties	ED	RD	45°
Module of elasticity [GPa]	43 (1)	45 (0)	42 (1)
Tensile yield strength [MPa]	251 (0)	128 (0)	149 (2)
Tensile ultimate strength [MPa]	309 (1)	279 (1)	264 (1)
Ductility (%)	11 (0)	23 (1)	26 (0)
Compressive yield strength [MPa]	128 (10)	132 (4)	123 (5)
Compressive ultimate strength [MPa]	449 (15)	357 (9)	388 (3)

3.3.3 Cyclic Behavior

3.3.3.1 Extrusion Direction

Figure 3-6 depicts the typical engineering stress-strain hysteresis loops of the stabilized cycles for total strain amplitudes between 0.2% and 2% for the ZK60 extrusion along ED. It is observed that the hysteresis loops for the strain amplitudes lower than 0.5% are not sigmoidal. On the contrary, increasing the strain amplitudes to more than 0.5% brings about a sigmoidal-shape hysteresis loop. Such asymmetry indicates the activation of twinning and detwinning upon compressive and tensile reversals, respectively [91].

To be more specific, the evolutionary change of hysteresis loops from the second cycle to the stabilized cycle is depicted in Figure 3-7. One of four distinct behaviors is applicable depending on the applied strain amplitude: (i) symmetric without twinning (ii) partially asymmetric (iii) asymmetric, and (iv) “leading-to-symmetric” behavior.

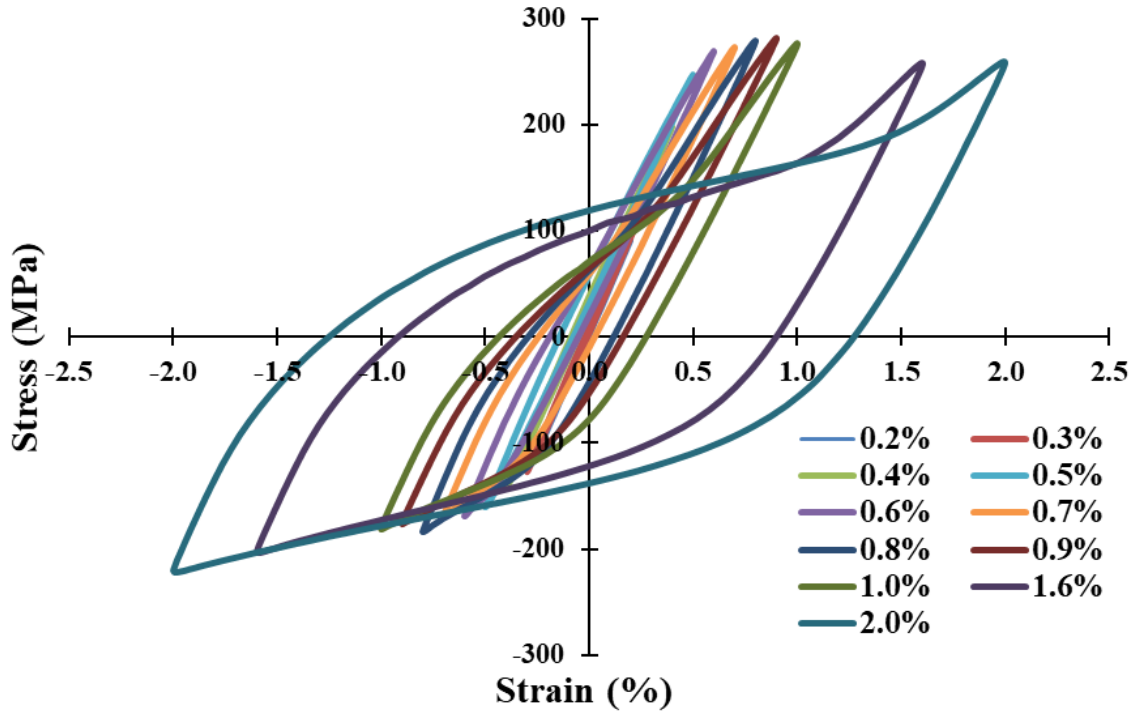


Figure 3-6. Typical engineering stress-strain hysteresis loops of the stabilized cycle for ED ranging from 0.2% to 2% strain amplitudes

First, at low strain amplitudes (lower than 0.4%), the stabilized hysteresis loops are symmetric, implying that the stress is insufficient to activate extension-twinning under compression loading [92]; At such low strain amplitudes, the deformation mechanism is controlled by the gliding of dislocations [6]. Moreover, marginal cyclic hardening is observed in Figure 3-7 (a), probably due to the increased density of dislocations with the increasing number of cycles [93]. For the strain amplitudes of 0.5%, Figure 3-7 (b), the hysteresis loop at the second cycle is asymmetric in tension and compression reversals, denoting that twin and detwin deformations are active. Activation of the extension twin in a compression reversal results in an 86.3° rotation in crystal orientation [94]. Therefore, the twinned grains are likely to detwin during the subsequent tension reversal [6]. Nevertheless, the twinned grains in the compression reversal are not fully detwinned in the following tension reversal, leading to the formation of residual twins and cyclic hardening [42]. However, the hysteresis loop at the stabilized cycle exhibits no sign of twinning dominance, and therefore the slip of dislocations is accommodating the applied strain. It is believed that this change in the deformation behavior is due to the exhaustion of the new extension twin. This behavior has already been observed in ZK60 [11] and AM30 [12] along ED.

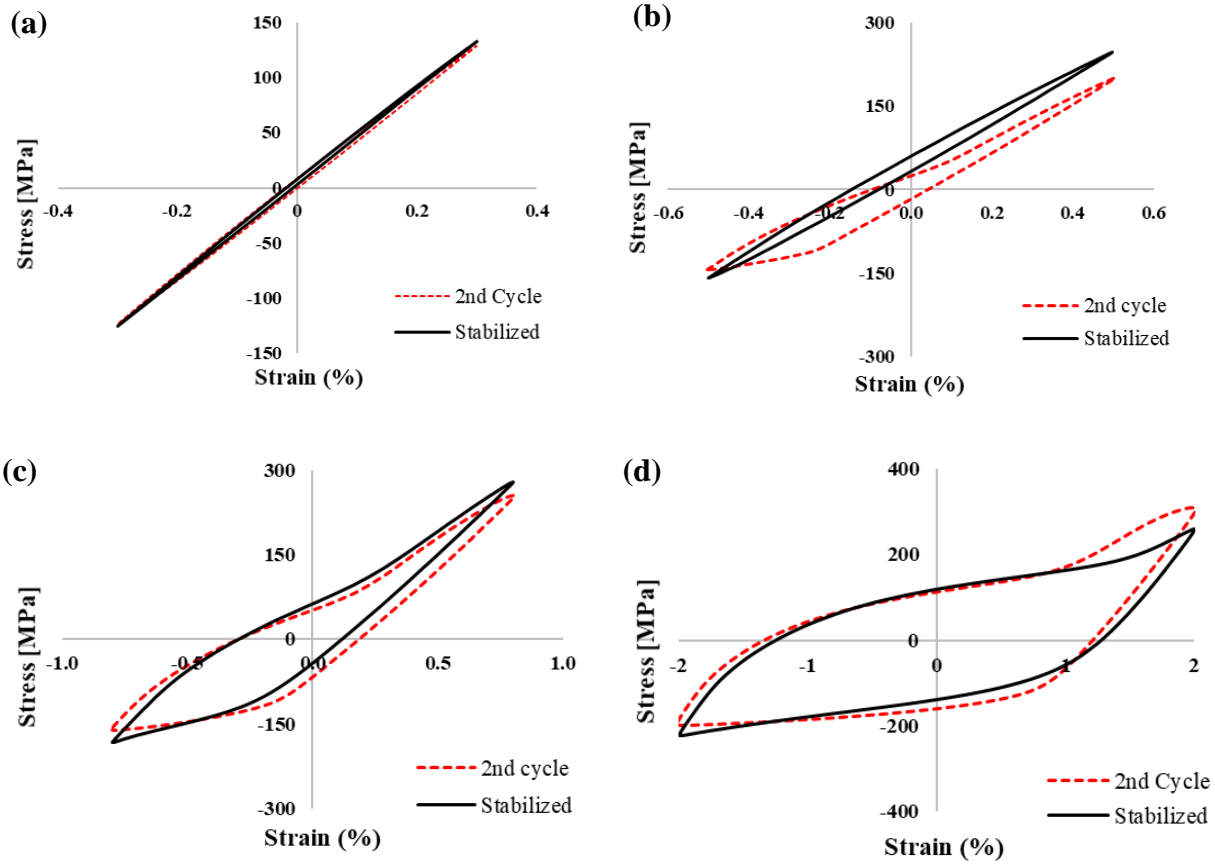


Figure 3-7. Evolution of hysteresis loops for 2nd and stabilized cycles along ED at different strain amplitudes: (a) 0.3%, (b) 0.5%, (c) 0.8%, and (d) 2%

As the applied strain amplitude is increased (to more than 0.5%), Figure 3-7 (c), the stresses during compressive reversals are high enough to activate the extension twinning. The twinned grains formed under compression are partially detwinned in the next tensile reversal, resulting in residual twins. These residual twins build up resistance to the plastic deformation in the wake of their interactions with dislocations and twinned grains which brings about cyclic hardening [6][95]. Lastly, when the strain amplitude reaches to as large as 2%, Figure 3-7 (d), twinning governs the plastic deformation in the compressive reversal of the first few cycles. During the tensile reversal, detwinning occurs inside the twinned grains, and after detwinning exhausts, non-basal slips accommodate strain [48]. As a result, the hysteresis loop for the second cycle is sigmoidal for the tensile reversal. However, as the number of cycles increases, the compressive reversal also tends to the sigmoidal shape, as twinning is exhausted before the end of compressive reversal. The subsequent concave-down curve is as a result of the competitive twinning and slip

mechanisms [62]. In contrast, the tensile reversal demonstrates cyclic softening, which is due to the formation of non-propagating micro-cracks in the first few cycles at such a high strain amplitude [96]. It is also reported that the annihilation and rearrangement of dislocations can cause this softening [6]. As a result of cyclic hardening in the compressive reversals and cyclic softening in the tensile reversals, hysteresis loops tend to be tension-compression symmetric. Similar behavior has been observed in AM30 extrusion for strain amplitudes greater than 1.5% [12].

3.3.3.2 Radial direction

Typical engineering stress-strain hysteresis loops along RD for ZK60 extrusion are plotted in Figure 3-8 at different strain amplitudes ranging from 0.2% to 2%. At all strain amplitudes, the hysteresis loops are roughly symmetric, unlike those in the ED. Slip is the dominant deformation mechanism at small strain amplitudes; however, twinning is also happening at high strain amplitudes ($\epsilon_a \geq 1.6\%$) and forms sigmoidal-shape hysteresis loops. It is also observed that the peak stresses in the compression reversals are larger than those in the tension ones. As indicated in Figure 3-9, there is no such a difference between the second hysteresis and the stabilized one along RD. This is because of the lack of residual twins in this direction in the microstructure, the reason of which will be discussed later. Thus, larger compressive peak stresses comparing to the tensile ones stem from the quasi-static behavior. Returning to section 3.3.2 and Table 3-1, it was stated that along RD, the compression yield strength is greater than the tension yield; thereby, higher peak stress is eventually achieved under compression reversal.

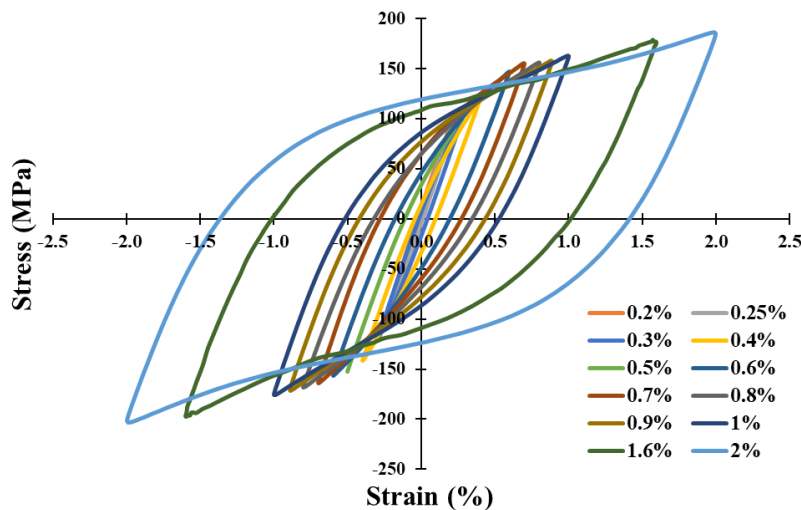


Figure 3-8. Typical engineering stress-strain hysteresis loops of the stabilized cycle for RD ranging from 0.2% to 2% strain amplitudes

According to Figure 3-9, at the strain amplitude of 1%, the second and stabilized hysteresis loops do not show a remarkable decrease of hardening rate under compressive reversal, indicating that twinning is not happening massively. In fact, the crystal orientations in some grains favor the activation of extension twinning under both reversals, and consequently, detwinning reorients part of the twinned grains under both tension and compression loading. As a result, few residual twins remain in the microstructure; hence, slight strain hardening occurs both in tension and compression reversals due to the twin-twin and twin-dislocation interactions. On the other hand, as the strain amplitude is increased to 2%, the non-basal slip modes are activated in addition to the twinning and detwinning, which results in the sigmoidal hysteresis loop. However, for the reason mentioned before, only a limited number of residual twins remain in the microstructure, and by comparing the stabilized and second cycle hysteresis loops, very marginal cyclic hardening can be observed.

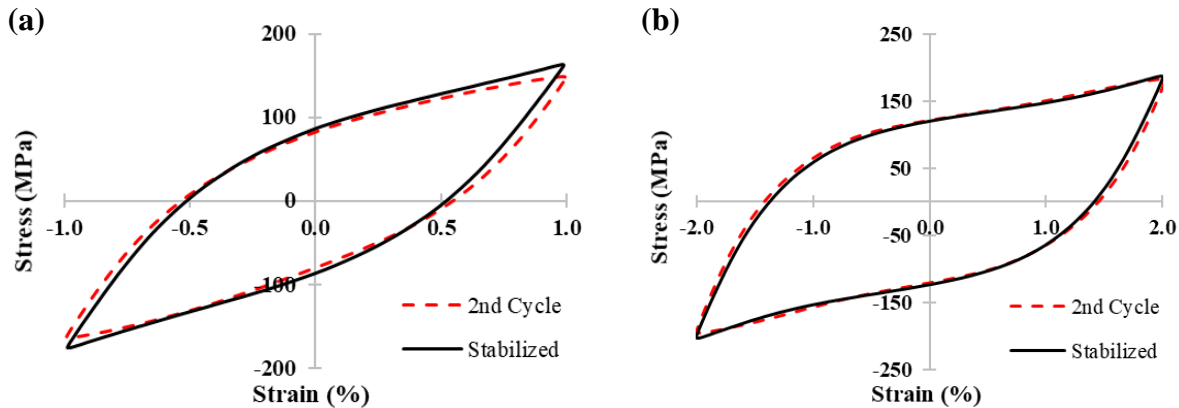


Figure 3-9. Evolution of hysteresis loops for 2nd and stabilized cycles along RD at the strain amplitude of: (a) 1% and (b) 2%

3.3.3.3 45° direction

Figure 3-10 shows the typical engineering stress-strain hysteresis loops along 45° for ZK60 extrusion at strain amplitudes ranging from 0.3% to 2%. The stabilized fatigue response, like the one along RD, does not show a low-hardening section under compressive and tensile reversals up to the strain amplitude of 1%. However, the sigmoidal behavior along 45° differs from that along RD, i.e., the peak stresses and strain hardening are slightly higher in tension reversals. This, again like RD, is stemming from the quasi-static behavior of 45°.

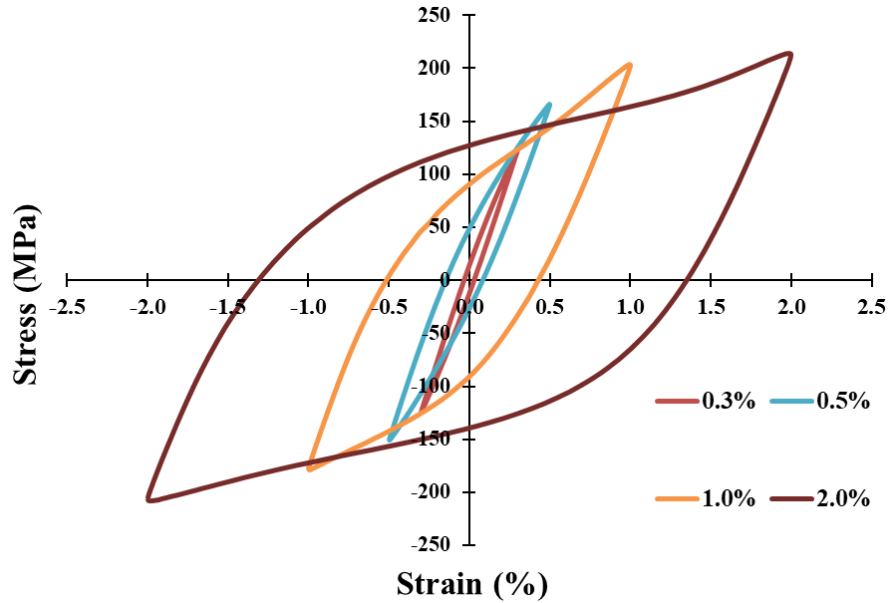


Figure 3-10. Typical engineering stress-strain hysteresis loops of the stabilized cycle for 45° direction ranging from 0.3% to 2% strain amplitudes

Hysteresis loop evolution along 45° is shown in Figure 3-11. As seen in Figure 3-11 (a), the hysteresis loop evolution along 45° at the strain amplitude of 1% is similar to that along RD; i.e., very marginal cyclic hardening is observed under both tension and compression loading. However, at the strain amplitude of 2%, Figure 3-11 (b), the behavior is more similar to that in the ED direction; i.e., after the first few cycles, cyclic softening on the tensile side and cyclic hardening on the compressive side can be seen. However, in the case of 45°, softening is not as severe as that along ED.

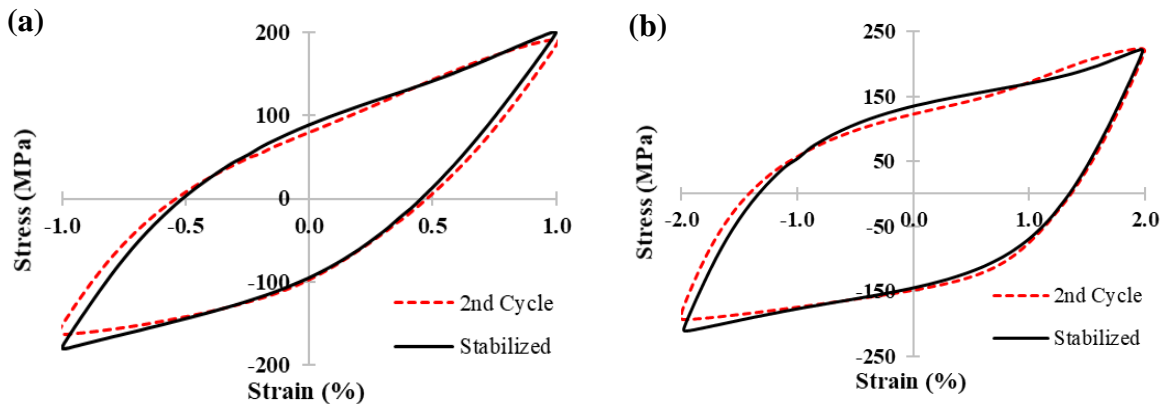


Figure 3-11. Evolution of hysteresis loops for 2nd and stabilized cycles along 45° direction at the strain amplitudes of: (a) 1% and (b) 2%

3.3.4 Strain-life Curve

The strain-life (ϵ_a-N) curves for ZK60 extrusion along different directions are depicted in Figure 3-12. It is noteworthy that both the 45° and RD samples are displaying the same life at different strain amplitudes. Moreover, comparing the fatigue responses along RD and ED, it is noted that the lives are similar for the strain amplitudes of 0.4% and higher (the low cycle fatigue regime). However, in the high cycle fatigue regime (strain amplitudes of 0.3% and lower), the cyclic response depends on the material direction. For instance, while the fatigue life at the strain amplitude of 0.3% along RD is ~ 27000 cycles, that for ED is improved to ~ 100,000 cycles. While the run-out test for ED happened at the strain amplitude of 0.25%, RD samples exhibited an average life of 90,000 cycles at the same strain amplitude. The run-out test for RD was achieved at 0.2%. The reasons for the similar fatigue performance in the LCF for all directions, but not in the HCF will be discussed later.

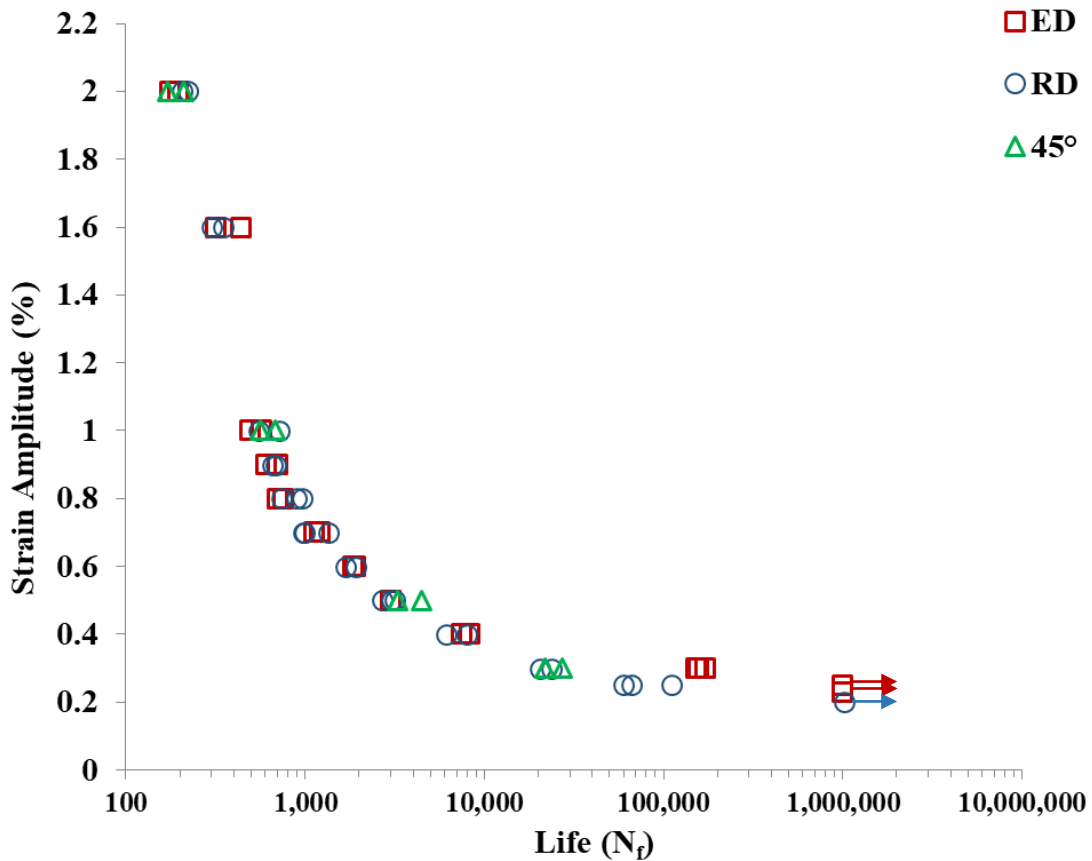


Figure 3-12. A comparison of strain-life (ϵ_a-N) curves obtained from different directions for the ZK60 extrusion

3.3.5 Fatigue Fracture Surfaces

The SEM images of the fatigue fracture surface of ED, RD, and 45° samples at two strain amplitudes of 0.3% and 2% are presented in Figure 3-13. Multiple crack initiation sites (marked by yellow arrows) are visible for all directions at the higher strain amplitude, whereas crack initiation sites are fewer at the lower strain amplitude. The fatigue failure (FF) area is distinguished from the fatigue crack growth (FCG) zone by dashed lines, and generally, at lower strain amplitudes, the FCG area is larger, manifesting a longer fatigue life.

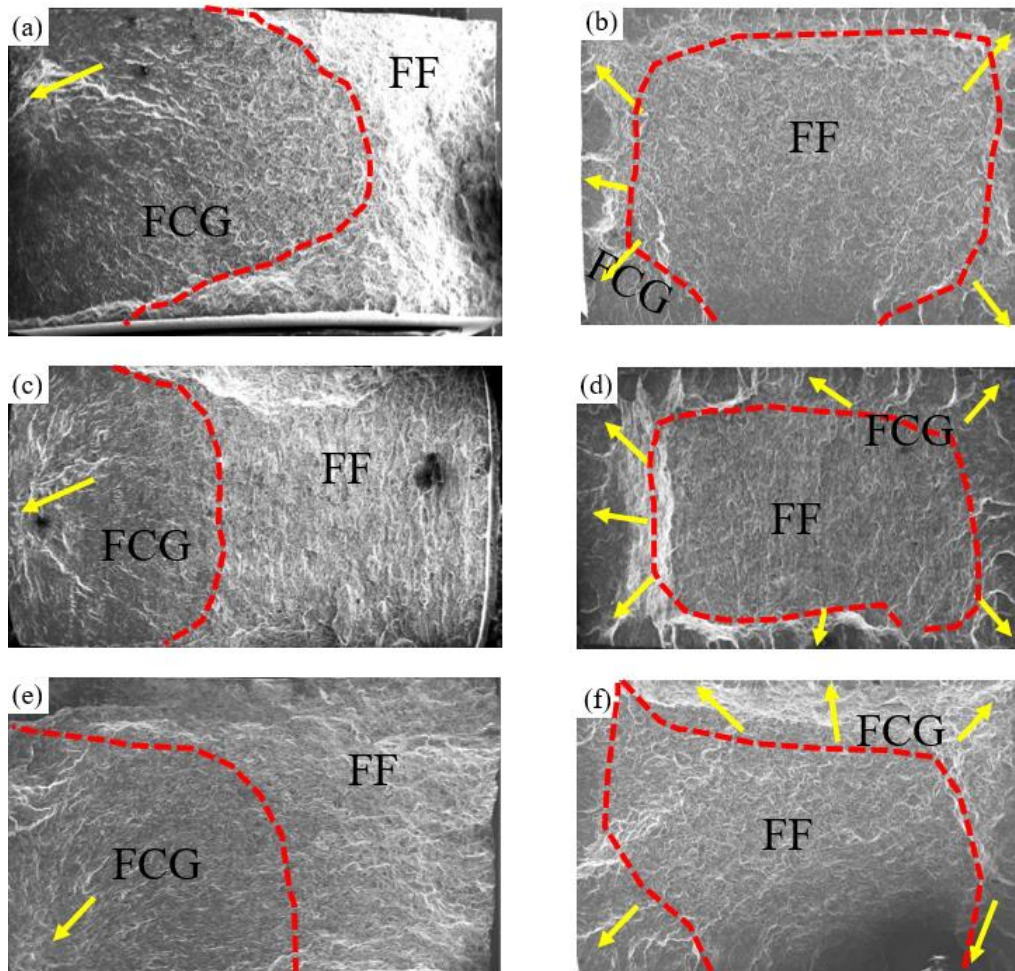


Figure 3-13. SEM images of fatigue fracture surfaces of ZK60 extrusion Mg alloy at different strain amplitudes along different directions: (a) ED at $\epsilon_a=0.3\%$, (b) ED at $\epsilon_a=2\%$, (c) RD at $\epsilon_a=0.3\%$, (d) RD at $\epsilon_a=2\%$, (e) 45° at $\epsilon_a=0.3\%$, and (f) 45° at $\epsilon_a=2\%$, (Yellow arrows indicate the position of FCI sites, and the dashed lines represent the boundary between the FCG and the FF areas)

The fracture surfaces at higher magnifications are shown for the strain amplitude of 2% along different directions in Figure 3-14. Twin lamellae are observed on the fracture surface of ED samples, whereas fracture surface for RD sample reveals slip bands (SB).

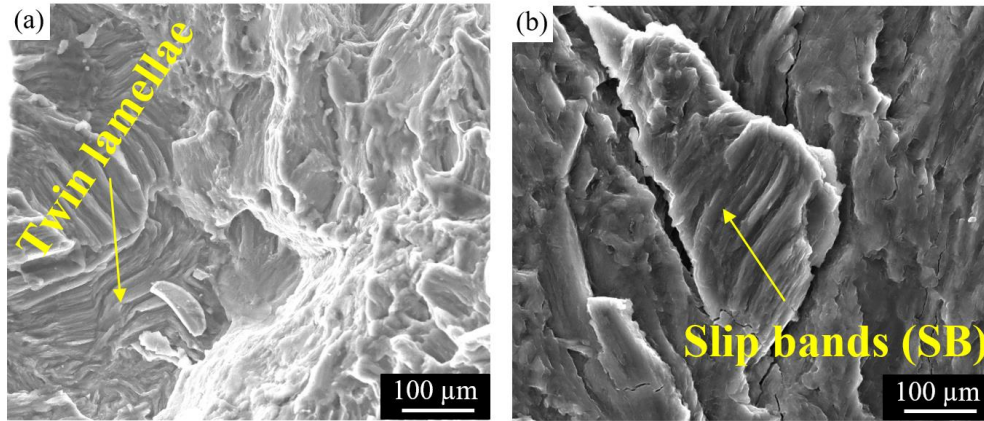


Figure 3-14. SEM images of the fracture surface of ZK60 extrusion at the total strain amplitude of 2% showing twin lamellae and slip bands on the: (a) ED sample and (b) RD sample

Also, Figure 3-15 illustrates the fatigue crack growth (FCG) zone of ZK60 at the total strain amplitudes of 0.3% and 2%. Fatigue striations (FS) marks are denoted on the images. Each striation mark represents the propagation of the fatigue crack in one cycle. Hence, the finer the marks, the longer the fatigue life. While the average distance between the FS marks for the ED sample under strain amplitude of 0.3% was $0.6\pm 0.16\ \mu\text{m}$, the RD and 45° samples exhibited striations with an average distance of $1.92\pm 0.3\ \mu\text{m}$, which is a testimony to the longer fatigue life along ED. In contrast, the average distance along FS marks along ED, RD, and 45° directions under strain amplitude of 2% were $2.14\pm 0.04\ \mu\text{m}$, $2.01\pm 0.09\ \mu\text{m}$, and $2.21\pm 0.43\ \mu\text{m}$, asserting the similar lives in the LCF regime.

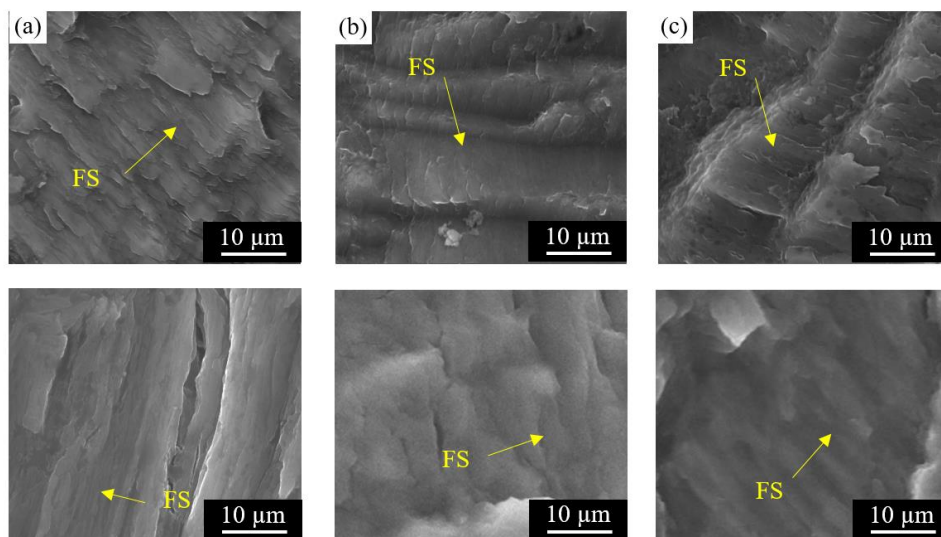


Figure 3-15. Fatigue crack growth at the total strain amplitudes of 0.3% (Top) and 2% (Bottom) for: (a) ED, (b) RD, and (c) 45° samples

Lastly, to be more specific, the microstructure of the fatigue fractured ZK60 Mg alloy tested at the strain amplitude of 2% along (a) ED and (b) RD are shown in Figure 3-16. Profuse twinned grains are observed in the microstructure along ED; however, the twinned area in the RD sample was significantly lower. This is in agreement with the hysteresis loops obtained in section 3.3.3, in that the one for ED samples was less symmetric, as twinning was more dominant.

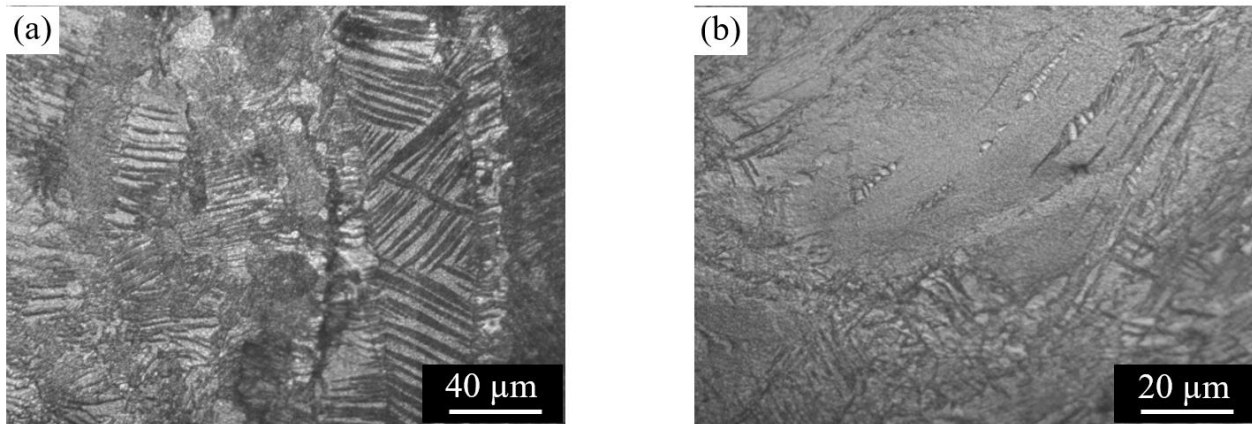


Figure 3-16. Microstructure illustrating the traces of twin on the polished cross-section of the fatigue-tested samples near the fracture surface, obtained at a strain amplitude of 2% along (a) ED and (b) RD

3.4 Discussion

3.4.1 Deformation Behavior

The development of hysteresis responses along different directions during the fatigue tests was illustrated in the previous sections. The mechanical behavior of the material is highly associated with the crystallographic texture, which controls the active modes of deformation. It is well-established that $\{10\bar{1}2\}$ extension-twin can accommodate plastic strain in HCP crystal structures when the applied loading is either tensile along the c-axes of the grains, or compressive perpendicular to the c-axes [6]. This polar nature of twinning brings about evident tension-compression asymmetric behavior in wrought Mg alloys [97]. For ZK60 extrusion, along ED, extension-twinning drives the deformation only under compressive loading. However, for the radial and 45° directions, twinning can happen under both tensile and compressive reversals. Consequently, in each reversal, some of the grains' orientation favors the activation of twinning, while the other pre-twinned grains tend to detwin. Therefore, hysteresis loops along these

directions are less asymmetric compared to ED.

The cyclic tension and compression behaviors of ZK60 along the three directions are depicted in Figure 3-17. The plots are constructed from the peak stresses of the stabilized hysteresis loops. It is noted that both the cyclic tension and cyclic compression curves for 45° are located between the curves of ED and RD. This observation suggests that the deformation mechanism, as a macroscopic consequence of texture, along the 45° direction is a combination of the activated mechanisms along ED and RD.

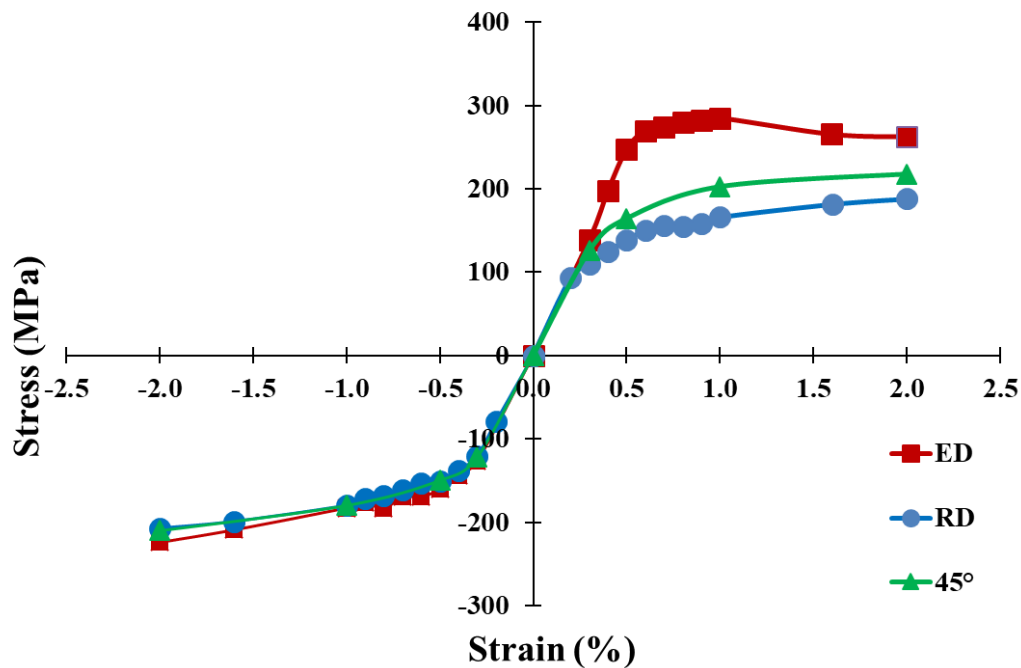


Figure 3-17. cyclic tension and compression behavior along ED, RD, 45°

In Figure 3-18, the term Asymmetric Ratio (AR) = $\frac{TS-CS}{TS+CS}$ refers to the level of asymmetry, where TS and CS are the tensile peak stress and compressive peak stress, respectively. For a symmetric cyclic behavior, the asymmetry level equals zero, whereas the positive and negative levels of asymmetry reveal higher tensile peak stress and higher compressive peak stress, respectively. Asymmetry is clearly evident along ED up to the strain amplitude of 1%, but then decreases drastically, probably due to the formation of micro-cracks, and consequently reduces the tensile peak stress. The annihilation and rearrangement of dislocations, which together can decrease the post-detwinning dislocation-based flow, can also cause this softening, as reported in the literature [62][6][96][15].

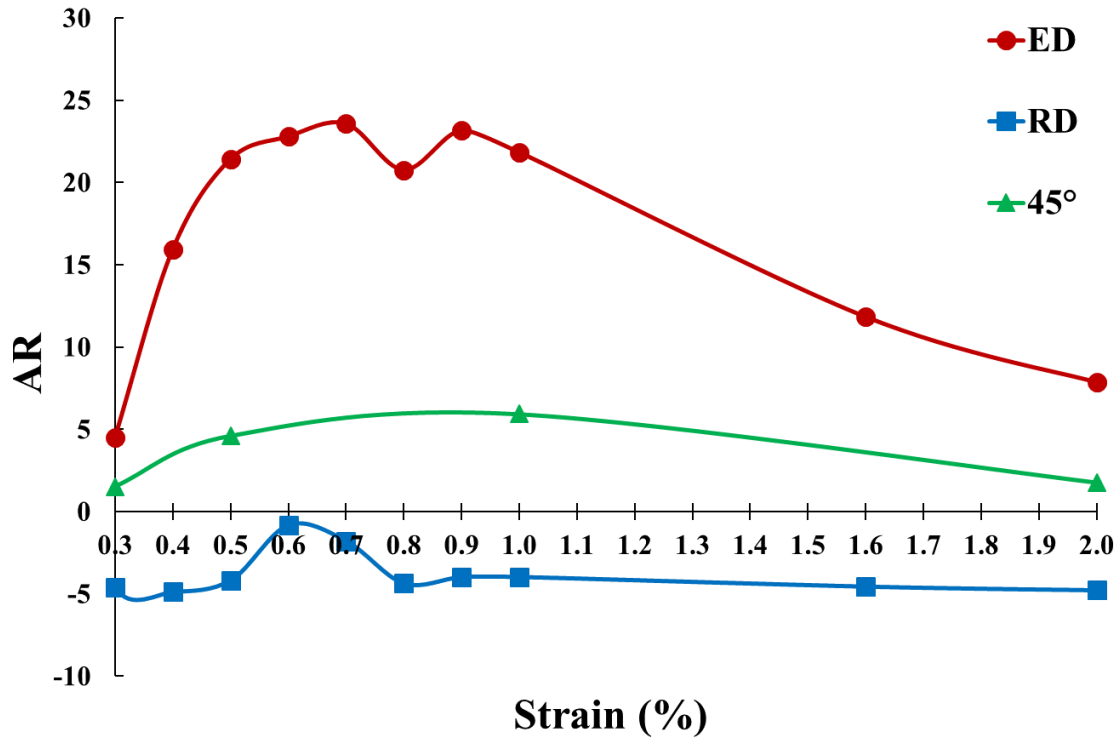


Figure 3-18. Ratio of cyclic asymmetry at different strain amplitudes ranging from 0.3 to 2% for different sample orientations

The RD asymmetry levels do not change remarkably, remaining close to zero, and so manifesting more symmetric behavior than other directions. As discussed, this symmetric behavior arises from the crystallographic texture of ZK60 extrusion, in which the c-axes of grains are randomly orientated on a plane normal to ED. Hence, twinning happens under both tension and compression along RD. Lastly, along 45°, like the deformation curves, the level of asymmetry lies between the ones for ED and RD, signifying that the deformation behavior of 45° is a combination of ED and RD behaviors. Moreover, while the asymmetry level for 45° is not as high as ED's owing to different texture, it decreases like ED's at high strain amplitudes. Referring to the Figure 3-9 this can be attributed to the tension peak stress drops at high strain amplitudes.

The tension and compression cyclic behavior of ZK60 is plotted against the quasi-static behavior under tension and compression loadings along different material directions in Figure 3-19. It is noted that at low strain amplitudes, where the material response is nearly elastic, the quasi-static and cyclic behaviors are very similar. However, at higher strain amplitudes, cyclic hardening occurs in the light of resistance built up by dislocation-dislocation, dislocation-twin,

and twin-twin interactions [62]. Hence, cyclic curves are harder than quasi-static curves for RD and 45°. However, as previously stated, for ED, softening occurs at strain amplitudes higher than 1% probably due to the formation of non-propagating micro-cracks. This affects the fatigue modeling, as will be discussed later.

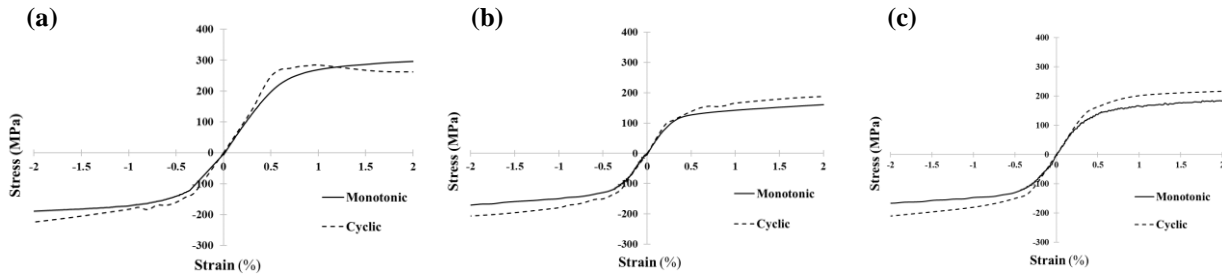


Figure 3-19. Comparison between quasi-static and cyclic curves for ZK60 extrusion along (a) ED, (b) RD, and (c) 45°

3.4.2 Effect of Loading on the Fatigue Performance

Figure 3-12 showed that the fatigue life of ZK60 is not sensitive to the material direction in the LCF regime, i.e., $\varepsilon_a \geq 0.4\%$, although the deformation behavior is different. In other words, the cyclic deformations for RD and 45° are almost symmetric, whereas the deformation for ED involves profound twinning happening only under compressive loading. Thus, significant asymmetry is evident. Nevertheless, the fatigue lives are not direction sensitive in LCF. On the other hand, according to Figure 3-12, fatigue lives within the HCF regime, i.e., $\varepsilon_a < 0.4\%$, are distinct in spite of similar symmetric deformation behavior.

Figure 3-20 demonstrates the hysteresis loops at two different strain amplitudes of 0.5% and 1%, both corresponding to the LCF regime, for different directions. It is noted that while the tensile peak stresses for ED are the highest among all directions for both strain amplitudes, the areas inside the ED hysteresis loop are the least compared to the areas of RD and 45°. The area inside the hysteresis loops represents the energy being dissipated in each cycle. Therefore, less energy would dissipate along ED in each cycle compared to the other two directions, both of which show relatively similar loop areas. On the other hand, the larger tensile peak stress causes larger stress range and tensile mean stress, which are more damaging for ED samples.

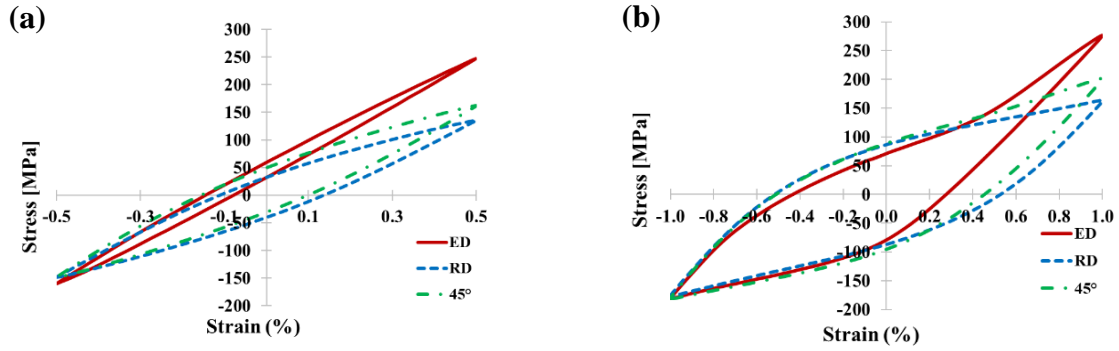


Figure 3-20. Stabilized hysteresis loops for ED, RD, and 45° at: (a) $\epsilon_a = 0.5\%$ and (b) $\epsilon_a = 1\%$

Furthermore, profound residual twins remained in the microstructure of the alloy can affect the fatigue life of ED samples in two ways. Firstly, interactions between twin-twin bands and twin-dislocations can cause crack initiation, leading to a pre-mature fatigue failure [15][98]. On the other hand, some studies have suggested that the surface roughness as a result of extension twinning can retard the crack growth rate due to roughness-induced crack closure [99]. As a result, from a microscopic point of view, although grain sizes along ED are smaller than those in the other directions, leading to higher strength along this direction, in the LCF regime, residual twins remain in the microstructure of ED samples, affecting the mechanical behavior of the material. The overall result of competing factors, namely strength, twin-twin band interactions, the interaction between twin and dislocations, and surface roughness as a result of extension twinning, is that the fatigue lives in the LCF regime are similar. However, in the HCF regime that twinning does not happen, the material strength governs the deformation. In fact, at these strain amplitudes, the area inside the hysteresis loop is small, exhibiting little plasticity in the deformation. Thus, the deformation tends to be more elastic; consequently, the governing fatigue life factor in the HCF regime would be the strength of the alloy. This suggests a remarkably higher fatigue life for ED samples in HCF because crack initiation occurs later due to the higher strength along this direction [100].

3.5 Fatigue Modeling

As discussed, ZK60 extrusion exhibits identical behavior in the LCF regime along three different directions in terms of the strain-life curve; however, in the HCF regime, their fatigue response shows segmental deviation. Furthermore, along the ED, there is a partial softening in the high strain amplitude, e.g., $\varepsilon_a = 1.6\%$ compared to 1 %, which causes nonlinearity in the elastic strain response of the material, when plotted with respect to the number of reversals (Figure 3-21). As a consequence, the fatigue modeling of ZK60 can be complex. A goal in fatigue modeling of anisotropic materials is to discover a set of universal parameters that can be employed for life prediction of the material regardless of the orientations. To this intent, RD was selected as the primary direction, and the universal parameters required for two different damage criteria were extracted from the experiments in this specific direction. Eventually, these parameters were used to predict the life in other directions. In what follows, SWT, as a critical plane model, and JV, as an energy-based damage criterion, are assessed for the fatigue life prediction of ZK60.

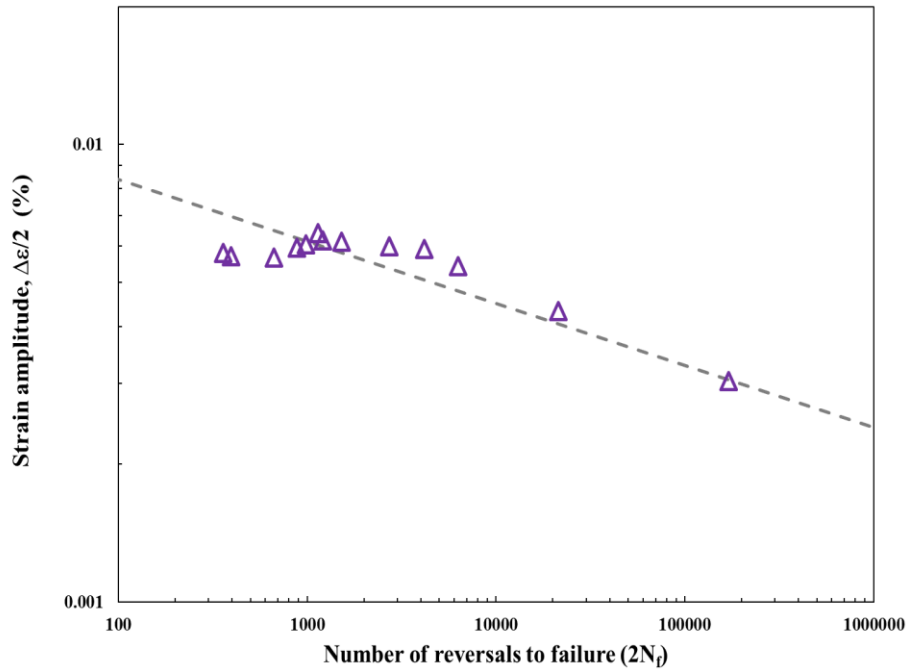


Figure 3-21. Nonlinear elastic response of the strain for ED

3.5.1 SWT

By employing strain-life and hysteresis curves along RD, the elastic and plastic strain ranges with respect to the number of reversals to failure are depicted in Figure 3-22. The Coffin-Manson

parameters, as presented in Table 3-2, were extracted from the experimental results in the reference direction (RD) using the aforementioned equations. Finally, by substituting these parameters into the SWT model (Eq. 2-1 and Eq. 2-2), the predicted lives in all three directions were found through a numerical solution.

Table 3-2. Coffin-Manson parameters for SWT model

σ'_f (MPa)	360.73
ϵ'_f	1.862
b	-0.110
c	-0.780

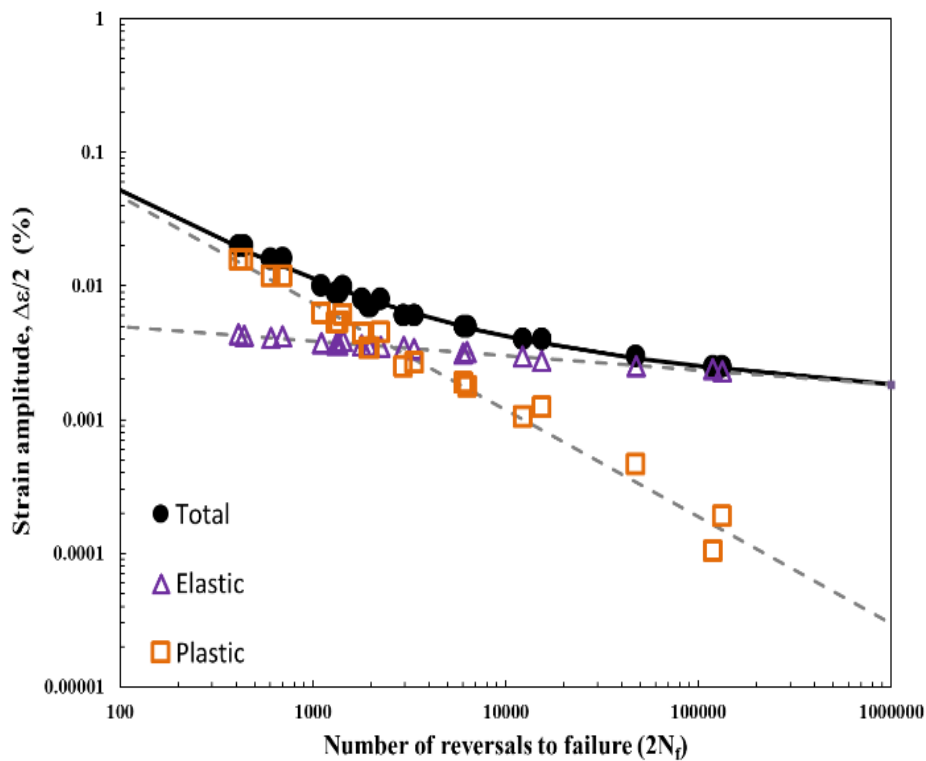


Figure 3-22. Decomposition of strain into elastic and plastic strain in RD

The predicted lives in contrast to the experimental ones are illustrated in Figure 3-23. A diagonal solid line denotes the ideal prediction, while the dashed and dashed-dot lines specify the area where predicted life over experimental life rests within the factors of 2 and 2.5, respectively. Along RD, life prediction meets expectation in accordance with the fact that the Coffin-Manson parameters were extracted in this direction. For both 45° and ED specimens, SWT underpredicts

the life; however, the prediction is more conservative for ED. The observed drop in the life prediction accuracy of ED might be attributed to the observed nonlinear elastic strain of the material, which is fitted by the linear regression in the Coffin-Manson relation (Figure 3-21).

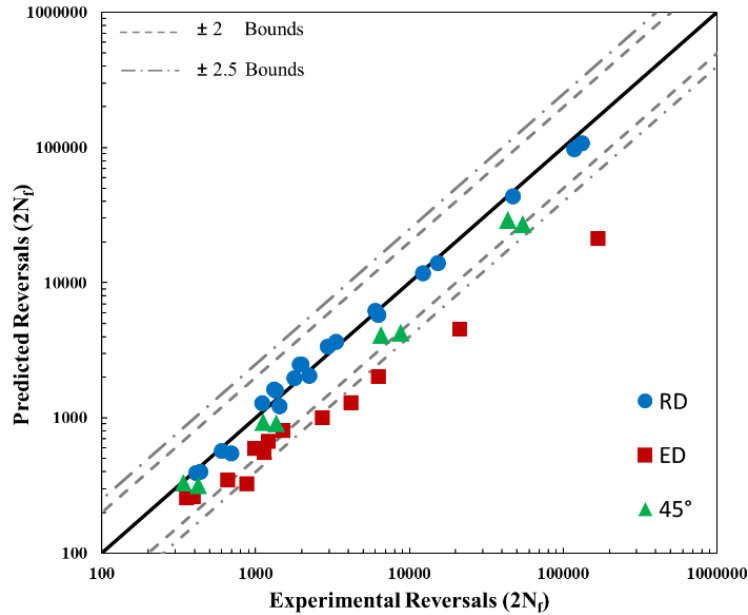


Figure 3-23. SWT predicted vs. experimental reversals for all directions

3.5.2 Jahed-Varvani

Based on the introduced concepts in section 2.1.2.2, the JV parameters are determined from the curves fitted to the elastic and plastic portions of the energy along RD, as depicted in Figure 3-24. By employing the JV model in conjunction with the parameters extracted for RD, Table 3-3, fatigue lives in different directions are predicted numerically similar to the SWT approach and plotted against the experimental life in Figure 3-25.

Table 3-3. JV model parameters

E'_e (MJ/m ³)	1.4875
E'_f (MJ/m ³)	1604.3
B	-0.219
C	-0.920

The data-points congregating about the solid line and almost within the bound of factor 2.5 in both LCF and HCF regions demonstrate the capability of the JV parameter to model the fatigue of ZK60 with anisotropic behavior. However, some deviation is observed along the ED direction as

the lives increases to more than 10000 cycles. This deviation is possibly attributed to exhausted plastic energy decapitation through the hysteresis loops in HCF where the model relies solely on the elastic part of the strain energy. Comparing the Figure 3-23 and Figure 3-25 suggests that the SWT model yields to more conservative life predictions than the JV model.

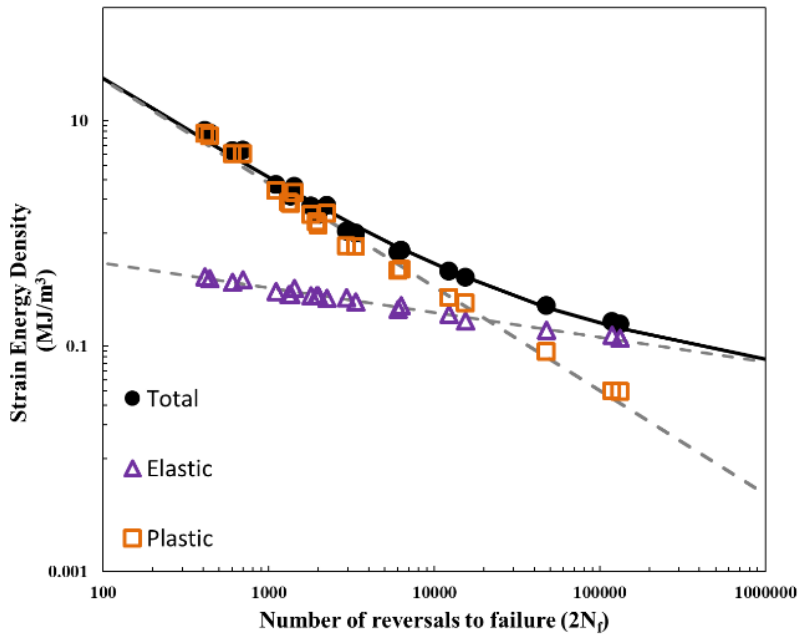


Figure 3-24. Decomposition of total strain energy into elastic and plastic energies in RD

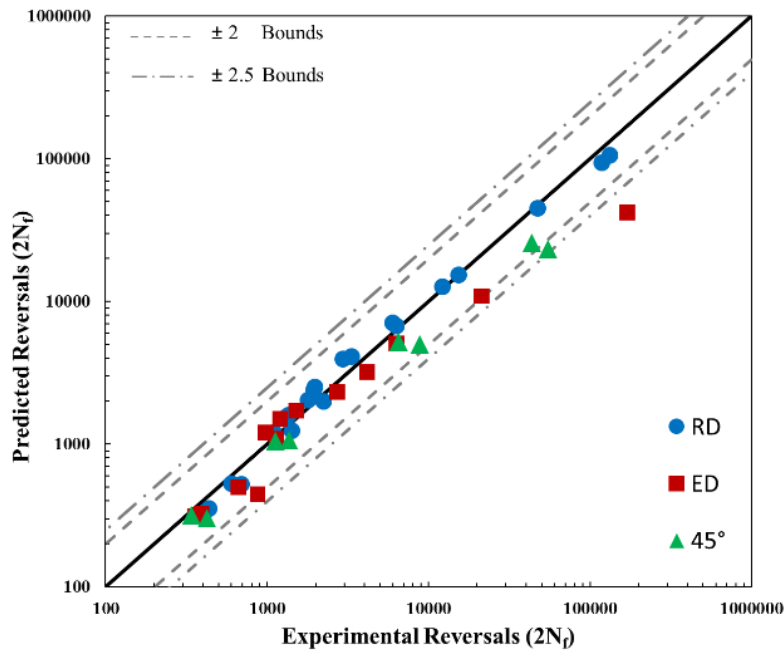


Figure 3-25. Predicted vs. experimental reversals for all directions by JV model

3.6 Further Discussion

The total strain energy density, as a fatigue damage parameter, is determined at each strain amplitude at the stabilized cycle to discern the underlying reason for similar LCF lives, but different HCF ones. Figure 3-26 depicts the total strain energy density against the total strain amplitude for the different directions. It is observed that at high strain amplitudes, although the deformation behaviors are dissimilar, the fatigue damage parameters are roughly the same.

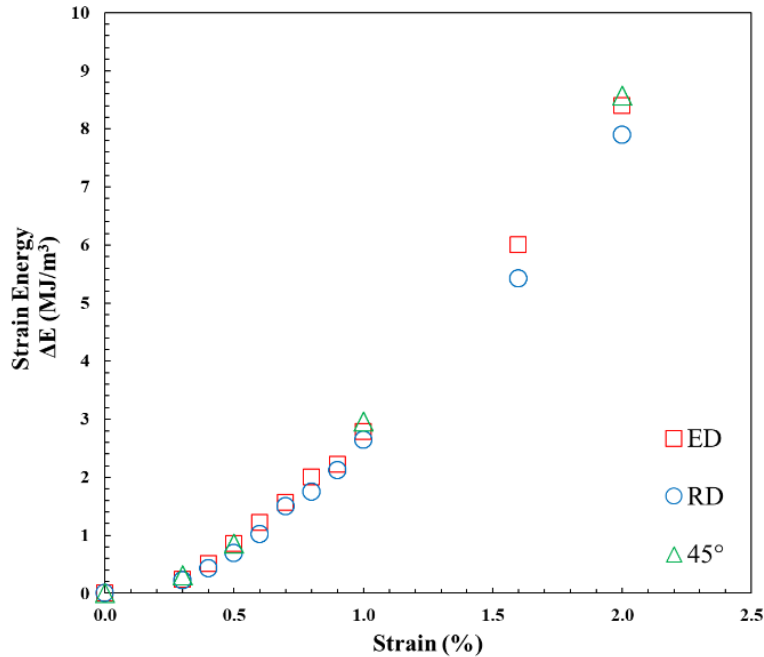


Figure 3-26. Total strain energy density as the fatigue damage parameter at different strain amplitudes along different directions for ZK60 extrusion

Therefore, the fatigue lives in the LCF regime are identical in the wake of similar fatigue damage occurring. On the other hand, under small strain amplitudes, i.e., the HCF regime, the amount of damage at the stabilized cycle is marginal and close to zero, implying elastic deformation.

3.7 Summary

The quasi-static and strain-controlled fatigue characteristics of ZK60 extrusion has been investigated along three different directions: the extrusion direction (ED), the radial direction (RD), and 45° to extrusion direction (45°). The quasi-static response showed symmetric behavior for the samples tested along RD and 45°, whereas ED samples manifested completely asymmetric

behavior. While the ED samples exhibited longer fatigue lives than the RD and 45° in the high cycle fatigue, the fatigue lives in the low cycle fatigue regime were similar. Microstructural analysis revealed finer grains for ED, thereby higher strength for this direction. Moreover, the texture measurement indicated a sharp basal texture justifying asymmetric behavior, solely along ED direction. Higher tensile mean stress and less dissipated plastic energy per cycle for the ED samples, acting as two competing factors, were the principal reasons for their identical fatigue response to those of RD and 45° in the LCF regime. The fracture surface in the ED direction was dominated by twin lamellae and profuse twined grains, whereas slip bands were dominant on the fracture surface in RD direction. Finally, Smith-Watson-Topper, as a critical-plane strain-based, and Jahed-Varvani, as an energy-based, damage criteria were employed to predict the fatigue lives along all directions using a single set of material parameters.

Chapter 4

Cyclic Stress-control Behavior

This chapter characterizes the fatigue behavior of ZK60 extrusion under stress-controlled condition in two perpendicular directions: extrusion direction (ED) and radial direction (RD). Special attention is given to the detailed explanation of the observed anisotropy and asymmetry. The JV model is calibrated using the strain-controlled experiments presented in Chapter 3. The merit of the JV model is then scrutinized by using the same set of material parameters to predict the fatigue life for stress-controlled experiments. The results demonstrate promising correlations between the experimental and predicted fatigue lives in different material orientations for both the stress- and strain-controlled loading conditions.

4.1 Material and Specimens

An extruded cylindrical billet with a diameter of 127 mm made of commercial ZK60 and supplied by Magnesium Elektron of North America (MENA) was used in the current study. The raw material is identical to the one previously investigated in Chapter 3. The dog-bone specimens, with the geometry depicted in Figure 4-1 (a) were machined along RD and ED according to the cylindrical coordinate system, as illustrated in Figure 4-1 (b).

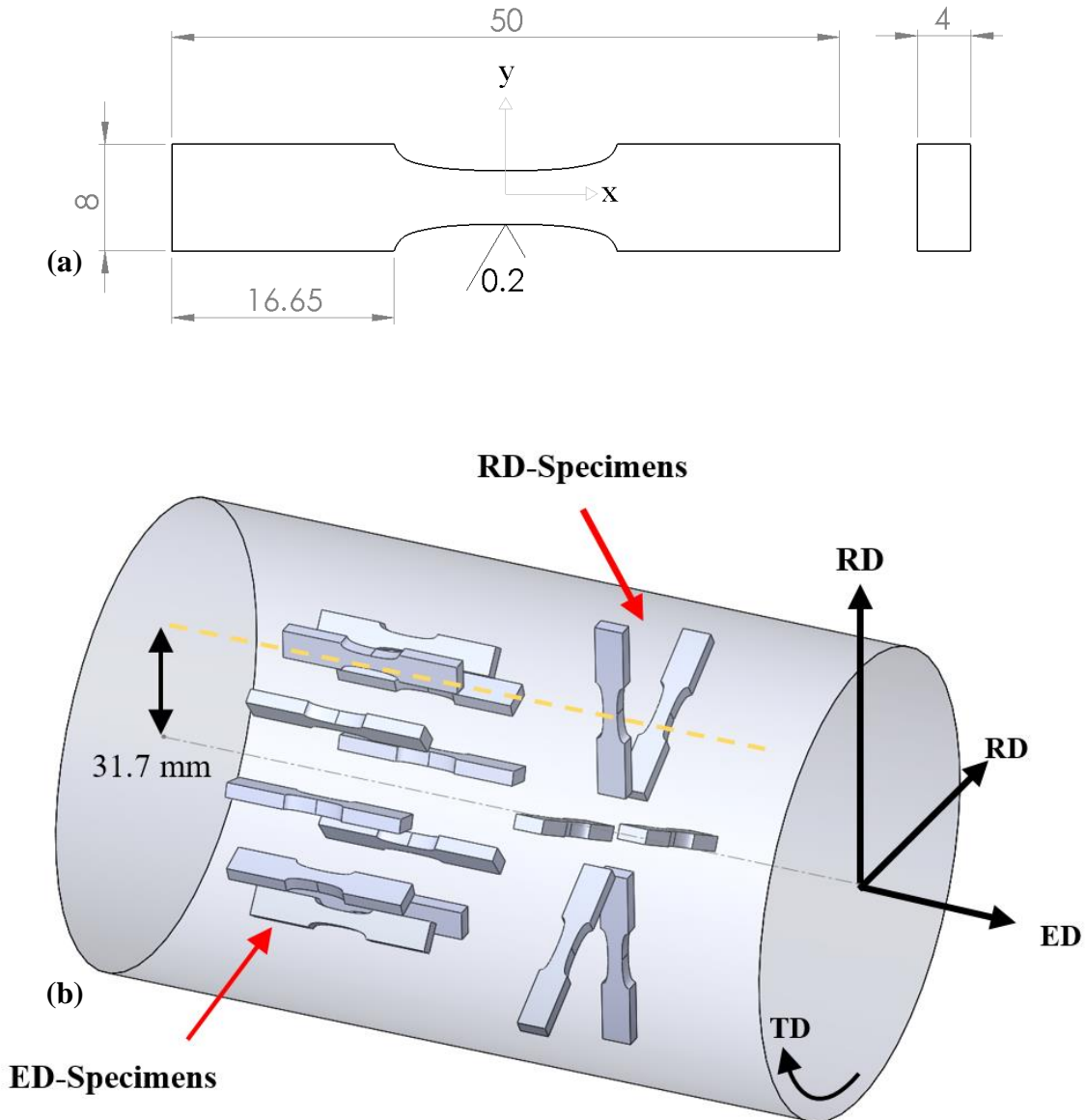


Figure 4-1. a) Dog-bone specimens' geometry; b) Specimens' orientations machined from ZK60 extrusion billet

4.2 Experimental Procedures

All tests were conducted at the room temperature, using a servo-hydraulic Instron 8872 test frame. Fully reversed ($R=-1$) stress amplitudes were generally imposed in the range of 70 to 200 MPa at a cyclic frequency of 10 Hz. In general, the loading cycle was initiated by a tensile reversal and followed a sinusoidal waveform. Strain was measured throughout the tests using an Instron extensometer with a gauge length of 10 mm and a ± 1 mm travel. For each stress amplitude, at least two specimens were tested to ensure reproducibility of the test results, and N_f denotes the number of cycles corresponding to final fracture. Tests were interrupted after 10^6 cycles, and the life was considered infinite.

4.3 Results and Discussion

Texture analyses in Chapter 3 demonstrated that the extrusion process on ZK60 renders the c -axes perpendicular to the ED but randomly distributes them in the RD-TD plane. The large difference in tensile and compression yield strengths of specimens loaded along ED revealed intense asymmetry, which is attributed to easily activated extension twins along ED under compression. In contrast, the undirected dispersion of the HCP crystals in the RD-TD plane provides an equal chance of extension twinning in both tension and compression for RD specimens, resulting in almost symmetrical behavior.

4.3.1 Fatigue Behavior

4.3.1.1 Radial Direction

Figure 4-2 illustrates the evolution of engineering strain in the first loading cycle for an RD specimen loaded to the stress amplitude of $\sigma_a = 200$ MPa. In the first tensile reversal, beyond the tensile yield strength (TYS), basal slip dominates the plastic deformation at low stress levels. However, due to the undirected crystallographic orientation in the loading plane (RD-TD), $\{10\bar{1}2\}$ pyramidal twinning may be triggered at high stress levels. The first tensile reversal plastically deforms the specimen up to 4% of strain by simultaneous activation of slip and extension-twinning, with slip being the dominant mechanism, contributing to low YYS. The crystals with their c -axis oriented in RD will undergo tension twinning during the first reversal and will rotate by 86.3° toward TD [94]. Dislocation slip governs plastic deformation in other grains where the crystals

were initially oriented unfavorably for twinning. The newly twinned grains unite the primary untwinned grains and form a basal texture, with most basal planes being aligned parallel to the TD. Now, these grains are ready to be twinned under subsequent unloading/compressive reversal. In the subsequent reversal, detwinning of formerly twinned grains in conjunction with the twinning of untwinned grains, predominantly strain the specimen up to 0.5% at which value detwinning will be almost exhausted. Further compressive loading results in non-basal slip activation and forms a mild sigmoidal shape of the unloading curve. At the end of the unloading stroke, 1.7% compressive strain will be imposed which is lower compared to 4% tensile strain achieved at the end of loading. The asymmetric straining can be attributed to the slightly higher compressive yield strength (CYS) against TYS, and activation of harder non-basal slip in compression. Thus, when the specimen is reloaded in tension, it will be deformed by means of the detwinning followed by non-basal slips up to 3.5 %, instead of the prior 4 % strain imposed by the initial loading. This difference generates a 0.5% strain gap within the unclosed hysteresis loop, in the form of the mean strain as indicated in Figure 4-2. This directional and escalating mean strain is referred to as “cyclic strain ratcheting” [30].

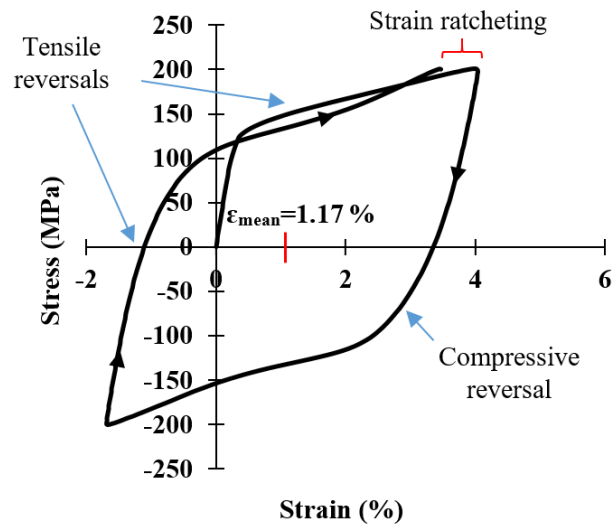


Figure 4-2. Strain ratcheting in the first cycle along RD at $\sigma_a = 200$ MPa

In metals with symmetric tension–compression curves, ratcheting takes place by virtue of mean stress [30], whereas in wrought Mg alloys fully reversed loading with no mean stress will induce a substantial amount of ratcheting due to asymmetric cyclic hardening behavior. The mutual participation of twinning and slip in both tensile and compressive reversals yields the sigmoidal but near-symmetric shape of the hysteresis loop for the first cycle along RD.

Figure 4-3 shows the progressive strain ratcheting through engineering stress-engineering strain fatigue hysteresis loops. The near-symmetric shape of the first cycle's stress-strain response is sustained during cyclic loading; however, the size of the hysteresis loop shrinks significantly. The translation of the maximum and minimum strain in opposite directions, as depicted in Figure 4-4, governs the observed reduction in the size of the hysteresis loops. It is interesting to note that the maximum strain development is almost saturated after the first cycle; however, the minimum strain continues to decline (Figure 4-4). This contrasting behavior can be attributed to deficient detwinning and residual twins impeding the plastic deformation during tensile reversals [42].

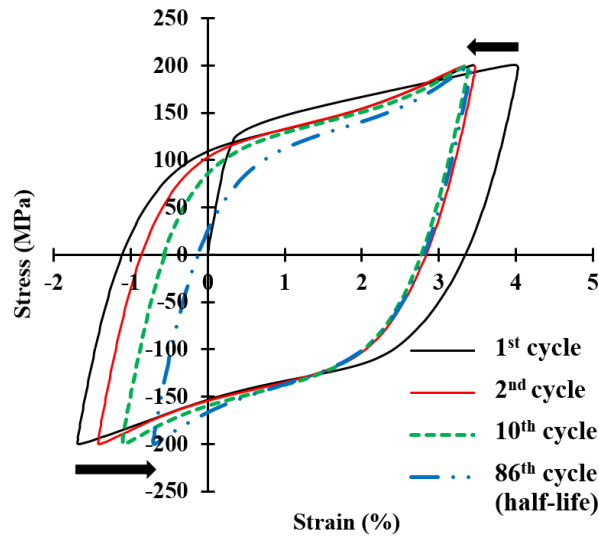


Figure 4-3. Evolution of stress-strain hysteresis loops along RD at $\sigma_a = 200$ MPa

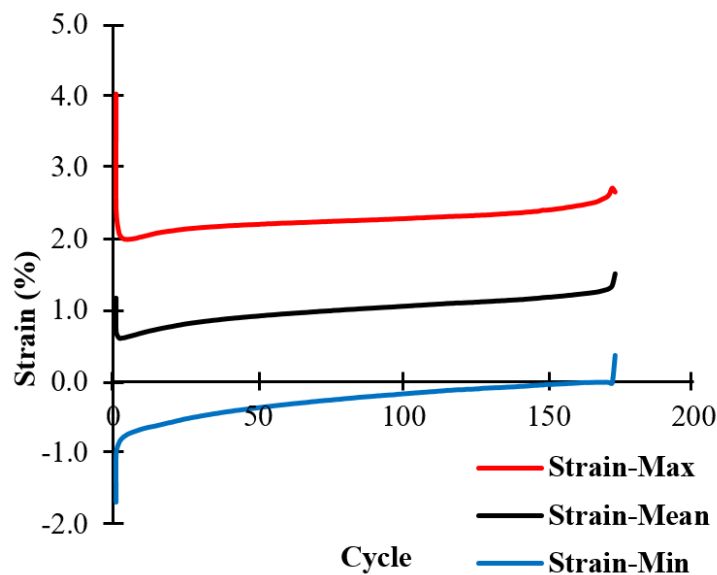


Figure 4-4. Strain evolution along RD at $\sigma_a = 200$ MPa

The analogous characteristics were perceived for lower stress amplitudes, e.g. $\sigma_a = 140$ MPa, by comparing the first and half-life hysteresis loops of the RD specimens illustrated in Figure 4-5 (a) and (b), respectively. The only dissimilarity is the concave shape of the hysteresis loops at low stress amplitudes, which can be ascribed to the disabled twinning-detwinning due to insufficient stress.

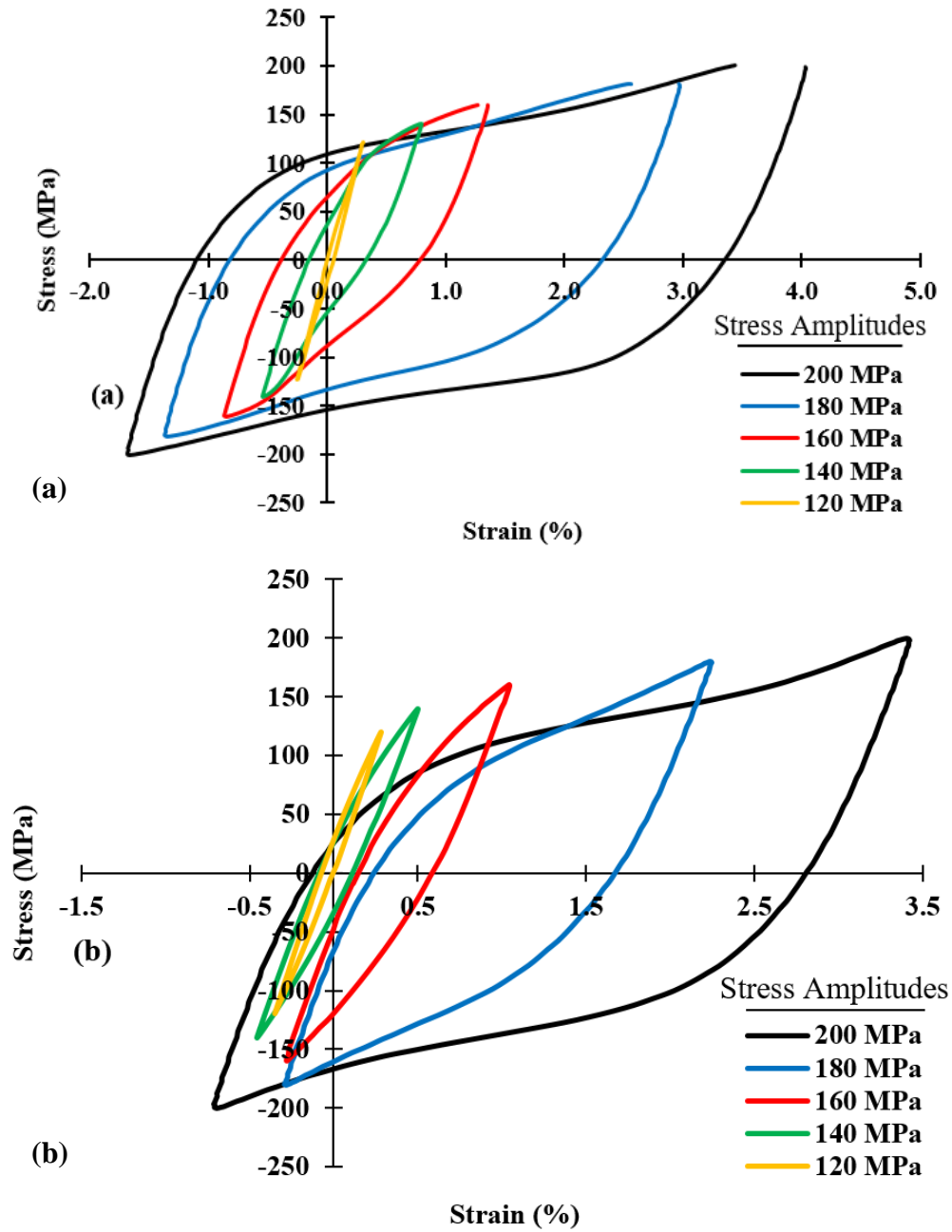


Figure 4-5. Stress-strain hysteresis loops along RD at different stress amplitudes, ranging from $\sigma_a = 120$ to 200 MPa: (a) for the 1st cycle, and (b) for the half-life cycle

4.3.1.2 Extrusion Direction

Figure 4-6 shows the engineering stress-engineering strain hysteresis response in the first loading cycle along ED for $\sigma_a = 200$ MPa. The high TYS in ED, i.e., 238 MPa, compared to 200 MPa maximum stress places the first reversal in the elastic region. By reversing the load, the basal texture favors extension twinning activation, resulting in 86.3° rotation of the crystallographic lattice with respect to the loading direction [53]. Twinning in compression reduces CYS against TYS [62], typically referred to as asymmetry, and brings about a significant amount of strain (-4.5 %) at the end of the unloading reversal. The twinned lattices are favorably aligned to detwin during the subsequent tensile loading. Detwinning reorients the twinned grains; however, complete texture restoration is unattainable, and residual twins develop [42]. Detwinning exhausts before reaching the maximum tension where harder non-basal slip takes over and accommodates deformation at yet a higher strain-hardening rate [6][95]. This substitution turns the concave-down loading curve into a sigmoidal one due to the higher stress demands of non-basal slip mechanisms. The discussed asymmetric behavior of the material leaves a gap in the hysteresis loop, as illustrated in Figure 4-6, and results in accumulating ratcheting strain.

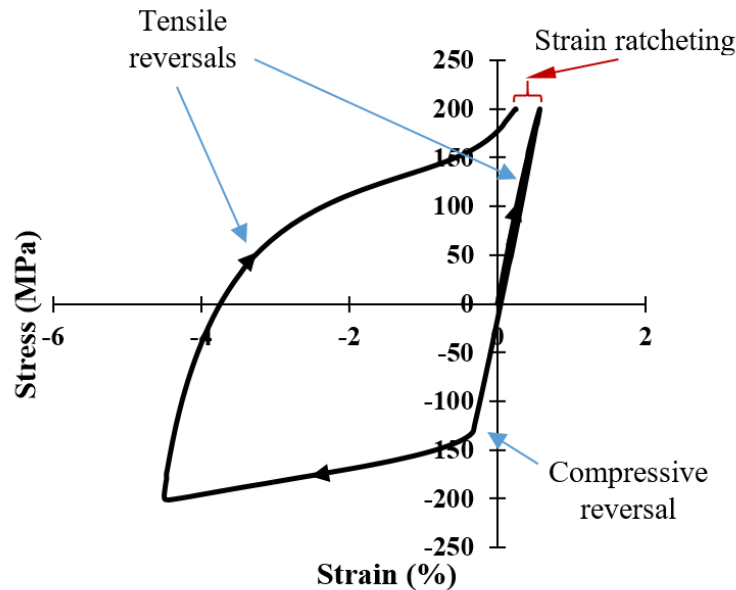


Figure 4-6. Strain ratcheting in the first cycle along ED at $\sigma_a = 200$ MPa

Figure 4-7 depicts the cyclic ratcheting of an ED specimen subjected to $\sigma_a = 200$ MPa. The smooth transition from an asymmetric hysteresis response in the first cycle to a fully symmetric

hysteresis in the half-life cycle (cycle #475) can be perceived. This characteristic suggests that twinning and detwinning are the dominant deformation mechanisms in the first few cycles, but are replaced by dislocation slip in subsequent cycles. The continuous but decaying evolution of maximum and minimum strains in ED, as shown in Figure 4-8, shrinks the hysteresis loops, analogous to the behavior observed in RD. Significant irreversible deformation in the first few cycles along with residual twins development that obstruct later plastic deformation prevent the twinning-detwinning from governing plastic deformation with increasing loading cycles and induce a pronounced material hardening, reflected in the strain range reduction [62].

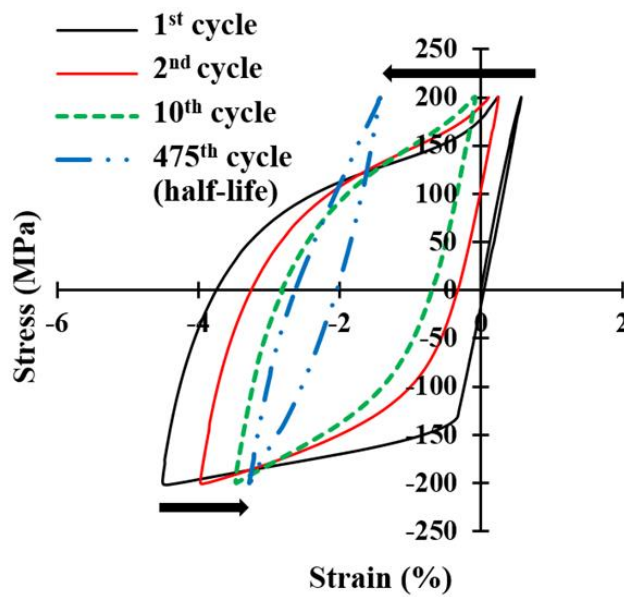


Figure 4-7. Evolution of stress-strain hysteresis loops along ED at $\sigma_a = 200$ MPa

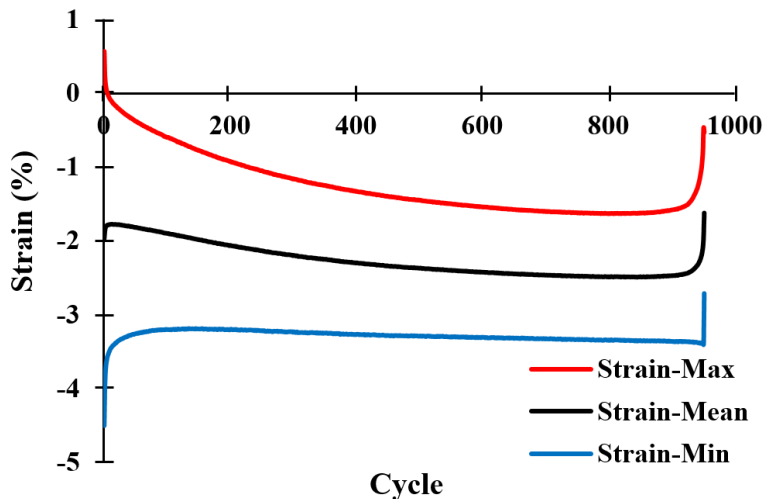


Figure 4-8. Strain evolution along ED at $\sigma_a = 200$ MPa

Figure 4-9 illustrates the hysteresis loops corresponding to the first and half-life cycles in different stress amplitudes. By comparing Figure 4-9 (a) and (b) and tracking the alternation of stress-strain responses at each stress amplitude, a transition from asymmetric to symmetric hysteresis is notable for $\sigma_a > 150$ MPa. However, at lower stress levels, the twinning-detwinning cannot be triggered even in the initial cycles, which puts the slip in charge for the entire history of plastic deformation.

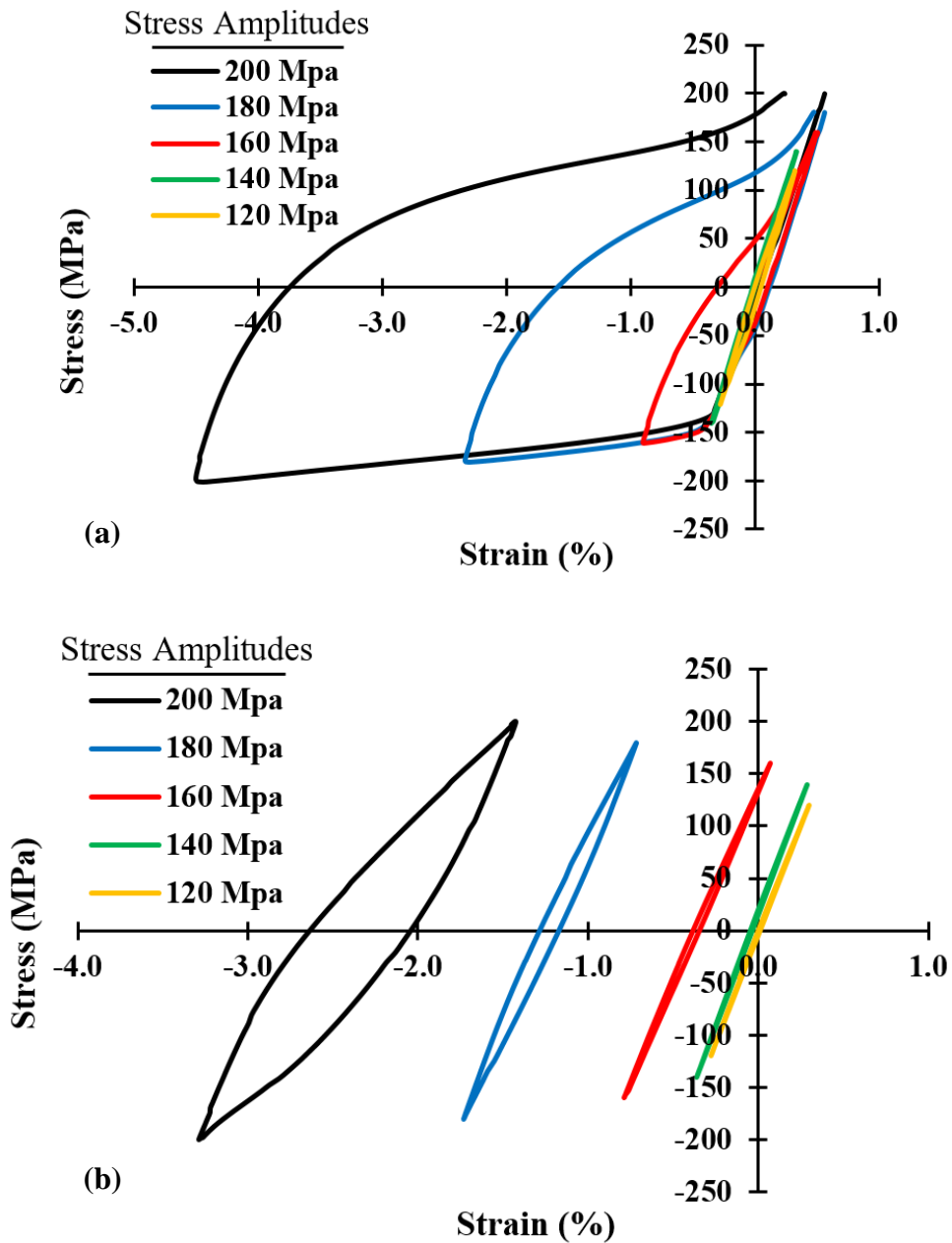


Figure 4-9. Stress-strain hysteresis loops along ED at different stress amplitudes, ranging from $\sigma_a = 120$ to 200 MPa: (a) for the 1st cycle, and (b) for the half-life cycle

4.3.2 Stress-life Curve

Figure 4-10 displays the stress-life curve for ZK60 extrusion along ED and RD. Data-points with arrows indicate run-out tests at 10^6 cycles. The selection of 10^6 cycles for infinite life is corroborated by the literature, which reports the minimal slopes of stress- and strain-life curves for Mg alloys in the range of $10^6 < N_f < 10^8$ cycles [37,101]. The anisotropic quasi-static behavior of ZK60 extrusion is extended to its cyclic stress-controlled behavior as well. The material along ED exhibits superior fatigue performance compared to RD at all stress levels. This behavior contrasts with observed identical LCF strain-controlled behavior in ED and RD (Figure 3-12). As exemplified in Figure 4-11, ED specimens show smaller hysteresis loops and consequently less plastic-induced damage at the same load level compared to RD, which can justify the ED specimens' longer survival. The gap perceived in the number of cycles to failure for the two loading directions is sustained through all stress levels.

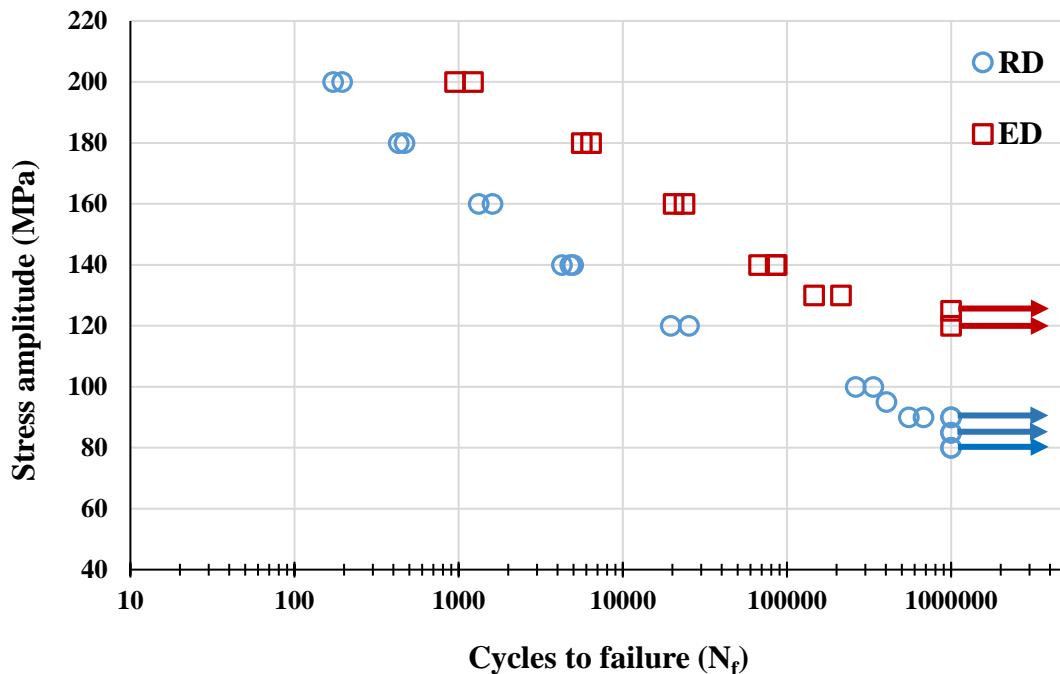


Figure 4-10. Stress-life curves for RD and ED

Fatigue strength in each direction was quantified by sequentially testing a set of specimens in accordance with the staircase statistical analysis method described in section 2.1.3. The fatigue strength at 10^6 cycles was found equal to 87 MPa and 120 MPa for RD and ED specimens, respectively.

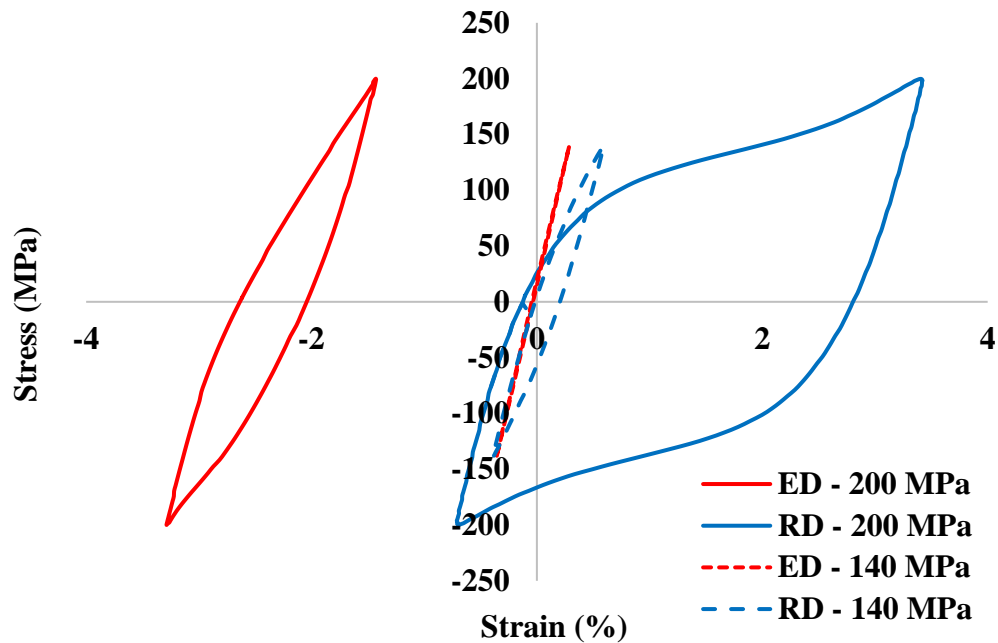


Figure 4-11. Smaller hysteresis loops of ED compared to RD at two stress amplitudes

4.3.3 Ratcheting Strain Effects on Fatigue Life

The Effect of mean stress on the fatigue strength of Mg alloys has been a major area of interest for researchers [81,102–106]. However, the literature suggests that fatigue strength is insensitive to mean strain if no mean stress is involved [37,72]. In order to evaluate this argument for ZK60 extrusion and also to examine the loading sequence effect, cyclic loading was applied with $\sigma_a = 200$ MPa along both RD and ED, with the first reversal being compressive, unlike in the previous experiments, where the first reversal was tensile. When the RD specimens are initially loaded in compression, a negative mean strain compared to the positive one in the tension-first experiments (Figure 4-12), is induced. The inceptive compressive strain is compensated for by positive strain ratcheting in the subsequent cycles, even though, the half-life mean strain ends up smaller than that with tension-first loading. Therefore, as depicted in Figure 4-13, the dissimilar loading sequence results in a mismatched half-life mean strain for RD; however, the cycles to failure remain close due to the analogous hysteresis-loop shapes. In contrast to RD, the half-life hysteresis along ED for both the loading sequences are almost identical. The similarity can be described by the fully elastic behavior along ED in the first tensile reversal, i.e., the first reversal induced almost no residual strain at zero stress point of the unloading/compressive reversal (Figure 4-6).

Therefore, the material experiences the same plastic deformation history for the two loading sequences, resulting in an identical half-life response.

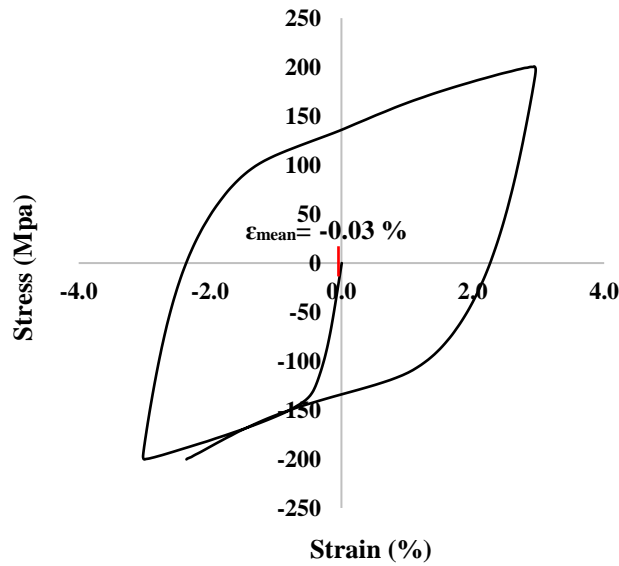


Figure 4-12. Initial compressive mean strain for the RD compression first test at $\sigma_a = 200$ MPa

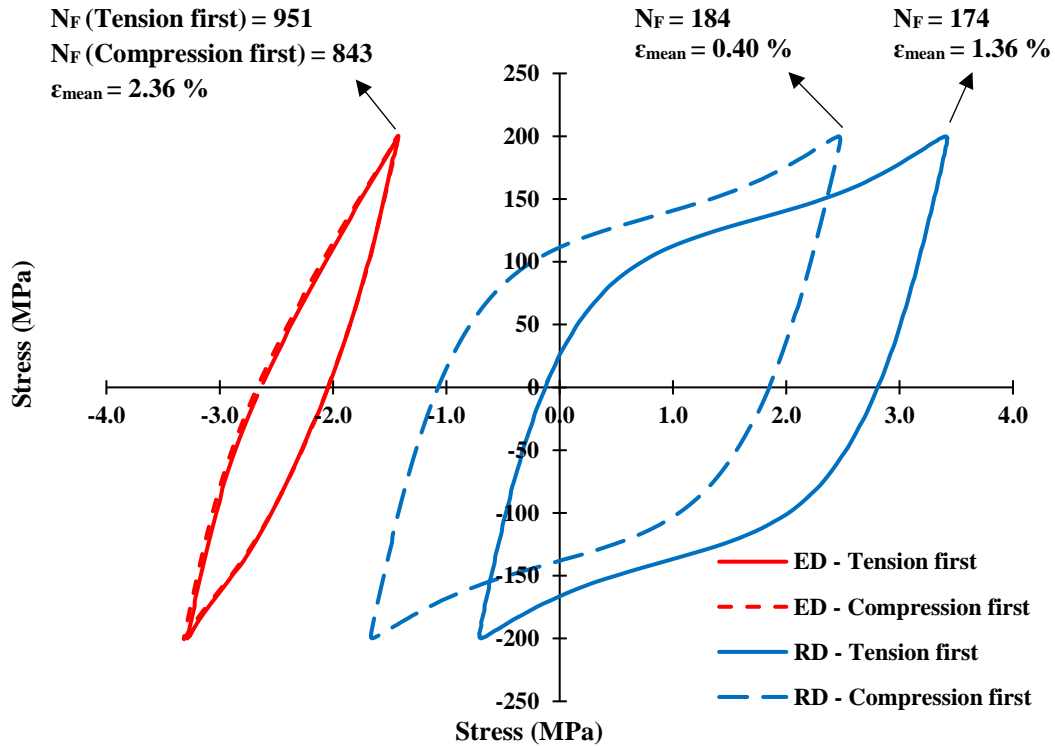


Figure 4-13. Effect of loading sequence on half-life hysteresis loops for ZK60 extrusion under $\sigma_a = 200$ MPa

4.4 Fatigue Modeling

4.4.1 Stress-Based Model (Basquin)

In order to mathematically express the stress-life curves along two directions via a stress-based model, the classical Basquin equation was employed [30]:

$$\sigma_a = A(N_f)^B \quad \text{Eq. 4-1}$$

where σ_a is the imposed stress amplitude, and A and B are material constants indicated in Figure 4-14. By implementing the material's constant from RD, lives predicted and plotted against experimented ones (Figure 4-15). Based on the dissimilarity observed for A and particularly B values along the different directions, one can expect that using one set of material parameters for the life prediction in different material orientations will be impractical in Basquin's model. To that intent, the adaptation of supplementary data, e.g., hysteresis loops, is indispensable, as discussed hereinafter.

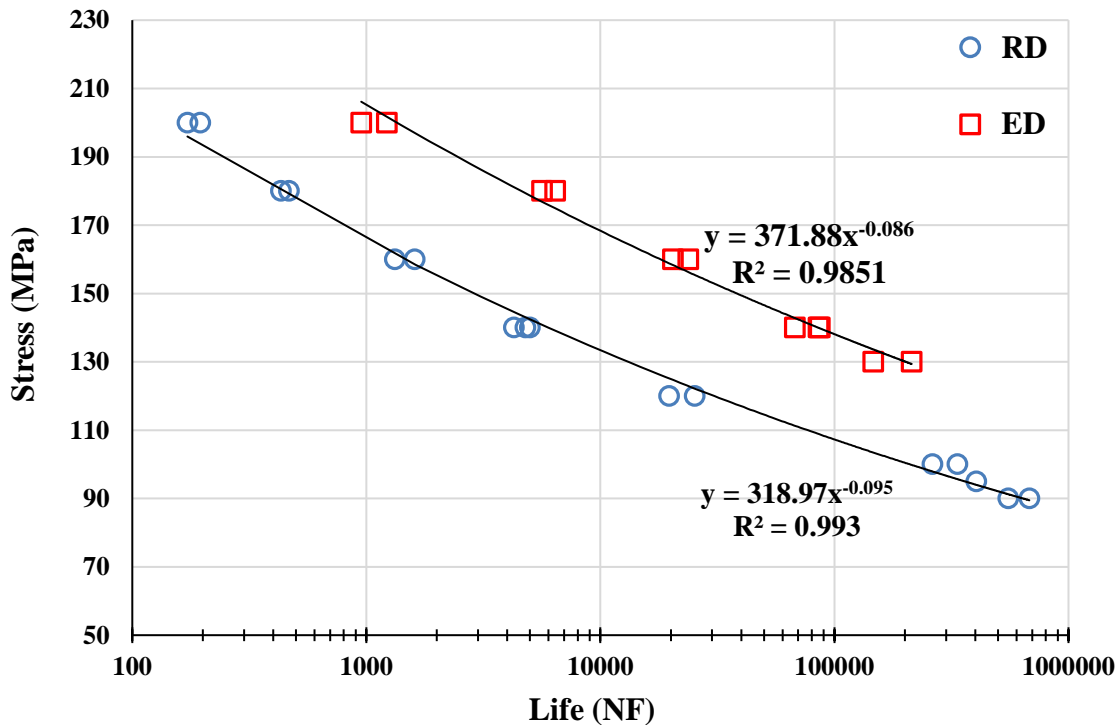


Figure 4-14. Basquin equation fitted to the stress-life curves of RD and ED

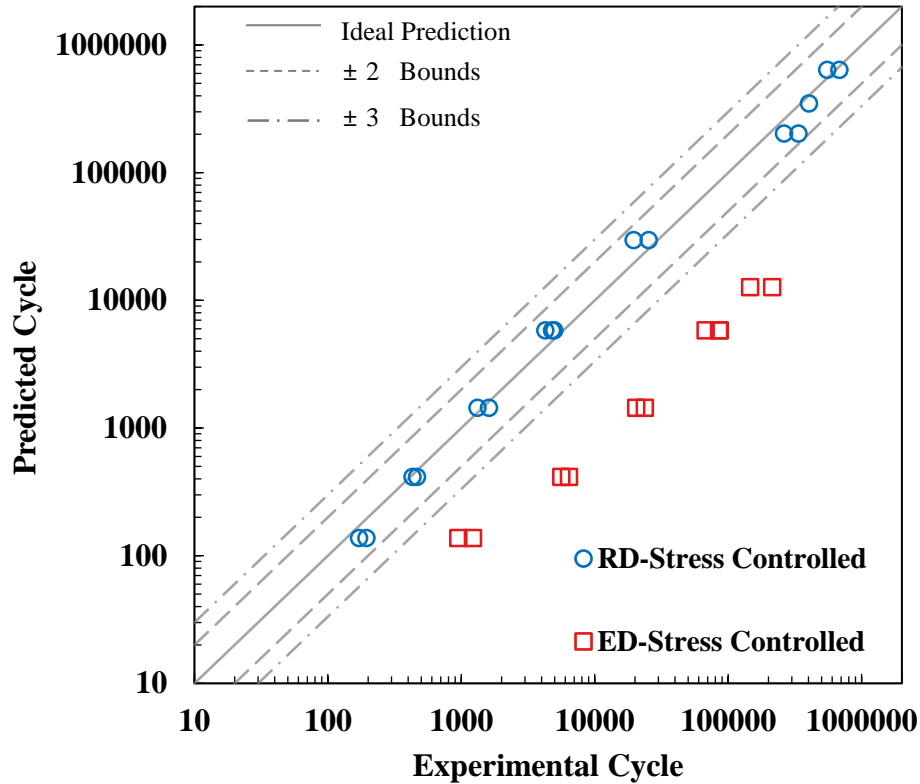


Figure 4-15. Predicted vs. experimental life for different directions using Basquin equation

4.4.2 Energy-Based Model (JV)

In order to predict the life via JV model, the experimental energy density values are extracted from the half-life hysteresis of strain-control tests along the reference direction (RD), as discussed in section 3.5.2. The strain-control half-life hysteresis loops were presented earlier in Chapter 3. The gradual evolution of the material's strain response in cyclic strain-control tests makes their half-life a suitable reference cycle for the fatigue modeling. The JV coefficients are listed in Table 3-3. In order to substantiate JV as an anisotropic fatigue model, these coefficients are employed to predict the stress-controlled fatigue life of the material along both RD and ED. The energy values for the stress-controlled tests were calculated using the half-life stress-strain response of the material in the two directions, Figure 4-5 (b) and Figure 4-9 (b). By utilizing TSED as an energy-based damage parameter, three sets of data are consolidated into one curve regardless of loading direction (Figure 4-16). Comparing this single energy curve with two isolated stress-life curves fitted by Basquin equation (Figure 4-14), indicates the energy-based model's superiority for anisotropic fatigue modeling of wrought Mg alloys over stress-based one.

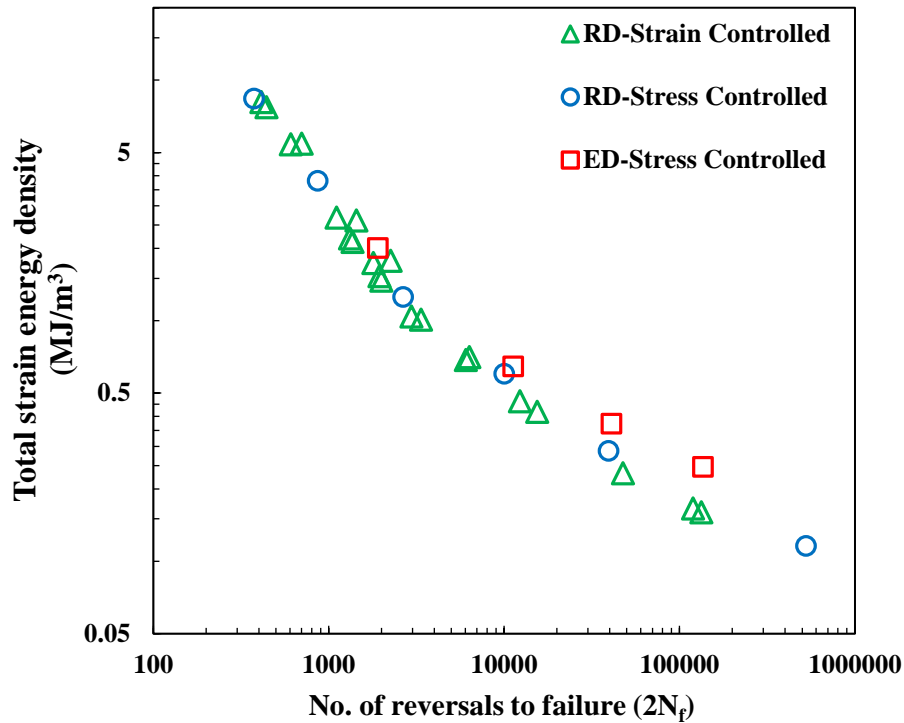


Figure 4-16. Comparing TSED as a function of reversals for different loading conditions

Figure 4-17 presents the life predicted by the JV model with respect to the experimental life for the reference data set (i.e., strain-controlled results along RD) used for the model calibration. All the strain-controlled data points congregate tightly about the ideal estimation, which is expected as the model's coefficients were extracted from the same data set. This graph also includes the predicted and experimental results for stress-controlled tests along RD and ED. The JV model provides a better correlation for RD compared to ED, a finding attributed to the fact that the JV coefficients correspond to RD direction. The life prediction for RD was excellent in the LCF, where the plastic deformation is significant and the PSED is the dominant term in the damage calculation (Eq. 2-5). However, in the HCF regime, where the PSED diminishes and the ESED takes over the fatigue damage, the life predictions deviate from the experimental life toward conservative predictions. The predictions along ED are not as accurate as those for RD, especially in HCF, where the lives are under-predicted. The deficiency can be attributed to ESED, as the controlling parameter in HCF regime. ESED over-predicts damage with its current definition where PSED is minor due to the compact hysteresis loops.

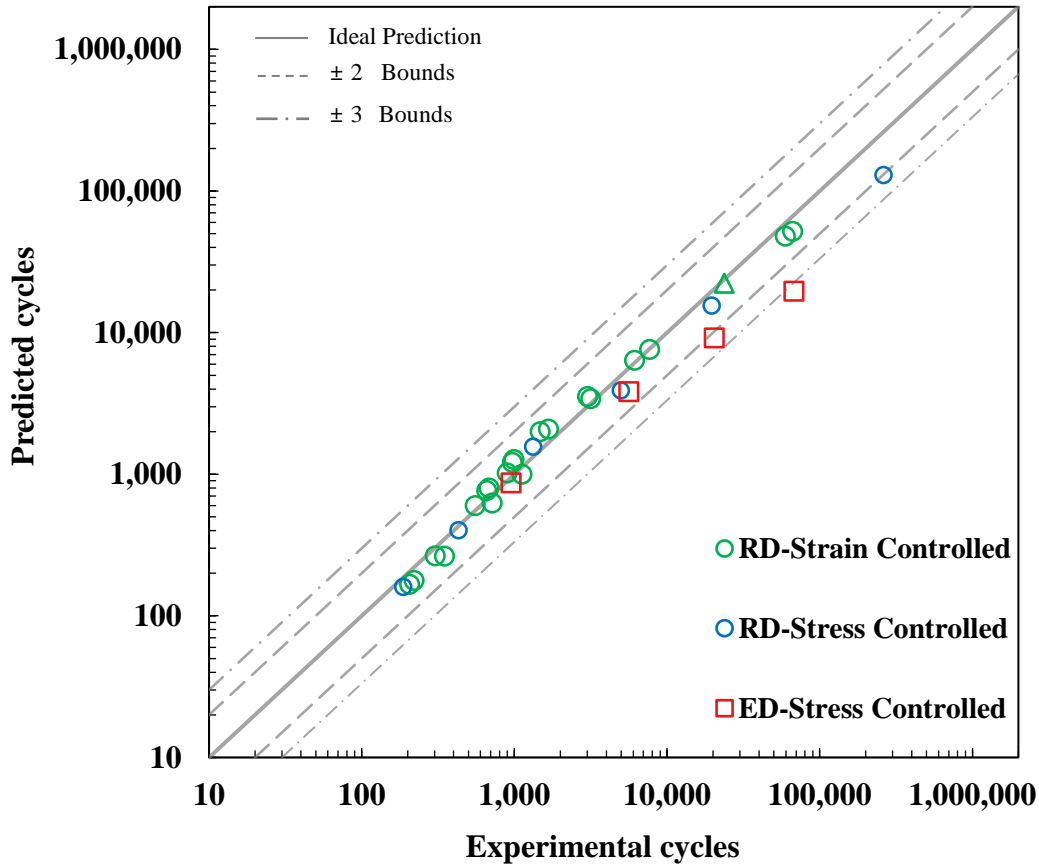


Figure 4-17. Predicted life vs. experimental life for both directions using one set of JV coefficients

In order to evaluate the prediction accuracy, the mean squared errors (MSE) between the n experimental and predicted lives at logarithmic scale were calculated, as follows:

$$MSE = \frac{\sum_{i=1}^n [Log(N_{Experimental}) - Log(N_{Predicted})]^2}{n} \quad \text{Eq. 4-2}$$

The MSE for the different sets of fatigue data is displayed and compared in Figure 4-18. As shown in this figure, because the JV coefficients were extracted from RD, the predicted lives in RD are more accurate than those in ED. The accuracy reduction along ED is expectedly immense when Basquin equation is employed.

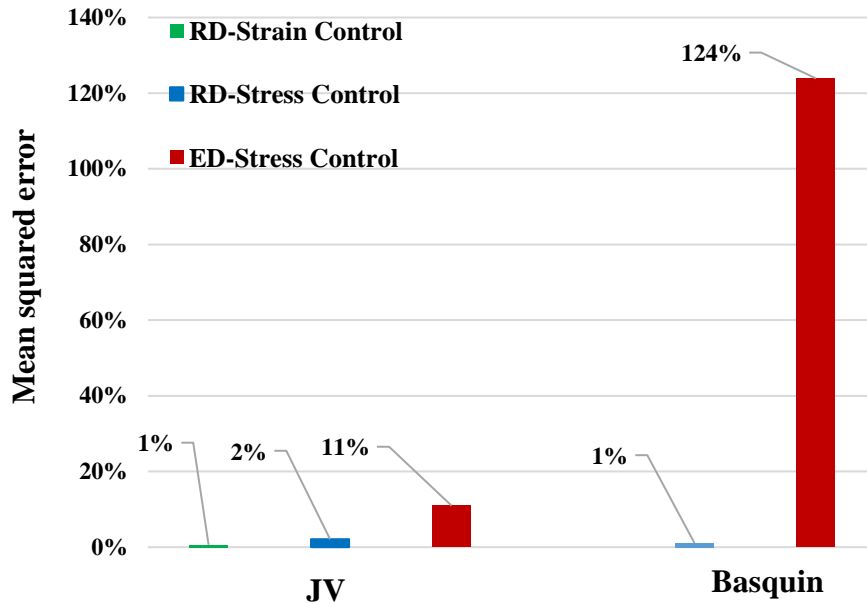


Figure 4-18. Mean squared error for strain- and stress-controlled tests, representing the prediction accuracy of JV and Basquin models

4.5 Further Discussion

4.5.1 Reference Cycle in Fatigue Modeling

Because damage is a cumulative phenomenon, averaging it can appropriately represent the damage, a material has sustained in its lifetime. However, in order to ease the calculation process, the majority of fatigue models assume that the material response is stabilized by the half-life cycle and calculate the damage parameter for this cycle [30]. Since the half-life cycle represents the material behavior over the majority of the fatigue life in these models, the damage associated to the half-life cycle is then extended to every cycle of the fatigue experiment under constant amplitude loading. In particular, these assumptions are often employed in modeling strain-controlled experiments [30]. Nevertheless, one should note that these assumptions may be violated in some cases; for instance, the material response in the strain-controlled tests does not stabilize when subjected to very high strain amplitudes [107]. Furthermore, the damage distribution over a life-time could enforce a noteworthy difference between average and half-life damages, making the half-life an inaccurate reference for the fatigue analysis. In particular, in stress-controlled tests, substantial evolution occurs in the strain response over the first few cycles. Thus, the total strain energy density also changes significantly before the material response stabilizes. Figure 4-7 reveals

that in the first cycles, considerable damage takes place. The damage rapidly diminishes through shrinkage of hysteresis loops. Therefore, the material is exposed to significant damage before it reaches the half-life cycle. This phenomenon can call into question the applicability of the half-life cycle as the reference cycle for damage calculation in stress-controlled tests.

In order to assess the validity of the half-life concept in stress-controlled tests, the evolution of the total strain energy density, as a widely accepted damage parameter for Mg alloys, was plotted over normalized life for different cases in Figure 4-19. This graph depicts a sharp decay in the damage over the beginning cycles, irrespective of the loading amplitude and material direction. Next, the mean value of the damage (MVD) was calculated by

$$MVD = \frac{\sum_{i=1}^n \Delta E_i}{n} \quad \text{Eq. 4-3}$$

along both ED and RD for two different stress amplitudes. Table 4-1 presents the quantified values and compares them with the corresponding damage at half-life and one-third of life cycles. On average 9.2% and 3.9% differences compared to mean value are observed at half-life and one-third of life cycles, respectively. The results suggest that one-third of life is more appropriate than the half-life for damage calculation in stress-controlled tests. This point is to be further investigated and verified.

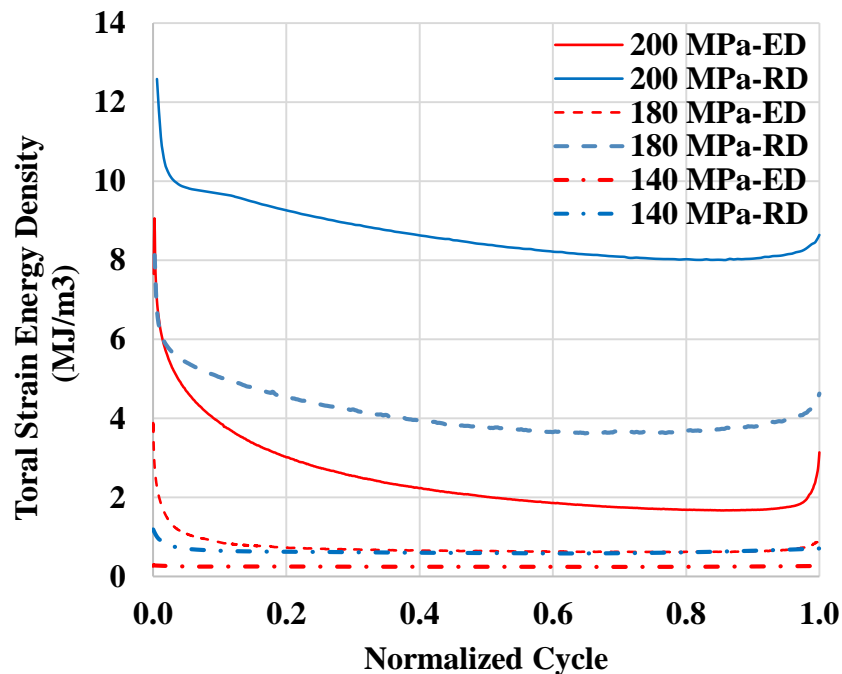


Figure 4-19. Evolution of TSED with respect to normalized life

Table 4-1. Strain energy density comparison in different cycles

Loading Scenario	Total strain energy density (MJ/M ³)		
	Mean value	Half-life	1/3 life
ED-200 MPa	2.46	2.02	2.43
ED-180 MPa	0.72	0.65	0.68
ED-140 MPa	0.26	0.24	0.25
RD-200 MPa	8.60	8.39	8.81
RD-180 MPa	4.14	3.78	4.11
RD-140 MPa	0.65	0.59	0.61

4.5.2 ESED Modification Accounting for Mean Stress Effect

From the early works of Ellyin and his co-workers [1,2], energy-based fatigue models have been used to predict the fatigue life of a variety of materials [3,4]. These models are based upon the fact that fatigue is the process of strain energy dissipation in the microstructure, through plastic strain accommodation. This dissipated strain energy can be quantified by measuring the area inside a stabilized cyclic hysteresis loop. Nonetheless, in the HCF regime close to fatigue endurance where in material behaves elastically, plastic strain energy's contribution to total fatigue damage is minimal; thus, energy resulting from the reversible portion of deformation, i.e., tensile (positive) elastic strain energy density, should be taken into account. On the other hand, the inclusion of tensile elastic energy density in the total strain energy density is justified as a means of considering the mean stress effects on fatigue life. Therefore, a proper definition for the positive ESED is crucial to reliably assess the fatigue life of components under cyclic loading.

In recent years, the strain energy density approach has been employed by many researchers to model the fatigue of Mg alloys, among other materials [108,109]. In all these investigations, it has been shown that the TSED consisting of plastic and tensile (positive) elastic parts yields good correlation between predicted and experimental lives. While the plastic strain energy density term was unanimously defined as the area inside a stabilized hysteresis loop, various definitions of positive the ESED were applied by different researchers. This variation indicates a challenge in defining the ESED term in such a way that it can be applied, with reasonable accuracy, to Mg alloys under cyclic loading at various stress/strain ratios.

As mentioned in section 2.1.2.2, JV model employs the Ellyin's formulation for ESED:

$$\Delta E_e^+ = \frac{\sigma_{max}^2}{2E} \quad \text{Eq. 4-4}$$

In order to evaluate the accuracy of this definition against the mean stress effects on ZK60 extrusion, ED samples were subjected to different load ratios, ranging from $R_\sigma = -0.5$ to $R_\sigma = 0.5$. Following the same approach described in section 4.4.2, the fully reversed strain-controlled tests along ED were employed to tune the model, and then the calculated JV parameters were used to correlate the life in all conditions. Figure 4-20 depicts experimentally obtained lives against JV predictions, in which ε and σ subscripts indicates strain- and stress-controlled tests, respectively. In each plot, solid, dash and dash-dot diagonal lines represent perfect match, 2x and 3x error bounds, respectively, between predicted and experimental lives. The ESED current definition excessively underpredicts samples' life under tensile mean stress. The largest discrepancy is seen for predictions at $R_\sigma = 0.5$, where lack of a good correlation with experimental results is evident. The observed inaccuracy is ascribed to the damage over-prediction by the ESED current definition.

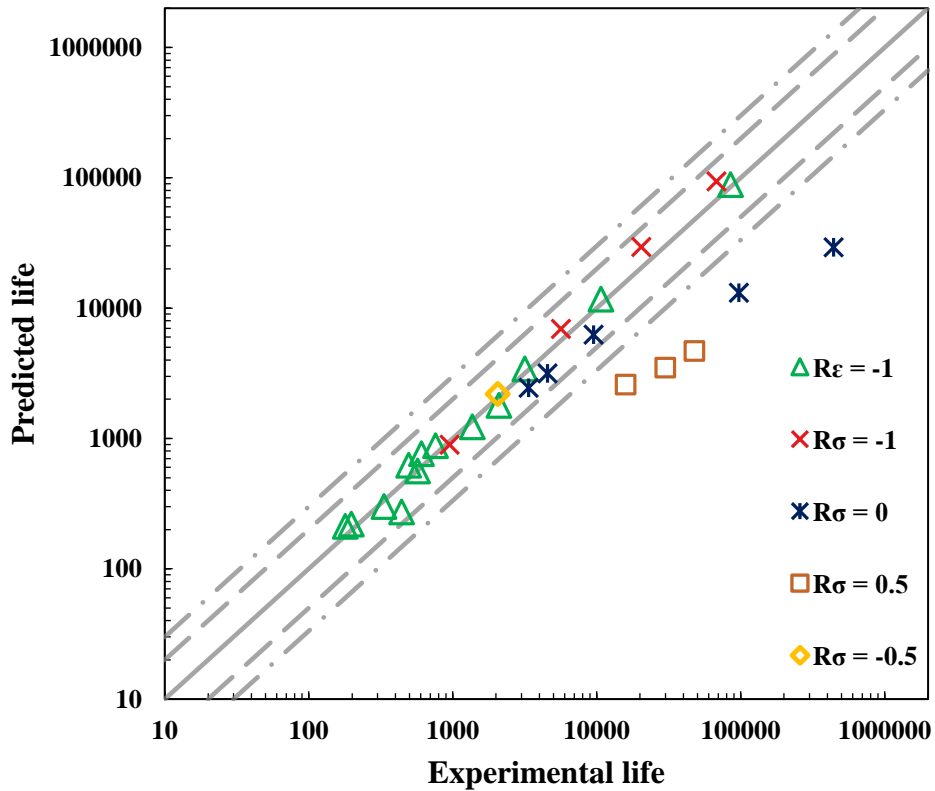


Figure 4-20. Experimental life vs. the life predicted by JV, using Ellyin's definition for ESED

In order to adjust the elastic-induced-damage, it is proposed to reformulate the positive strain energy density as,

$$\Delta E_e^+ = \frac{(\sigma_{max} + \sigma_{mean})\sigma_a}{2E} \quad \text{Eq. 4-5}$$

where σ_a is the stress amplitude, and σ_{mean} is the mean stress. The graphical interpretation of the proposed formulation, Eq. 4-5, is illustrated in Figure 4-21, for an experimental stabilized hysteresis loop tested at $R_\sigma > 0$. The area corresponding to the Ellyin's definition is also shown for comparison. As is observed, more fatigue damage is predicted by Eq. 4-4, which was found to be overestimation.

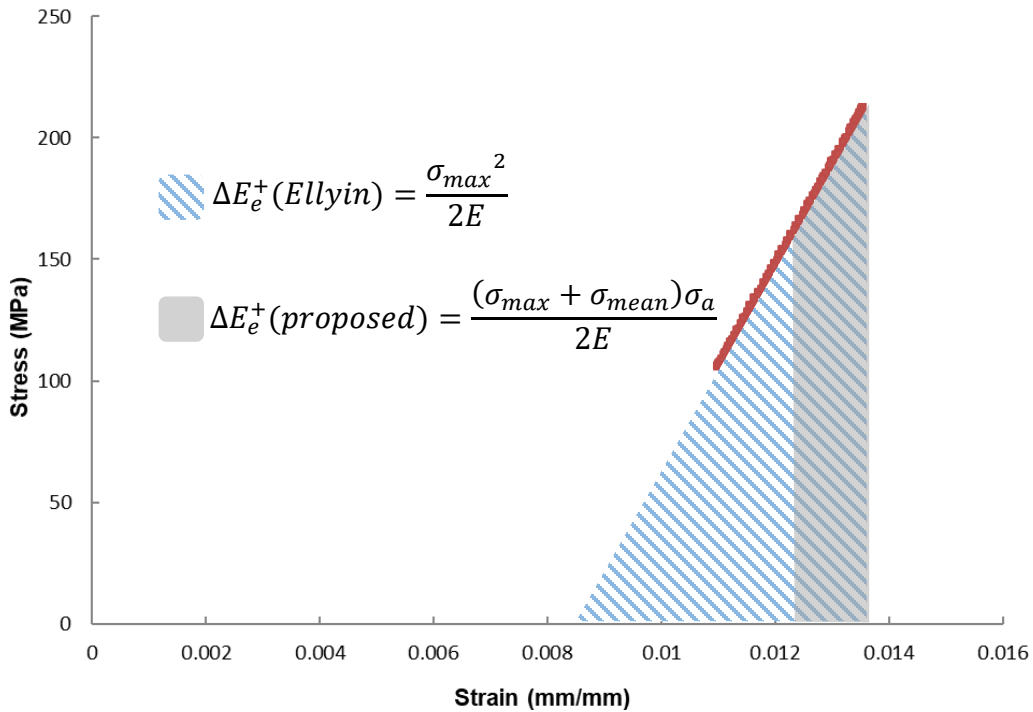


Figure 4-21. Schematic illustration of Ellyin's and proposed definition for positive elastic energy density

The fatigue lives were predicted by employing the new ESED definition, and the result are illustrated in Figure 4-22. The majority of predictions are within the 3x error bounds, with most of them in the 2x error bounds. According to the results, the proposed definition (Eq. 4-5) yields better predictions over the entire range of stress/strain ratios.

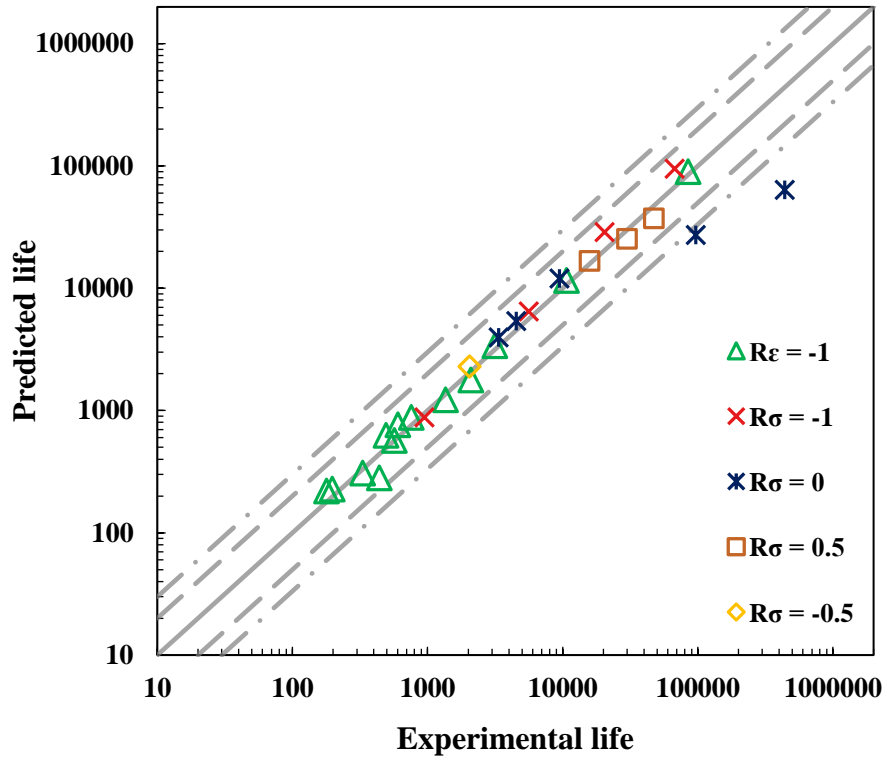


Figure 4-22. The experimental life vs. the life predicted by JV using the ESED new definition

4.6 Summary

The anisotropic fatigue behavior of ZK60 extrusion Mg alloy is investigated through fully reversed stress-control tests over a wide range of stress amplitudes along two different material directions: extrusion (ED) and radial (RD) directions. The in-plane random texture along RD promotes activation of twinning/detwinning deformations in both tension and compression reversals, which brings about a sigmoidal but near-symmetric shape for hysteresis loops along this direction. The stress-strain response along ED is asymmetric in tension and compression reversals if subjected to stress amplitudes of $\sigma_a > 140$ MPa. The asymmetry is attributed to different deformation mechanisms being active in the tension and compression reversals. Overall, loading along ED yields superior fatigue performance compared to RD. Fatigue strengths of 115 MPa and 87 MPa are obtained at 10^6 cycles based on the staircase statistical method for ED and RD, respectively. The effects of loading sequence and ratcheting strain on the fatigue response of the material are investigated. Lastly, one set of Jahed-Varvani (JV) coefficients extracted from strain-controlled tests is employed to model the anisotropic stress-control fatigue response of the material. The results show the promising capability of the JV model to describe the anisotropic

fatigue behavior of wrought Mg alloys. However, a better life-correlation is achieved by employing proposed ESED formulation when $R \geq 0$.

Chapter 5

Notch Effects

Notches are inevitable in many components and structures due to design limitations. In addition, they are the locations for stress concentration and are susceptible to fatigue failure. As a result, the fatigue response at a notch is of key importance. This chapter investigates notch effects on the fatigue behavior of ZK60 extrusion.

5.1 Material and Specimens

For the design of notched specimens in this study, the following restrictions were considered:

1. **Raw material availability:** The specimens must be machined from a cylindrical billet with

127 mm diameter.

2. **Grip size:** A minimum grip section is required to ensure no slippage at the grips.
3. **Loading:** As the specimen undergoes compression as well as tension in cyclic loading, both the buckling and yield loads of the designed specimen should be checked.
4. **Strain measurement techniques:** The digital image correlation (DIC) field of view should be considered a limitation in the specimen design.
5. **Stress concentration:** According to the literature, notch sensitivity will rise by increasing K_t in ZK60 [89], and the gap between K_t and K_f is more pronounced for K_t values greater than 2 for Mg alloys [82]. As a result, the minimum desired K_t was set as 2.5.

Accounting for these limitations, a center hole notch was selected as the sample's geometry, imposing a 2.5 theoretical stress concentration factor (Figure 5-1).

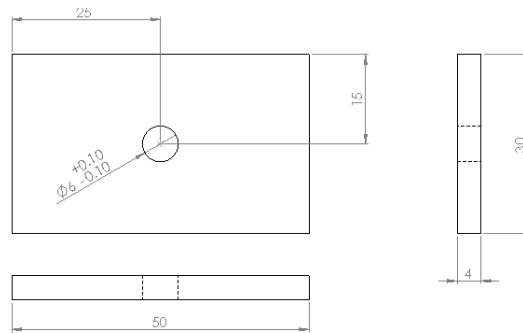


Figure 5-1. Cyclic notched samples (All dimensions are in mm)

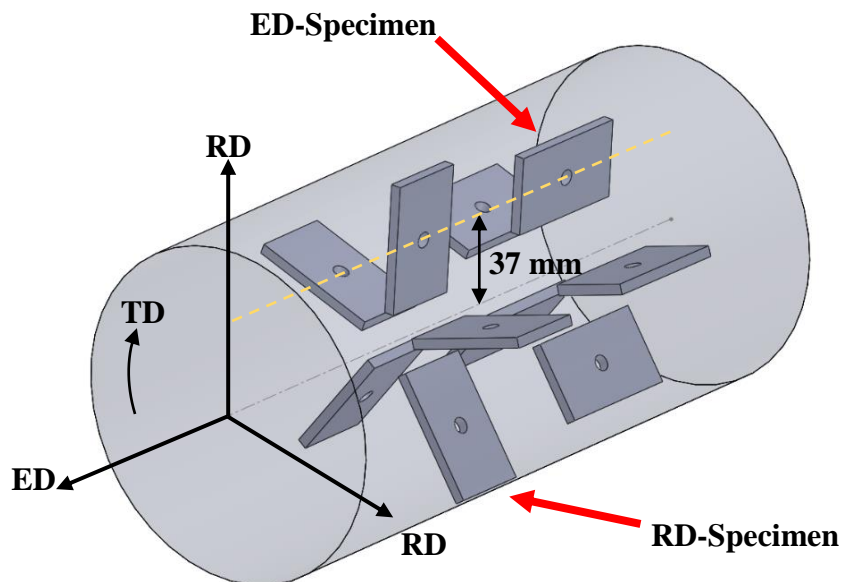


Figure 5-2. Schematic illustration of the reference cylindrical coordinate system utilized for the notched-specimen extraction

Based on the cylindrical coordination system, schematically depicted in Figure 5-2, the samples were CNC machined from the billet. ED and RD denote two perpendicular directions, the extrusion and radial directions, respectively.

5.2 Experimental Procedures

The specimen was loaded using the MTS 810 servo-hydraulic test-rig with 50 kN load capacity. All tests were run at ambient temperature under fully reversed stress-controlled condition with the nominal stress amplitude (σ_n) taken as the controlling parameter, determined by Eq.1 and ranging from 100 to 220 MPa. The test frequency was chosen to be between 0.1 and 10 Hz as a function of the stress amplitude, to ensure minimal difference between the command and the feedback of the imposed sinusoidal loading. Full separation of samples was considered as failure. At least two samples were tested at each stress amplitude to guarantee the results' reproducibility. The fatigue strength was calculated in accordance with the staircase statistical procedure at 10^6 cycles, as elaborated in the ISO-12107 standard [28]. The initiation and propagation of fatigue cracks were captured using a DIC system. The DIC system utilized in this research was the ARAMIS 3D with 5-megapixel resolution and a frame rate of 15 fps. The cameras were set up such that the sample wall thickness at the notch root, where crack initiation is expected, was captured in the right and left images (Figure 5-3). The cycle in which a crack was first detected at the notch root was recorded as the fatigue crack initiation pint. Subsequent to failure, the fracture surfaces were examined by means of a scanning electron microscope (SEM).

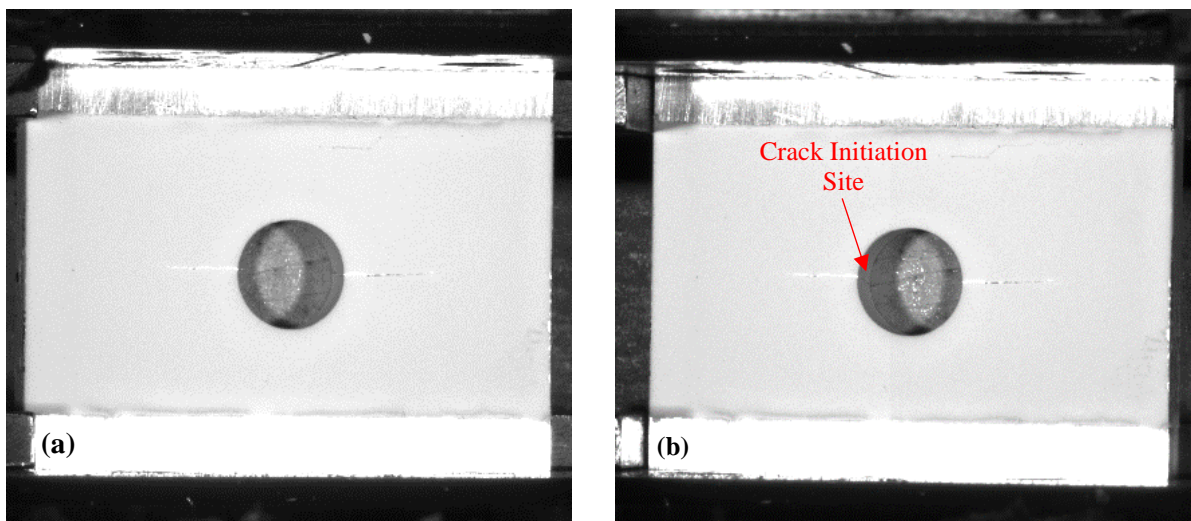


Figure 5-3. Detection of crack initiation and propagation on both sides of a notched sample by using a stereo camera setup: (a) left image, and (b) right image

5.3 Results

In the present study, fully reversed stress-control tests on center-hole notched samples were performed along radial (RD) and extrusion (ED) directions in order to investigate the effect of the loading direction on the notch sensitivity of the ZK60 extrusion. In addition to studying the local concentrated stress as a function of the cycles to failure, the crack initiation cycle was identified via visually tracking the lifetime of the samples, then plotted as the stress-life curves for both directions. The fatigue stress concentration factor and notch sensitivity were assessed over the life cycles.

5.3.1 Stress-life Behavior

Figure 5-4 illustrates the stress-life curves of notched specimens along ED and RD; the run-out tests are denoted by arrows. The observed anisotropic fatigue behavior of ED samples, showing superior fatigue performance, resembles the stress-life curve of un-notched specimens (Figure 4-10). These results can be explained by the key role of the plastic-induced-damage in the stress-controlled tests discussed in Chapter 4. Changing the failure criterion from final rupture to crack initiation results in similar anisotropic fatigue behavior, i.e., crack nucleation happens earlier in RD compared to ED under the same stress amplitudes (Figure 5-5).

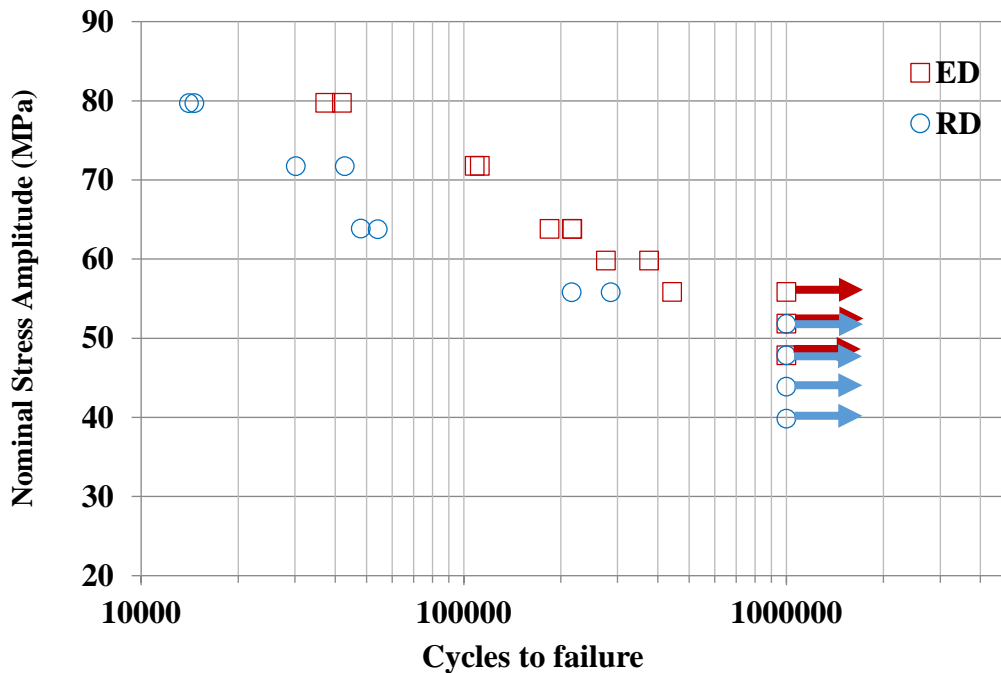


Figure 5-4. S-N curve for notched samples along ED and RD under fully reversed loading condition

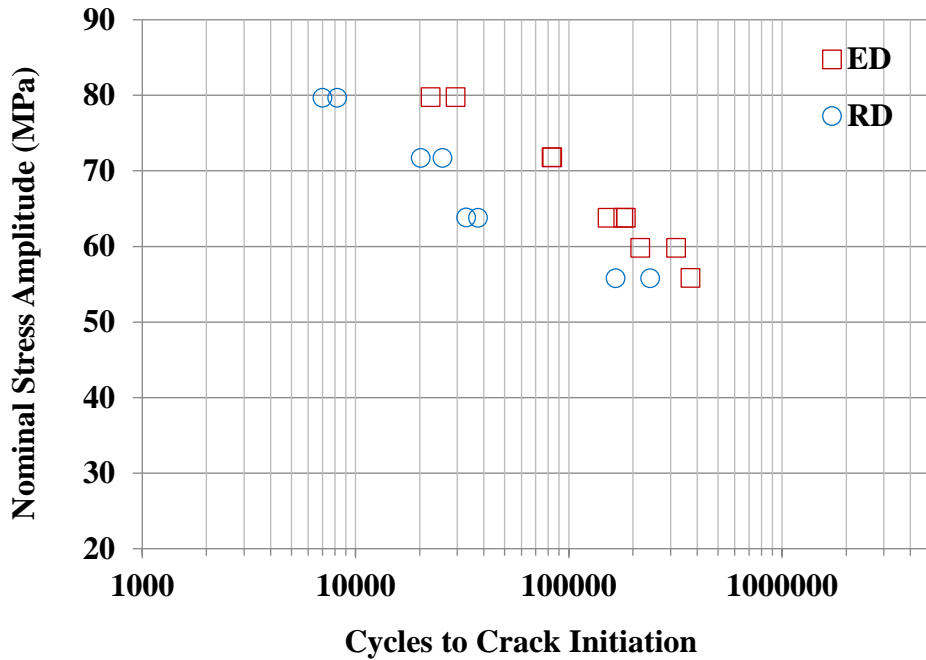


Figure 5-5. Stress vs. crack initiation life for notched samples along ED and RD

5.3.2 Notch Sensitivity

In order to evaluate the notch sensitivity, the fatigue strength for notched samples should be quantified first. To find the fatigue strength, the notched samples were tested sequentially by following the staircase method [28]. The results are tabulated in Table 5-1 and Table 5-2 for ED and RD, respectively. X denotes failed samples, whereas O indicates the surviving ones, and starred tests were not included in the calculation process. Table 5-3 lists the fatigue strengths of the material accompanied by the parameters of the staircase procedure calculated in both orientations. At 10^6 cycles, the fatigue strengths are 53 MPa and 46 MPa for the ED and RD samples, respectively.

Table 5-1. Sequential tests to obtain fatigue strength along ED

σ_r (MPa)	σ_n (MPa)	Sequence number of specimens								
		1	2	3	4	5	6	7	8	9
150	60			X		X				
140	56		O		O		X		X	
130	52		O						O	O
120	48	*O								

Table 5-2. Sequential tests to obtain fatigue strength along RD

σ_{root} (MPa)	σ_n (MPa)		Sequence Number of specimens								
			1	2	3	4	5	6	7	8	9
130	52						X				X
120	48			X		O		O		O	
110	44		O		O				O		
100	40	*O									

Table 5-3. Fatigue strength along two directions based on the staircase method

	ED	RD
Fatigue Strength (MPa)	53	46
No. of Tested Samples	9	9
Stress Step (MPa)	4	4
Standard Deviation	5.5	5.5

By substituting the fatigue strength of notched and un-notched samples into Eq. 2-10, one can calculate the K_f . Subsequently, the notch sensitivity (q) at 10^6 cycles can be found by employing Eq. 2-11. In comparison with ED, the sensitivity to the notch presence along RD is significantly lower, by 24 %. However, in both orientations, the detrimental effect of the notch is obvious.

Table 5-4. Notch parameters for ED and RD

	ED	RD
Fatigue stress concentration factor (K_f)	2.25	1.90
Notch sensitivity (q)	83 %	59 %

5.4 Discussion

The significant difference between the notch sensitivity of the material along ED and RD necessitates further investigations into the variation of this parameter as a function of life. Figure 5-6 shows the power functions fitted to S-N curves of the smooth and notched samples. By substituting the smooth and notch stresses in the K_f definition with their regression functions, K_f can be redefined as a function:

$$K_f = \frac{A(N_f)^B}{A'(N_f)^{B'}}$$

Eq. 5-1

where A and B are the smooth samples' constants, and A' and B' are dedicated to the notched samples. All the expressed parameters are calculated by linear regression. The Figure 5-7 and Figure 5-8 plot the variation of K_f and q with the number of cycles, respectively. The deviation between ED and RD for both graphs starts in LCF and escalates with increasing life.

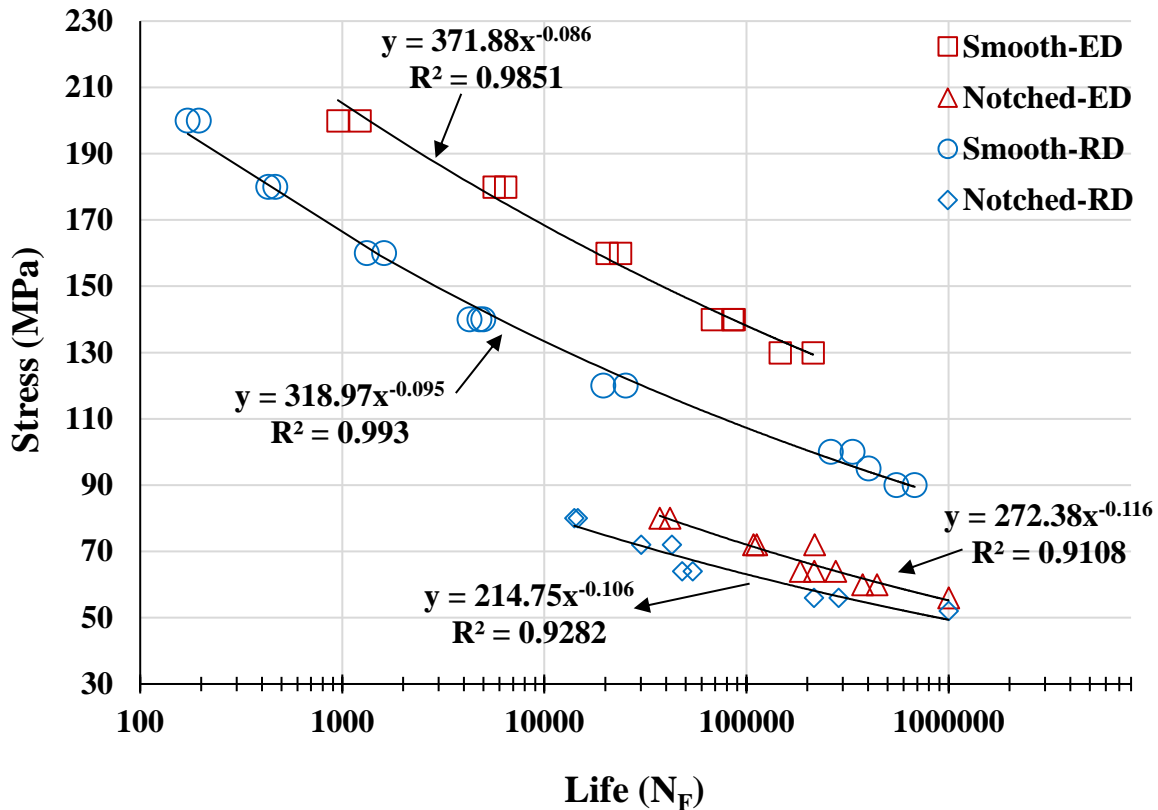


Figure 5-6. S-N curves for ED and RD notched and smooth samples with fitted power functions in semi-log scale

In LCF, notch sensitivity is diminished significantly for both material's directions, which can be attributed to two main factors:

1. Within the LCF, stress is quite high, which makes k_t impractical for stress/strain assessment [30]. Figure 2-3 shows that elevating the stress at the notch beyond the yield of the material decreases stress concentration factor. Therefore, the difference between the nominal and root stress will lessen, leading to considerably lower notch sensitivity in this region.

2. According to the literature, BTGs may be formed due to twining-detwinning activation in LCF [37,80,110]. BTGs induce beneficial residual compressive strain/stress in the unloading reversals, along with more-scattered energy dissipation via remapping the strain field adjacent to the notch. As a result, they increase life and decrease notch sensitivity [88]. This phenomenon is likely to be more pronounced for ED due to its intensive basal texture and higher chance of twining-detwinning activation.

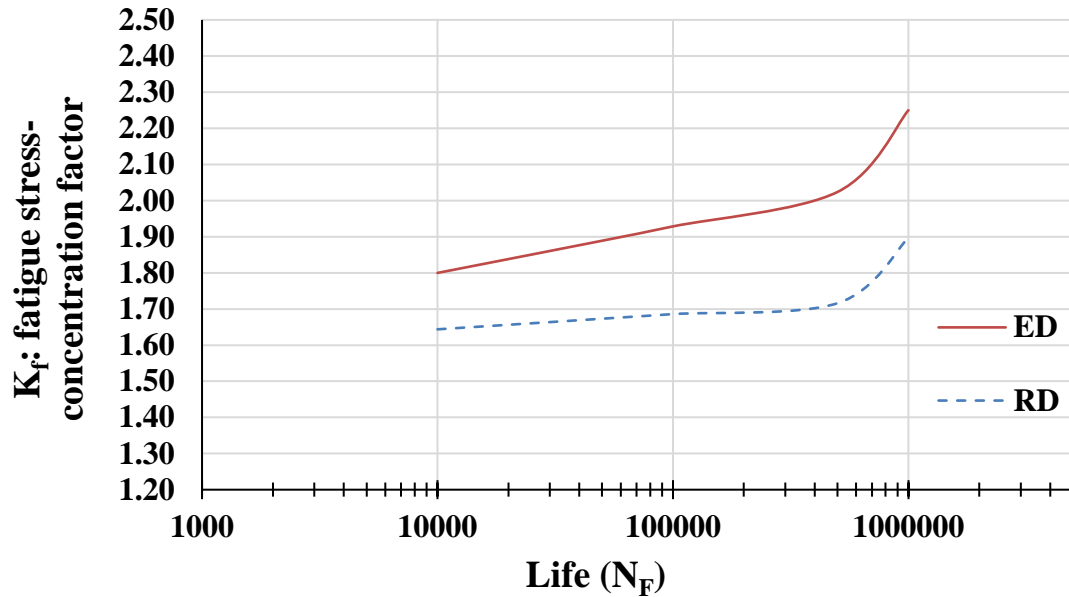


Figure 5-7. Evolution of fatigue stress concentration (K_f) over number of cycles

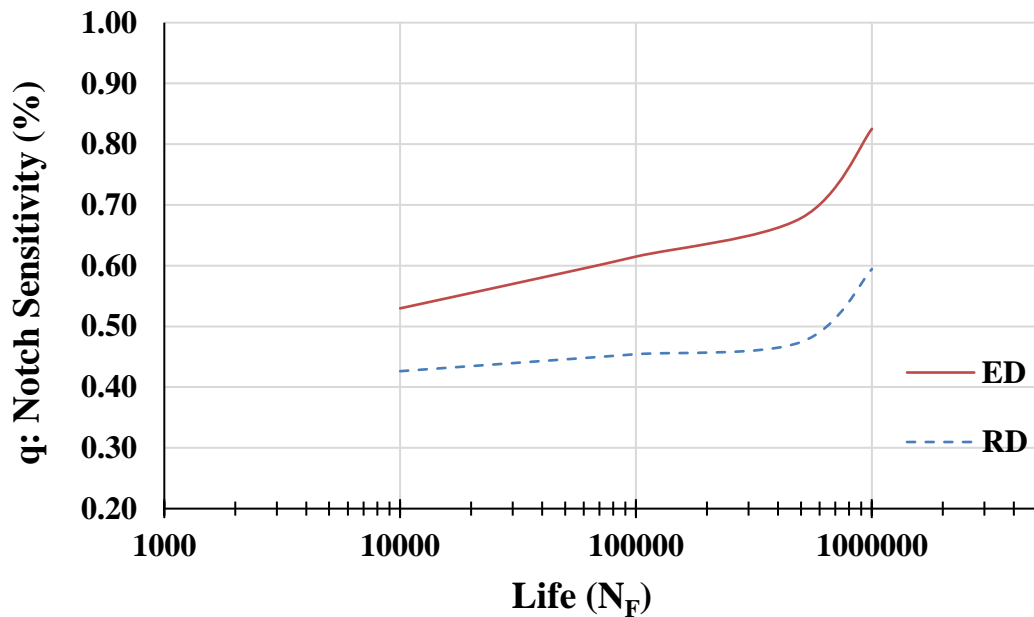


Figure 5-8. Evolution of notch sensitivity (q) over number of cycles

The notch sensitivity identified at 10^6 cycles for ED ($q=83\%$) is in line with that in previous investigations on wrought Mg alloys which reported q in the range of 80% to 100 % along the forming direction [85,88,89]. However, RD exhibits noteworthy lower notch sensitivity even in HCF. There is some potential hypothesis for the observed direction-dependency of the notch sensitivity in ZK60 extrusion:

1. The anisotropic nature of wrought alloys' mechanical properties, extensively explored in previous chapters, can affect notch sensitivity in two distinct ways. First, the stress/strain response in the vicinity of the notch can be redistributed in such a way that the maximum stress/strain location rotates from the root to other regions on the notch. Second, the new maximum stress/strain spot does not necessarily possess the same strength as the root. Conclusively, the strength, in conjunction with the maximum stress/strain location, both highly sensitive to a material's direction, should be considered simultaneously in the notch analysis of the anisotropic materials. Figure 5-9 exemplifies the case in which crack is not initiated at the root of the notch.
2. It is generally found that increasing the strength of the alloy boosts notch sensitivity [111]. Such behavior is attributed to “crackless plasticity”, in which stronger alloys have a greater capacity for small plastic flow, imposing concentrated work-hardening at the notch and consequently makes them more notch sensitive [112].

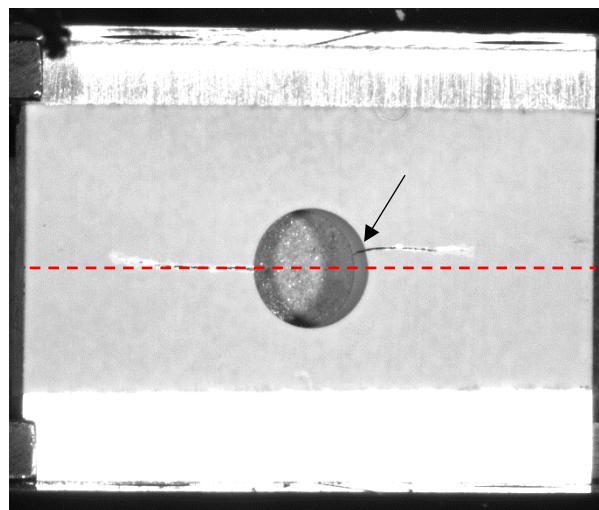


Figure 5-9. Crack initiated at a location other than the notch root (ED sample under $\sigma_{\text{root}} = 160$ MPa)

5.5 Summary

The effect of a material's orientation on the fatigue response of notched ZK60 extrusion was investigated via fully reversed stress-controlled experiments in the extrusion (ED) and radial directions (RD). The anisotropy observed in the stress-life curves of the notched ED and RD samples resembles the stress-controlled fatigue performance of the smooth samples. This observation is attributed to the higher strength of ED specimens, which imposes less plastic-induced-damage in the stress-controlled fatigue experiments. The ED specimens exhibit not only superior fatigue performance but also higher notch sensitivity ($q=83\%$) whereas loading along RD significantly reduces the notch sensitivity to 59%.

Chapter 6

Conclusions and Future Works

This chapter summarizes the conclusions and main findings of the thesis and presents possible directions for future studies.

6.1 Conclusions

From the results and discussions presented in this research, the following conclusions can be drawn:

1. The extruded alloy exhibited a sharp basal texture in the microstructure such that the hexagonal crystals were randomly orientated with their c-axes being perpendicular to

the extrusion direction.

2. The quasi-static behavior of ZK60 extrusion depends on the material's direction in the light of the developed texture. Indeed, while the static behavior along ED was asymmetric in tension and compression, RD and 45° samples exhibited symmetric behaviors.
3. In spite of different quasi-static behaviors along the different directions, the strain-controlled cyclic behavior in the LCF regime was not sensitive to the direction. However, the behaviors in the HCF regime were distinct.
4. JV, as an energy-based model, provides acceptable fatigue life predictions for ZK60 extrusion with anisotropic behavior. The model, calibrated using strain-controlled test results, is capable to explain the anisotropic fatigue behavior under stress-control condition.
5. Sigmoidal hysteresis loops with preserved symmetry were observed along RD under high-stress amplitudes because the twinning/detwinning deformations are active in both tension and compression reversals for stress-controlled tests.
6. Due to the sharp basal texture, loading along ED yields asymmetric hysteresis response accompanied by considerable cyclic hardening when stress is high enough to activate twinning/detwinning deformations.
7. In contrast to strain-controlled conditions, the material along ED exhibits superior fatigue performance superior to RD in stress-controlled experiments, due to ED's higher strength and consequently smaller hysteresis loops.
8. The limited investigations within the scope of this study suggest that 1/3 of life is more appropriate for damage calculation in stress-controlled tests, compared to the half-life cycle.
9. The proposed definition of ESED performs better compared to Ellyin's in term of life correlation of the fatigue tests with positive mean stress.
10. The fatigue performance of the notched ED samples is superior to that of the RD over a wide range of stress levels. The difference can be ascribed to the higher strength of ED, as strength dominates the plastic damage accumulated in the stress-controlled fatigue history of the alloy. Similar to final rupture, crack initiation occurs later in ED compared to in RD notched samples.

11. The difference between the notched fatigue behavior of RD and ED samples, in terms of concentration factor (K_f) and notch sensitivity (q), rises with by increasing number of cycles.
12. The low notch sensitivity of the material in LCF is attributed to the root and nominal stresses convergence in that highly-stressed region.
13. The noteworthy lower notch sensitivity of RD against ED may be related to the lower strength of the material in ED compared to RD. However, this finding accentuates the need of further exploration to determine probable microstructure correlations.

6.2 Future Works

The following future works are suggested, based on the findings of this thesis:

1. This study showed the auspicious capability of energy-based fatigue models to correlate the anisotropic fatigue-life of Mg alloys. These models rely on the strain-stress hysteresis response of the material, which is yet captured via experiment. In the case of complex loading, e.g. variable amplitude loading, the material's response quantification can become highly intricate and time-consuming. As a result, a phenomenological model, developed to predict the stress-controlled hysteresis loops as a substitute for laborious experimental work, will accelerate the overall life-calculation process and contribute to the industrial application of Mg alloys.
2. The intense anisotropy observed in the fatigue behavior of the ZK60 notched specimen necessitates further investigation, including strain-field assessments to discover the roots of discrepancies. To that intent, DIC, as an advanced and well-established strain measurement technique, is suggested.
3. The merit of the proposed JV model modification should be further verified under other types of loading, for instance, variable-amplitude, step, and multiaxial loadings.
4. Notch effects, as energy-derived phenomena, could be taken into account through energy-based fatigue models. The new model could be tuned via notch sensitivity as a correction factor.

References

- [1] Friedrich H, Schumann S. Research for a “new age of magnesium” in the automotive industry. *J Mater Process Technol* 2001;117:276–81. doi:10.1016/S0924-0136(01)00780-4.
- [2] Avedesian MM, Baker H. *ASM specialty handbook: Magnesium and its alloys*. ASM International; 1999.
- [3] BLAWERT, C.; HORT, N.; KAINER KU. Automotive applications of magnesium and its alloys. *Int J Adv Manuf Technol* 2004;39:851–65. doi:10.1007/s00170-007-1279-2.
- [4] Kulekci MK. Magnesium and its alloys applications in automotive industry. *Int J Adv Manuf Technol* 2008;39:851–65. doi:10.1007/s00170-007-1279-2.
- [5] Staroselsky A, Anand L. A constitutive model for hcp materials deforming by slip and twinning: Application to magnesium alloy AZ31B. *Int J Plast* 2003;19:1843–64. doi:10.1016/S0749-6419(03)00039-1.
- [6] Wu L, Jain A, Brown DW, Stoica GM, Agnew SR, Clausen B, et al. Twinning-detwinning behavior during the strain-controlled low-cycle fatigue testing of a wrought magnesium alloy, ZK60A. *Acta Mater* 2008;56:688–95. doi:10.1016/j.actamat.2007.10.030.
- [7] Casey J, Jahedmotlagh H. The strength-differential effect in plasticity. *Int J Solids Struct* 1984;20:377–93. doi:10.1016/0020-7683(84)90047-7.
- [8] Avedesian MM, Baker H. *ASM specialty handbook: magnesium and magnesium alloys*. 1999.
- [9] Smith Kn, Topper TH, Watson P. A stress-strain function for the fatigue of metals (Stress-strain function for metal fatigue including mean stress effect). *J Mater* 1970;5:767–78.
- [10] Xiong Y, Jiang Y. Fatigue of ZK60 magnesium alloy under uniaxial loading. *Int J Fatigue* 2014;64:74–83. doi:10.1016/j.ijfatigue.2014.02.019.
- [11] Yu Q, Zhang J, Jiang Y, Li Q. An experimental study on cyclic deformation and fatigue of extruded ZK60 magnesium alloy. *Int J Fatigue* 2012;36:47–58. doi:10.1016/j.ijfatigue.2011.08.016.

- [12] Roostaei AA, Jahed H. Role of loading direction on cyclic behaviour characteristics of AM30 extrusion and its fatigue damage modelling. *Mater Sci Eng A* 2016;670:26–40. doi:10.1016/j.msea.2016.05.116.
- [13] Albinmoussa J, Jahed H. Multiaxial effects on LCF behaviour and fatigue failure of AZ31B magnesium extrusion. *Int J Fatigue* 2014;67:103–16. doi:10.1016/j.ijfatigue.2014.01.025.
- [14] Castro F, Jiang Y. Fatigue life and early cracking predictions of extruded AZ31B magnesium alloy using critical plane approaches. *Int J Fatigue* 2016;88:236–46. doi:10.1016/j.ijfatigue.2016.04.002.
- [15] Toscano D, Shaha SK, Behravesb B, Jahed H, Williams B. Effect of forging on the low cycle fatigue behavior of cast AZ31B alloy. *Mater Sci Eng A* 2017;706:342–56. doi:10.1016/j.msea.2017.08.086.
- [16] Park SH, Hong SG, Yoon J, Lee CS. Influence of loading direction on the anisotropic fatigue properties of rolled magnesium alloy. *Int J Fatigue* 2016;87:210–5. doi:10.1016/j.ijfatigue.2016.01.026.
- [17] Jahed H, Varvani-Farahani A. Upper and lower fatigue life limits model using energy-based fatigue properties. *Int J Fatigue* 2006;28:467–73. doi:10.1016/j.ijfatigue.2005.07.039.
- [18] Ellyin F, Golos K. Multiaxial Fatigue Damage Criterion. *J Eng Mater Technol* 1988;110:63. doi:10.1115/1.3226012.
- [19] Gryguc A, Shaha SK, Jahed H, Wells M, Williams B, McKinley J. Tensile and fatigue behaviour of as-forged AZ31B extrusion. *Frat Ed Integrita Strutt* 2016;10:251–8. doi:10.3221/IGF-ESIS.38.34.
- [20] Toscano D, Shaha SK, Behravesb B, Jahed H, Williams B, Su X. Influence of low temperature forging on microstructure and low cycle fatigue behavior of cast AZ31B Mg alloy. *Miner Met Mater Ser* 2018;Part F7:267–73. doi:10.1007/978-3-319-72332-7_41.
- [21] Karparvarfard SMH, Shaha SK, Behravesb SB, Jahed H, Williams BW. Fatigue characteristics and modeling of cast and cast-forged ZK60 magnesium alloy. *Int J Fatigue* 2018:1–15. doi:10.1016/j.ijfatigue.2018.03.019.
- [22] Gryguc A, Behravesb SB, Shaha SK, Jahed H, Wells M, Williams B, et al. Low-cycle

- fatigue characterization and texture induced ratcheting behaviour of forged AZ80 Mg alloys. *Int J Fatigue* 2018;116:429–38. doi:10.1016/j.ijfatigue.2018.06.028.
- [23] Roostaei AA, Jahed H. Multiaxial cyclic behaviour and fatigue modelling of AM30 Mg alloy extrusion. *Int J Fatigue* 2017;97:150–61. doi:10.1016/j.ijfatigue.2016.12.037.
- [24] Gryguc A, Shaha SK, Behravesh SB, Jahed H, Wells M, Williams B, et al. Monotonic and cyclic behaviour of cast and cast-forged AZ80 Mg. *Int J Fatigue* 2017;104:136–49. doi:10.1016/j.ijfatigue.2017.06.038.
- [25] Behravesh SB, Jahed H, Lambert S. Fatigue characterization and modeling of AZ31B magnesium alloy spot-welds. *Int J Fatigue* 2014;64:1–13. doi:10.1016/j.ijfatigue.2014.01.026.
- [26] Noban M, Jahed H, Winkler S, Ince A. Fatigue characterization and modeling of 30CrNiMo8HH under multiaxial loading. *Mater Sci Eng A* 2011;528:2484–94. doi:10.1016/j.msea.2010.11.075.
- [27] Behravesh SB, Jahed H, Lambert S. Characterization of magnesium spot welds under tensile and cyclic loadings. *Mater Des* 2011;32:4890–900. doi:10.1016/j.matdes.2011.06.001.
- [28] International Organization for Standardization. ISO 12107-Metallic materials — Fatigue testing — Statistical planning and analysis of data. 2003.
- [29] Dixon WJ, Mood AM. A Method for Obtaining and Analyzing Data. *J Am Stat Assoc* 1948;43:109–26.
- [30] Stephens RI, Fatemi A, STEPHENS RR, FUCHS H O. *Metal Fatigue in Engineering* (second Edition). vol. 103. 2001. doi:10.1115/1.3225026.
- [31] Jordon JB, Brown HR, El Kadiri H, Kistler HM, Lett RL, Baird JC, et al. Investigation of fatigue anisotropy in an extruded magnesium alloy. *Int J Fatigue* 2013;51:8–14. doi:10.1016/j.ijfatigue.2013.01.006.
- [32] Roostaei AA, Jahed H. A cyclic small-strain plasticity model for wrought Mg alloys under multiaxial loading: Numerical implementation and validation. *Int J Mech Sci* 2018;145:318–29. doi:10.1016/j.ijmecsci.2018.07.024.
- [33] Roostaei AA, Jahed H. Multiaxial cyclic behaviour and fatigue modelling of AM30 Mg

- alloy extrusion. *Int J Fatigue* 2017;97:150–61. doi:10.1016/j.ijfatigue.2016.12.037.
- [34] Jahadi R, Sedighi M, Jahed H. Effects of aluminum and copper cover tube casing on the ECAP process of AM30 magnesium alloy. *Mater Manuf Process* 2017;32:1375–83. doi:10.1080/10426914.2016.1269917.
- [35] Jahadi R, Sedighi M, Jahed H. ECAP effect on the micro-structure and mechanical properties of AM30 magnesium alloy. *Mater Sci Eng A* 2014;593:1375–83. doi:10.1016/j.msea.2013.11.042.
- [36] Albinmousa J, Pascu A, Jahed H, Horstemeyer MF, Luo A, Chen D, et al. Monotonic and Fatigue Behavior of Magnesium Extrusion Alloy AM30: An International Benchmark Test in the “Magnesium Front End Research and Development Project” 2010. doi:10.4271/2010-01-0407.
- [37] Dallmeier J, Huber O, Saage H, Eigenfeld K. Uniaxial cyclic deformation and fatigue behavior of AM50 magnesium alloy sheet metals under symmetric and asymmetric loadings. *Mater Des* 2015;70:10–30. doi:10.1016/j.matdes.2014.12.056.
- [38] Kim S-H, Hong S-G, Lee J-H, Soo Lee C, Yoon J, Yu H, et al. Anisotropic in-plane fatigue behavior of rolled magnesium alloy with {10–12} twins. *Mater Sci Eng A* 2017;700:191–7. doi:10.1016/j.msea.2017.06.004.
- [39] Lv F, Yang F, Duan QQ, Luo TJ, Yang YS, Li SX, et al. Tensile and low-cycle fatigue properties of Mg-2.8% Al-1.1% Zn-0.4% Mn alloy along the transverse and rolling directions. *Scr Mater* 2009;61:887–90. doi:10.1016/j.scriptamat.2009.07.023.
- [40] Ishihara S, Taneguchi S, Shibata H, Goshima T, Saiki a. Anisotropy of the fatigue behavior of extruded and rolled magnesium alloys. *Int J Fatigue* 2013;50:94–100. doi:10.1016/j.ijfatigue.2012.02.011.
- [41] Park SH, Hong SG, Bang W, Lee CS. Effect of anisotropy on the low-cycle fatigue behavior of rolled AZ31 magnesium alloy. *Mater Sci Eng A* 2010;527:417–23. doi:10.1016/j.msea.2009.08.044.
- [42] Albinmousa J, Jahed H, Lambert S. Cyclic behaviour of wrought magnesium alloy under multiaxial load. *Int J Fatigue* 2011;33:1127–39. doi:10.1016/j.ijfatigue.2011.01.009.

- [43] Marzbanrad B, Toyserkani E, Jahed H. Cyclic hysteresis of AZ31B extrusion under load-control tests using embedded sensor technology. *Fatigue Fract Eng Mater Struct* 2017;40:221–32. doi:10.1111/ffe.12488.
- [44] Noban M, Albinmousa J, Jahed H, Lambert S. A continuum-based cyclic plasticity model for AZ31B magnesium alloy under proportional loading. *Procedia Eng* 2011;10:1366–71. doi:10.1016/j.proeng.2011.04.227.
- [45] Kalatehmollaei E, Mahmoudi-Asl H, Jahed H. An asymmetric elastic-plastic analysis of the load-controlled rotating bending test and its application in the fatigue life estimation of wrought magnesium AZ31B. *Int J Fatigue* 2014;64:33–41. doi:10.1016/j.ijfatigue.2014.02.012.
- [46] Behravesh SB. *Fatigue Characterization and Cyclic Plasticity Modeling of Magnesium Spot-Welds* 2013:264.
- [47] Kleiner S, Uggowitzer PJ. Mechanical anisotropy of extruded Mg-6% Al-1% Zn alloy. *Mater Sci Eng A* 2004;379:258–63. doi:10.1016/j.msea.2004.02.020.
- [48] Xiong Y, Jiang Y. Cyclic deformation and fatigue of rolled AZ80 magnesium alloy along different material orientations. *Mater Sci Eng A* 2016;677:58–67. doi:10.1016/j.msea.2016.09.031.
- [49] Gryguc A, Shaha SK, Behravesh SB, Jahed H, Wells M, Williams B. Compression Behaviour of Semi-closed Die Forged AZ80 Extrusion. *Miner Met Mater Ser* 2017;Part F7:361–9. doi:10.1007/978-3-319-51382-9_39.
- [50] Lin YC, Chen XM, Liu ZH, Chen J. Investigation of uniaxial low-cycle fatigue failure behavior of hot-rolled AZ91 magnesium alloy. *Int J Fatigue* 2013;48:122–32. doi:10.1016/j.ijfatigue.2012.10.010.
- [51] Wang C, Luo TJ, Zhou JX, Yang YS. Anisotropic cyclic deformation behavior of extruded ZA81M magnesium alloy. *Int J Fatigue* 2017;96:178–84. doi:10.1016/j.ijfatigue.2016.11.020.
- [52] Xiong Y, Gong X, Jiang Y. Effect of initial texture on fatigue properties of extruded ZK60 magnesium alloy. *Fatigue Fract Eng Mater Struct* 2018;274–276:193–8. doi:10.1111/ffe.12792.

- [53] Wu L. Mechanical Behavior and the Role of Deformation Twinning in Wrought Magnesium Alloys Investigated Using Neutron and Synchrotron X-ray Diffraction. 2009.
- [54] Pahlevanpour A, Karparvarfard S, Shaha SK, Behraves SB, Adibnazari S, Jahed H. Anisotropy in the Quasi-static and Cyclic Behavior of ZK60 Extrusion Alloy; Characterization and Fatigue Modeling. *Mater Des* 2018.
- [55] Hadadzadeh A, Wells MA, Shaha SK, Jahed H, Williams BW. Role of compression direction on recrystallization behavior and texture evolution during hot deformation of extruded ZK60 magnesium alloy. *J Alloys Compd* 2017;702:274–89. doi:10.1016/j.jallcom.2017.01.236.
- [56] Park SH. Effect of initial twins on the stress-controlled fatigue behavior of rolled magnesium alloy. *Mater Sci Eng A* 2017;680:214–20. doi:10.1016/j.msea.2016.10.093.
- [57] Gao H, Ye W, Zhang Z, Gao L. Ratcheting behavior of ZEK100 magnesium alloy with various loading conditions and different immersing time. *J Mater Res* 2017;32:2143–52. doi:10.1557/jmr.2017.104.
- [58] Zhang H, Dong DX, Ma SJ, Gu CF, Chen S, Zhang XP. Effects of percent reduction and specimen orientation on the ratcheting behavior of hot-rolled AZ31B magnesium alloy. *Mater Sci Eng A* 2013;575:223–30. doi:10.1016/j.msea.2013.03.074.
- [59] Lv F, Yang F, Duan QQ, Yang YS, Wu SD, Li SX, et al. Fatigue properties of rolled magnesium alloy (AZ31) sheet: Influence of specimen orientation. *Int J Fatigue* 2011;33:672–82. doi:10.1016/j.ijfatigue.2010.10.013.
- [60] Sajuri Z Bin, Miyashita Y, Hosokai Y, Mutoh Y. Effects of Mn content and texture on fatigue properties of as-cast and extruded AZ61 magnesium alloys. *Int J Mech Sci* 2006;48:198–209. doi:10.1016/j.ijmecsci.2005.09.003.
- [61] Zhou HT, Zhang ZD, Liu CM, Wang QW. Effect of Nd and Y on the microstructure and mechanical properties of ZK60 alloy. *Mater Sci Eng A* 2007;445–446:1–6. doi:10.1016/j.msea.2006.04.028.
- [62] Xiong Y, Yu Q, Jiang Y. An experimental study of cyclic plastic deformation of extruded ZK60 magnesium alloy under uniaxial loading at room temperature. *Int J Plast* 2014;53:107–24. doi:10.1016/j.ijplas.2013.07.008.

- [63] Xiong Y, Yu Q, Jiang Y. Deformation of extruded ZK60 magnesium alloy under uniaxial loading in different material orientations. *Mater Sci Eng A* 2018;710:206–13. doi:10.1016/j.msea.2017.10.059.
- [64] Basquin OH. The exponential law of endurance tests. *Proc Am Soc Test Mater* 1910;10:625–30.
- [65] Manson SS. Behavior of materials under conditions of thermal stress. NACA Rep TN 2933 1954.
- [66] Garud YS. A New Approach to the Evaluation of Fatigue Under Multiaxial Loadings. *J Eng Mater Technol* 1981;103:118. doi:10.1115/1.3224982.
- [67] Lefebvre D, Neale KW, Ellyin F. A Criterion for Low-Cycle Fatigue Failure Under Biaxial States of Stress. *J Eng Mater Technol* 1981;103:1. doi:10.1115/1.3224968.
- [68] Ellyin F, Kujawski D. An energy-based fatigue failure criterion. *Microstruct Mech Behav Mater* 1985.
- [69] Paris P, Erdogan F. A Critical Analysis of Crack Propagation Laws. *J Basic Eng* 1963;85:528. doi:10.1115/1.3656900.
- [70] Shiozawa K, Kitajima J, Kaminashi T, Murai T, Takahashi T. Low-cycle fatigue deformation behavior and evaluation of fatigue life on extruded magnesium alloys. *Procedia Eng* 2011;10:1244–9. doi:10.1016/j.proeng.2011.04.207.
- [71] Dallmeier J, Huber O, Saage H, Eigenfeld K, Hilbig A. Quasi-static and fatigue behavior of extruded ME21 and twin roll cast AZ31 magnesium sheet metals. *Mater Sci Eng A* 2014;590:44–53. doi:10.1016/j.msea.2013.09.088.
- [72] Hyuk Park S, Hong SG, Ho Lee B, Bang W, Soo Lee C. Low-cycle fatigue characteristics of rolled Mg-3Al-1Zn alloy. *Int J Fatigue* 2010;32:1835–42. doi:10.1016/j.ijfatigue.2010.05.002.
- [73] Ishihara S, McEvily AJ, Sato M, Taniguchi K, Goshima T. The effect of load ratio on fatigue life and crack propagation behavior of an extruded magnesium alloy. *Int J Fatigue* 2009;31:1788–94. doi:10.1016/j.ijfatigue.2009.02.034.
- [74] Hasegawa S, Tsuchida Y, Yano H, Matsui M. Evaluation of low cycle fatigue life in AZ31

- magnesium alloy. *Int J Fatigue* 2007;29:1839–45. doi:10.1016/j.ijfatigue.2006.12.003.
- [75] Smith JO. The Effect of Range of Stress on the Fatigue Strength of Metals. Univ Illinois, Eng Exp Station Urbana, 1942;334:631–6.
- [76] Paul SK, Sivaprasad S, Dhar S, Tarafder S. Ratcheting and low cycle fatigue behavior of SA333 steel and their life prediction. *J Nucl Mater* 2010;401:17–24. doi:10.1016/j.jnucmat.2010.03.014.
- [77] Chen G, Lu LT, Cui Y, Xing RS, Gao H, Chen X. Ratcheting and low-cycle fatigue characterizations of extruded AZ31B Mg alloy with and without corrosive environment. *Int J Fatigue* 2015;80:364–71. doi:10.1016/j.ijfatigue.2015.06.022.
- [78] Jahed H, Varvani-Farahani A, Noban M, Khalaji I. An energy-based fatigue life assessment model for various metallic materials under proportional and non-proportional loading conditions. *Int J Fatigue* 2007;29:647–55. doi:10.1016/j.ijfatigue.2006.07.017.
- [79] Noban M, Jahed H, Ibrahim E, Ince A. Load path sensitivity and fatigue life estimation of 30CrNiMo8HH. *Int J Fatigue* 2012;37:123–33. doi:10.1016/j.ijfatigue.2011.10.009.
- [80] Luo TJ, Yang YS, Tong WH, Duan QQ, Dong XG. Fatigue deformation characteristic of as-extruded AM30 magnesium alloy. *Mater Des* 2010;31:1617–21. doi:10.1016/j.matdes.2009.08.042.
- [81] Begum S, Chen DL, Xu S, Luo AA. Strain-controlled low-cycle fatigue properties of a newly developed extruded magnesium alloy. *Metall Mater Trans A Phys Metall Mater Sci* 2008;39:3014–26. doi:10.1007/s11661-008-9677-0.
- [82] Found G. The Notch Sensitivity in Fatigue Loading of Some Magnesium-Base and Aluminium-Base Alloys. *Proc. Am. Soc. Test. Mater.*, 1946, p. 46: 715.
- [83] Sonsino CM, Dieterich K. Fatigue design with cast magnesium alloys under constant and variable amplitude loading. *Int J Fatigue* 2006;28:183–93. doi:10.1016/j.ijfatigue.2005.06.043.
- [84] Bhuiyan S, Mutoh Y, Miyashita Y, Ostuka Y. Notch Effect on Fatigue Strength of Die Cast AM60 Magnesium Alloy. *Asian Pacific Conf. Mater. Mech.*, 2009.
- [85] Zhang P, Lindemann J, Leyens C. Influence of shot peening on notched fatigue strength of

- the high-strength wrought magnesium alloy AZ80. *J Alloys Compd* 2010;497:380–5. doi:10.1016/j.jallcom.2010.03.079.
- [86] B. Kuester, M. Hilpert, A. Kiefer LW. Shot peening. WILEY-VCH; n.d.
- [87] M. Wollmann, J. Atoura, M. Mhaede LW. Comparing Fatigue Notch Sensitivities of Various Alloys Before and After Mechanical Surface Treating, n.d.
- [88] Denk J, Dallmeier J, Huber O, Saage H. The fatigue life of notched magnesium sheet metals with emphasis on the effect of bands of twinned grains. *Int J Fatigue* 2017;98:212–22. doi:10.1016/j.ijfatigue.2017.01.041.
- [89] Liu W-C, Dong J, Zhang P, Zheng X-W, Ding W-J, Li D-H, et al. Smooth and notched fatigue performance of aging treated and shot peened ZK60 magnesium alloy. *J Mater Res* 2010;25:1375–87. doi:10.1557/JMR.2010.0173.
- [90] ASTM, ASTM Int. Standard Test Methods for Tension Testing of Metallic Materials 1. *Astm* 2016:1–27. doi:10.1520/E0008.
- [91] Brown DW, Jain A, Agnew SR, Clausen B. Twinning and Detwinning during Cyclic Deformation of Mg Alloy AZ31B. *Mater Sci Forum* 2007;539–543:3407–13. doi:10.4028/www.scientific.net/MSF.539-543.3407.
- [92] Agnew SR, Christopher A. Calhoun and JJB. What is in a Strain Hardening “Plateau”? *Magnes. Technol.* 2016, Springer Int. Publ., 2016, p. 189–94.
- [93] Fleck N a., Muller GM, Ashby MF, Hutchinson JW. Strain gradient plasticity: Theory and experiment. *Acta Metall Mater* 1994;42:475–87. doi:10.1016/0956-7151(94)90502-9.
- [94] Máthis K, Beran P, Čapek J, Lukáš P, Lukáš P. In-situ neutron diffraction and acoustic emission investigation of twinning activity in magnesium. *J Phys Conf Ser* 2012;340:12096. doi:10.1088/1742-6596/340/1/012096.
- [95] Proust G, Tomé CN, Jain A, Agnew SR. Modeling the effect of twinning and detwinning during strain-path changes of magnesium alloy AZ31. *Int J Plast* 2009;25:861–80. doi:10.1016/j.ijplas.2008.05.005.
- [96] Yu Q, Zhang J, Jiang Y. Fatigue damage development in pure polycrystalline magnesium under cyclic tension-compression loading. *Mater Sci Eng A* 2011;528:7816–26.

- doi:10.1016/j.msea.2011.06.064.
- [97] Karparvarfard SMHH, Shaha SK, Behravesh SB, Jahed H, Williams BW. Microstructure, texture and mechanical behavior characterization of hot forged cast ZK60 magnesium alloy. *J Mater Sci Technol* 2017;33:907–18. doi:10.1016/j.jmst.2017.04.004.
- [98] Yu H, Xin Y, Chapuis A, Huang X, Xin R, Liu Q. The different effects of twin boundary and grain boundary on reducing tension-compression yield asymmetry of Mg alloys. *Nat Publ Gr* 2016;4–11. doi:10.1038/srep29283.
- [99] Wu YJ, Zhu R, Wang JT, Ji WQ. Role of twinning and slip in cyclic deformation of extruded Mg-3%Al-1%Zn alloys. *Scr Mater* 2010;63:1077–80. doi:10.1016/j.scriptamat.2010.08.008.
- [100] Yang F, Yin SM, Li SX, Zhang ZF. Crack initiation mechanism of extruded AZ31 magnesium alloy in the very high cycle fatigue regime. *Mater Sci Eng A* 2008;491:131–6. doi:10.1016/j.msea.2008.02.003.
- [101] Nan ZY, Ishihara S, McEvily AJ, Shibata H, Komano K. On the sharp bend of the S-N curve and the crack propagation behavior of extruded magnesium alloy. *Scr Mater* 2007;56:649–52. doi:10.1016/j.scriptamat.2007.01.009.
- [102] Zhu SP, Lei Q, Wang QY. Mean stress and ratcheting corrections in fatigue life prediction of metals. *Fatigue Fract Eng Mater Struct* 2017;40:1343–54. doi:10.1111/ffe.12569.
- [103] Zhu S-P, Lei Q, Huang H-Z, Yang Y-J, Peng W. Mean stress effect correction in strain energy-based fatigue life prediction of metals. *Int J Damage Mech* 2016;26:1219–41. doi:10.1177/1056789516651920.
- [104] Park SJ, Kim KS, Kim HS. Ratcheting behaviour and mean stress considerations in uniaxial low-cycle fatigue of Inconel 718 at 649 °C. *Fatigue Fract Eng Mater Struct* 2007;30:1076–83. doi:10.1111/j.1460-2695.2007.01177.x.
- [105] Begum S, Chen DL, Xu S, Luo AA. Effect of strain ratio and strain rate on low cycle fatigue behavior of AZ31 wrought magnesium alloy. *Mater Sci Eng A* 2009;517:334–43. doi:10.1016/j.msea.2009.04.051.
- [106] Noban M, Jahed H. Ratchetting strain prediction. *Int J Press Vessel Pip* 2007;84:223–33.

doi:10.1016/j.ijpvp.2006.10.003.

- [107] Wang F, Dong J, Jiang Y, Ding W. Cyclic deformation and fatigue of extruded ZK60 magnesium alloy with aging effects. vol. 615. Elsevier; 2014. doi:10.1016/j.msea.2012.10.048.
- [108] Roostaei AA, Jahed H. Multiaxial cyclic behaviour and fatigue modelling of AM30 Mg alloy extrusion. *Int J Fatigue* 2017;97:150–61. doi:10.1016/j.ijfatigue.2016.12.037.
- [109] Jahed H, Albinmoussa J. Multiaxial behaviour of wrought magnesium alloys – A review and suitability of energy-based fatigue life model. *Theor Appl Fract Mech* 2014;73:97–108. doi:10.1016/j.tafmec.2014.08.004.
- [110] Baird JC, Li B, Yazdan Parast S, Horstemeyer SJ, Hector LG, Wang PT, et al. Localized twin bands in sheet bending of a magnesium alloy. *Scr Mater* 2012;67:471–4. doi:10.1016/j.scriptamat.2012.06.007.
- [111] Yen CS, Dolan TJ. A critical review of the criteria for notch-sensitivity in fatigue of metals. *Univ Illinois Bull* 1952;49:62.
- [112] H. F. Moore. Crackless Plasticity - A New Property of Metals. *Iron Age* 1931:674.